



1-1-2019

Development Of Graphene And Polymer Based Nanomaterials For Analytical And Biological Applications

Xiao Liu

[How does access to this work benefit you? Let us know!](#)

Follow this and additional works at: <https://commons.und.edu/theses>

Recommended Citation

Liu, Xiao, "Development Of Graphene And Polymer Based Nanomaterials For Analytical And Biological Applications" (2019). *Theses and Dissertations*. 2859.
<https://commons.und.edu/theses/2859>

This Dissertation is brought to you for free and open access by the Theses, Dissertations, and Senior Projects at UND Scholarly Commons. It has been accepted for inclusion in Theses and Dissertations by an authorized administrator of UND Scholarly Commons. For more information, please contact und.common@library.und.edu.

DEVELOPMENT OF GRAPHENE AND PLOYMER BASED NANOMATERIALS
FOR ANALYTICAL AND BIOLOGICAL APPLICATIONS

by

Xiao Liu
Bachelor of Engineering, Jilin University, China 2014

A Dissertation

Submitted to the Graduate Faculty

of the

University of North Dakota

In partial fulfillment of the requirements

for the degree of

Doctor of Philosophy

Grand Forks, North Dakota
December
2019

Copyright 2019 Xiao Liu


This dissertation, submitted by Xiao Liu in partial fulfillment of the requirements for the Degree of Doctor of Philosophy from the University of North Dakota, has been read by the Faculty Advisory Committee under whom the work has been done, and is hereby approved.



Chairperson



This dissertation is being submitted by the appointed advisory committee as having met all of the requirements of the School of Graduate Studies at the University of North Dakota and is hereby approved.


Dr. Chris Nelson, Associate Dean
School of Graduate Studies

11/26/19
Date

PERMISSION

Title Development of Graphene and Polymer-based Nanomaterials for Analytical and Biological Applications

Department Chemistry

Degree Doctor of Philosophy

In presenting this document in partial fulfillment of the requirements for a graduate degree from the University of North Dakota, I agree that the library of this University shall make it freely available for inspection. I further agree that permission for extensive copying for scholarly purposes may be granted by the professor who supervised my dissertation work or, in her/his absence, by the Chairperson of the department or the Dean of the Graduate School. It is understood that any copying or publication or other use of this dissertation or part thereof for financial gain shall not be allowed without my written permission. It is also understood that due recognition shall be given to me and to the University of North Dakota in any scholarly use which may be made of any material in my dissertation.

Xiao Liu
December 2019

Abbreviations

ATCC	American Tissue Culture Collection
A549	Lung cancer cell line
CTAB	Hexadecyltrimethylammonium bromide
dsDNA	Double string DNA
DOX	Doxorubicin
DLS	Dynamic light scattering
DMSO	Dimethyl sulfoxide
DMEM	Dulbecco's modified eagle's medium
DAPI	4'-6-diamidino-2-phenylindole
EDTA	Ethylenediaminetetraacetic acid
Eu-SPN	Eu ³⁺ Coordinated Semiconducting Polymer Nanoparticles
Exo III	Exonuclease III
FTIR	Fourier-transform infrared spectroscopy
FAM	Fluorescein
FRET	Fluorescence resonance energy transfer
GO	Graphene Oxide
GQDs	Graphene quantum dots

HP	Hairpin Probe
HRTEM	High resolution transmission electron microscopy
L-15	Leibovitz's L-15 medium
mSilica	Mesoporous Silica
MEH-PPV	Poly[2-methoxy-5-(2-ethylhexyloxy)-1,4-phenylenevinylene]
MTT	3-(4,5-Dimethylthiazol-2-yl)-2,5-diphenyltetrazolium bromide
NIR	Near Infrared
PSMA	Poly(styrene-co-maleic anhydride)
PDT	Photodynamic therapy
PTT	Photothermal therapy
rGO	Reduced Graphene Oxide
ssDNA	Single String DNA
SW620	Colon cancer cell line
SPN	Semiconducting Polymer nanoparticles
spICP-MS	Single Particle inductively coupled plasma mass spectrometry

TEM	Transmission Electron Microscope
TEOS	Tetraethyl orthosilicate
U	Standard unit of enzyme activity
XPS	X-ray photoelectron spectroscopy

TABLE OF CONTENTS

LIST OF FIGURES	IX
LIST OF TABLES	XIV
LIST OF SCHEMES.....	XV
ACKNOWLEDGEMENTS.....	XVI
ABSTRACT.....	XVII
CHAPTER I.....	1
REDUCED GRAPHENE OXIDE/MESOPOROUS SILICA NANOPARTICLES FOR PH-TRIGGERED DRUG RELEASE AND PHOTOTHERMAL THERAPY	1
1. INTRODUCTION	1
2. EXPERIMENTAL SECTION	3
2.1. Chemicals.....	3
2.2. Instruments.....	4
2.3. Synthesis of Reduced Graphene Oxide / Mesoporous Silica Nanocarrier (rGO@msilica).....	5
2.4. Measurement of Pore Size and Surface Area	6
2.5. Measurement of Drug Loading and Release Efficiency.....	6
2.6. Photothermal Effect of rGO@msilica Nanocarrier.....	7
2.7. Biocompatibility of rGO@msilica Nanocarrier.....	7
2.8. Chemotherapeutic Effect of the DOX-loaded rGO@msilica Nanocarrier.....	7
2.9. Confocal Fluorescence Imaging of Drug Release in Cancer Cells.	8
2.10. Synergistic Therapeutic Efficiency.....	8
3. RESULTS AND DISCUSSION.....	8
3.1. Design and Synthesis of the DOX-Loaded rGO@msilica Nanocarrier.....	8
3.2. Characterization of the DOX-Loaded rGO@msilica Nanocarrier.	10
3.3. Drug loading.....	14
3.4. pH-Responsive Drug Release.	15
3.5. Biocompatibility of the rGO@msilica Nanocarrier.....	17
3.6. Chemotherapy Evaluation of the DOX-Loaded rGO@msilica Nanocarrier.	18
3.7. Cellular Uptake and Drug Release in Cells	19
3.8. Synergistic Chemo-Photothermal Therapy of Cancer Cells.....	20
4. CONCLUSIONS.....	22

CHAPTER II.....	23
GRAPHENE OXIDE-BASED FLUORESCENCE ASSAY FOR SENSITIVE DETECTION OF DNA EXONUCLEASE ENZYMATIc ACTIVITY	23
1. INTRODUCTION	23
2. EXPERIMENTAL SECTION	25
2.1. <i>Chemicals and Instruments</i>	25
2.2. Feasibility of the sensor for Exo III detection	25
2.3. <i>Detection of Exo III activity</i>	26
2.4. <i>Evaluation of the selectivity</i>	26
2.5. <i>Exonuclease inhibition assay</i>	26
2.6. <i>Performance in 25-times diluted serum</i>	26
2.7. <i>Kinetic Analysis</i>	27
3. RESULTS AND DISCUSSION.....	27
3.1. <i>Design of the Exo III assay</i>	27
3.2. <i>Characterization of GO</i>	28
3.3. <i>Feasibility investigation</i>	30
3.4. <i>Optimization of experimental conditions</i>	30
3.5. <i>Exo III detection</i>	32
3.6. <i>Selectivity investigation</i>	34
3.7. <i>Inhibition test</i>	35
3.8. <i>Application in diluted serum sample</i>	36
3.9. <i>Kinetic Analysis</i>	37
4. CONCLUSIONS.....	38
CHAPTER III	39
ONE POT SYNTHESIS OF GRAPHENE QUANTUM DOTS USING HUMIC ACID AND ITS APPLICATION FOR COPPER(II) ION DETECTION	39
1. INTRODUCTION	39
2. EXPERIMENTAL SECTION	41
2.1. <i>Chemical and materials</i>	41
2.2. <i>Synthesis of GQDs</i>	42
2.3. <i>Characterization of GQDs</i>	42
2.4. <i>pH Effect and photostability</i>	43
2.5. <i>Quantum yield detection</i>	44
2.6. <i>Cu²⁺ induced aggregation analysis</i>	44
2.7. <i>Cu²⁺ detection procedure</i>	44
2.8. <i>Selectivity investigation of GQDs</i>	44
3. RESULTS AND DISCUSSION.....	45
3.1. <i>Formation and design of the highly fluorescent GQDs</i>	45
3.2. <i>Characterization of graphene quantum dots</i>	46

3.3 <i>Fluorescent properties</i>	49
3.4 <i>pH effect, photostability and stability on metal ions</i>	50
3.5 <i>Experiment condition optimization</i>	52
3.6 <i>Cu²⁺ Detection</i>	54
3.7 <i>Analysis of spiked sample</i>	55
4. CONCLUSION.....	55
CHAPTER IV	56
TWO READOUTS SENSOR USING EU COORDINATED MEH PPV SPN FOR THE DETECTION OF COPPER(II) IONS	57
1. INTRODUCTION	57
2. EXPERIMENTAL SECTION.....	59
2.1 <i>Materials and instruments</i>	59
2.2 <i>Synthesis of the Eu-SPN</i>	61
2.3 <i>Characterization of the Eu-SPN</i>	61
2.4 <i>Cu²⁺ detection in fluorometric and spICP-MS methods</i>	61
2.5 <i>Selectivity investigation of Eu-SPN in Fluorometric and spICP-MS Methods</i>	61
3. RESULTS AND DISCUSSION.....	62
3.1 <i>Design of the Eu-SPN sensing platform</i>	62
3.2 <i>Synthesis and characterization of Eu-SPN</i>	63
3.3 <i>Feasibility investigation of Cu²⁺ detection using spICP-MS</i>	64
3.4 <i>Optimization of the reaction conditions</i>	66
3.5 <i>Sensitivity of SPN-Eu on Cu²⁺ by fluorescence</i>	71
3.6 <i>Selectivity of SPN-Eu on various metal ions by fluorescence</i>	72
3.7 <i>Cu²⁺ detection in spICP-MS</i>	73
3.8 <i>Selectivity of SPN-Eu on Cu²⁺ by spICP-MS</i>	76
3.9 <i>Analysis of the spiked samples</i>	77
4. CONCLUSIONS.....	78
REFERENCES	79

LIST OF FIGURES

Figure		Page
1.	TEM images of rGO@msilica nanocarrier. (A) A pure rGO sheet. (B) low magnification TEM image of rGO@msilica nanocarrier (300 - 500 nm). (C) HRTEM image of rGO@msilica nanocarrier.	11
2.	Elemental analysis of the of rGO@msilica nanocarriers. STEM image of the rGO@msilica nanocarrier (A) and its corresponding elemental maps of Si (B, green color), carbon (C, yellow color), and oxygen (D, red color) (scale bar = 250 nm).	12
3.	The Nitrogen adsorption-desorption isotherm curve (A) and the pore size distribution (B) of rGO@msilica nanocarriers based on BJH method. The outgas was conducted at 120 °C for 1.2 h. (C) Absorption spectra of GO, GO@msilica and rGO@msilica nanocarrier. (D) Zeta potential of GO, GO@msilica and rGO@msilica nanocarrier in pH 5.0, 10 mM PBS buffer at room temperature.	12
4.	DOX loading into rGO@msilica nanocarrier. (A) The fluorescence spectra of DOX (0.01 mg/mL) at different pH values. (B) Calibration curve of DOX in 10 mM pH 7.4 PBS buffer (DOX concentration: 3.0×10^{-2} , 2.0×10^{-2} , 1.0×10^{-2} , 5.0×10^{-3} , 2.5×10^{-3} , 1.3×10^{-3} mg/mL). (C) Fluorescence spectra of initial pure DOX solution to be used for loading (curve a) and the supernatant after centrifuging DOX-loaded rGO@msilica nanocarrier (curve b). Inset shows the initial pure DOX solution (a) and the DOX-loaded rGO@msilica nanocarrier solution after centrifugation (b). (D) The fluorescence spectra of (a) pure DOX (3.0×10^{-2} mg/mL), (b) 7.5×10^{-1} mg/mL DOX-loaded rGO@msilica nanocarriers (with equivalent DOX concentration of 2.7×10^{-2} g/mL) in 10 mM pH 7.4 PBS buffer (c) and pure 10 mM pH 7.4 PBS buffer solution as control. Excitation wavelength: 480 nm, Emission wavelength: 591 nm.	14
5.	(A) Cumulative release of DOX from DOX-loaded rGO@msilica (1.0 mg/mL) within different pH buffers with or without irradiation. An NIR laser (808 nm, 0.3 W/cm^2) was used for irradiation. (B) Temperature increasing curves of PBS, GO@msilica nanocarrier (0.5 mg/mL) and rGO@msilica nanocarrier (0.5 mg/mL) solutions exposed to an NIR laser (808 nm, 0.3 W/cm^2) for 15 min. The solution volume was 2.0 mL.	16
6.	Cell viability of A549 cells (A) and SW620 cells (B) after the treatments with various concentrations of rGO@msilica nanocarriers for 24 h.	18
7.	(A) The cell viability of the A549 cells with different concentrations of DOX-	

- loaded rGO@msilica nanocarrier. The concentration of DOX loaded rGO@msilica was from 2.5×10^{-5} mg/mL to 2.5 mg/mL. The incubation time was 12 hours. (B) The time effect of the DOX-loaded rGO@msilica nanocarrier on the cell viability of the A549 cells. The concentration of the DOX-loaded rGO@msilica nanocarrier was 2.5×10^{-2} mg/mL..... 19
8. (A) Confocal fluorescence images of A549 cells incubated with DOX-loaded rGO@msilica nanocarrier at different time periods, including 10 min, 6 h, and 24 h. The nucleus was counterstained with DAPI (blue). The red fluorescence was from DOX. (B) The fluorescence intensity of DOX in cells was quantified by Image J software. (**** p < 0.0001).....20
 9. The cell viabilities of SW620 (A) and A549 (B) cells after different treatments. “-” stands for no treatment. “+” stands for the treatment. The cells were incubated with nanocarriers for 6 h and 24 h, respectively, followed by the 808 nm laser irradiation of 15 min. (**** p < 0.0001).....21
 10. (A) The SEM image and corresponding elemental maps of GO in (B) carbon (pink), (C) oxygen (yellow). (D) overlaid mapping of GO (scale bar = 10 μ m). (E) UV-vis absorption spectrum of GO with a typical absorption maximum at 230 nm.....29
 11. Fluorescence spectra of HP (100 nM) under different conditions. (a) 100 nM HP, (b) 100 nM HP + 20 μ g/mL GO, (c) 100 nM HP + 0.5 U/mL Exo III + 20 μ g/mL GO. $\lambda_{ex} = 480$ nm, All the reagents were incubated in 1X NEBuffer 2. $\lambda_{em} = 500$ nm - 650 nm.....30
 12. (A) A time-based fluorescence intensity curve was collected in 100 μ L 1X NEBuffer2 solution containing 50 nM HP solution with addition of 20 μ g/mL GO at 37 $^{\circ}$ C for 1200 s. (B) Fluorescence intensity ratios of F/F0 at different concentrations of GO. F0 refers to the fluorescence intensity of 100 nM HP without GO, and F refers to the fluorescence intensity of 100 nM HP after the addition of various concentrations of GO. $\lambda_{ex} = 480$ nm, $\lambda_{em} = 517$ nm.31
 13. The effect of concentration of HP on the performance of the sensor. F referred to the fluorescence intensity of different concentrations of HP treated with 50.0 U/mL of Exo III followed by the addition of 20 μ g/mL GO. F0 represented the fluorescence intensity of the same series of HP without treatment of Exo III in the presence of 20 μ g/mL GO. $\lambda_{ex} = 480$ nm, $\lambda_{em} = 517$ nm.....32

14. Fluorescence spectra of sensor incubated with different concentrations of Exo III from 0 U/mL to 20.0 U/mL. (B). The plot of the fluorescence intensity with different concentrations of Exo III. The inset graph shows the calibration curve of the sensor. Reaction conditions: 100 nM HP and 20 $\mu\text{g/mL}$ GO in 100 μL 1X NEBuffer 2. $\lambda_{\text{ex}} = 480 \text{ nm}$, $\lambda_{\text{em}} = 517 \text{ nm}$	33
15. Selectivity of the sensor for Exo III over other enzymes. Reaction conditions: 100 nM HP and 20 $\mu\text{g/mL}$ GO in 100 μL 1X NEBuffer 2. The concentration of enzymes was 10.0 U/mL. $\lambda_{\text{ex}} = 480 \text{ nm}$, $\lambda_{\text{em}} = 517 \text{ nm}$	35
16. Effect of EDTA concentration on the Exo III activity. Reaction conditions: 100 nM HP and 20 $\mu\text{g/mL}$ GO in 100 μL 1X NEBuffer 2. The concentration of Exo III was 10.0 U/mL. $\lambda_{\text{ex}} = 480 \text{ nm}$, $\lambda_{\text{em}} = 517 \text{ nm}$	36
17. (A) Fluorescence spectra of the sensor upon incubation with different concentrations of Exo III in 25-times diluted FBS from 0 U/mL to 5.0 U/mL. (B) The plot of the fluorescence intensity with different concentrations of Exo III. The inset graph shows the calibration curve of the sensor. Reaction conditions: 100 nM HP and 20 $\mu\text{g/mL}$ GO in 200 μL 25-times diluted FBS. $\lambda_{\text{ex}} = 480 \text{ nm}$, $\lambda_{\text{em}} = 517 \text{ nm}$	37
18. Real-time kinetic analysis of Exo III with different concentrations. From bottom to top: 0, 0.1, 0.5, 1.0 U/mL	38
19. The Cu^{2+} induced aggregation could be reversed by introducing EDTA into solution. Reaction condition: pH 7.0, 20 mM HEPES, 0.4 mg/mL GQDs, 40 μM Cu^{2+} , 40 μM EDTA, $\lambda_{\text{ex}} = 360 \text{ nm}$, $\lambda_{\text{em}} = 470 \text{ nm}$	46
20. (a),(b) TEM images of the GQDs. (c) HRTEM image of the GQDs (0.286 nm). (d) The size distribution of the GQDs detected by DLS.....	47
21. XRD patterns of GQDs.....	47
22. (A) (a) Survey scan from 1400 eV (b) and from 700 eV. (c) Multiplex scan and fittings on C 1s peak.	48
23. The FT-IR spectra of the GQDs and Humic acid.....	49
24. (A) photographs of humic acid (b) and GQDs (a) excited under 365 nm UV light). (B) Upon excitation at 360 nm, GQDs emit fluorescence peak at 460 nm. (c) UV-vis absorption spectrum of humic (a) and GQDs (b). (D) Fluorescence spectra the excitation wavelength increased from 260 nm to 560 nm, the fluorescence emission peak shifted from 440 nm to 590 nm.	50
25. Photostability(A) and pH effect(B) of the GQDs.	51
26. Effects of different ions (20 μM) on the fluorescence intensity difference of graphene quantum dots.....	52

27. The effect of concentration of graphene quantum dots on the sensitivity of the assay. F referred to the fluorescence intensity of different concentrations of quantum dots treated with 50 μM Cu^{2+} in 20 mM HEPES (pH 5.0) $\lambda_{\text{ex}} = 360 \text{ nm}$, $\lambda_{\text{em}} = 470 \text{ nm}$	52
28. The effect of pH on the sensitivity of the assay. F referred to the fluorescence intensity of different pH of the same concentration of quantum dots treated with 50 μM Cu^{2+} in 20 mM HEPES. (pH 5.0) $\lambda_{\text{ex}} = 360 \text{ nm}$, $\lambda_{\text{em}} = 470 \text{ nm}$	54
29. Time effect on the sensitivity of the sensor. F referred to the fluorescence intensity of different pH of the same concentration of quantum dots treated with 10 μM Cu^{2+} in 20 mM HEPES (pH 5.0). $\lambda_{\text{ex}} = 360 \text{ nm}$, $\lambda_{\text{em}} = 470 \text{ nm}$	54
30. Fluorescence spectra of quantum dots incubation with different concentrations of Cu^{2+} in 20 mM HEPES (pH 5.0) from 0 μM to 300 μM . (B). The plot of the fluorescence intensity with different concentrations of Cu^{2+} . The inset graph shows the calibration curve of the sensor. $\lambda_{\text{ex}} = 360 \text{ nm}$, $\lambda_{\text{em}} = 470 \text{ nm}$. (LOD: 0.44 μM).....	55
31. (A) TEM image of SPN-Eu (500 nm) (B) TEM image of SPN-Eu (200 nm) (C) Size distribution and zeta potential (pH 7.0 10 mM HEPES) of MEH PPV SPN and MEH PPV- Eu^{3+} SPN	65
32. Increasing the particle number concentration of Eu-SPN (a: 0 P/mL, b: 5.0×10^3 P/mL, c: 1.0×10^4 P/mL, d: 2.0×10^4 P/mL, e: 5.0×10^4 P/mL).(153Eu, dwell time: 1 ms).	66
33. spICP-MS spectra of Eu-SPN in the presence of Cu^{2+} at 100 μM (a: 0 P/mL, b: 1.0×10^4 P/mL, c: 1.0×10^4 P/mL, Cu^{2+} concentrations in 100 μM).(153Eu, dwell time: 1 ms).	66
34. Fluorescence spectra of SPE-Eu under two conditions. (a) SPN-Eu (b) SPN-Eu + 100 μM Cu^{2+} , $\lambda_{\text{ex}} = 480 \text{ nm}$, $\lambda_{\text{em}} = 560 \text{ nm}$	67
35. The effect of concentration of MEH-PPV-Eu SPN on the sensitivity of the sensor. F referred to the fluorescence intensity of different concentrations of SPN treated with 100 μM Cu^{2+} in 20 mM HEPES (pH 7.0) $\lambda_{\text{ex}} = 480 \text{ nm}$, $\lambda_{\text{em}} = 560 \text{ nm}$, reaction time: 5.0 h.	68
36. Time effect on the sensitivity of the MEH-PPV-Eu SPN. F referred to the fluorescence intensity of different time period of the 1.0 ppm of MEH PPV-Eu SPN treated with 50 μM Cu^{2+} in 20 mM HEPES (pH 7.0) $\lambda_{\text{ex}} = 480 \text{ nm}$, $\lambda_{\text{em}} = 560 \text{ nm}$	69
37. The effect of pH on the sensitivity of MEH-PPV-Eu SPN. F referred to the	

fluorescence intensity of different pH of the 0.1 ppm of MEH PPV-Eu SPN treated with 100 μM Cu^{2+} at different pH in 20 mM HEPES, $\lambda_{\text{ex}} = 480$ nm, $\lambda_{\text{em}} = 560$ nm, reaction time 1.0 h.....	70
38. The effect of various Cu^{2+} concentrations on the fluorescence intensity of MEH-PPV-Eu SPN in pH 7.0 10 mM HEPES $\lambda_{\text{ex}} = 480$ nm, $\lambda_{\text{em}} = 560$ nm, reaction time 1.0 h.....	71
39. Effects of different ions (50 μM) on the fluorescence intensity difference of graphene quantum dots in pH 7.0 for 1.0 h.	72
40. spICP-MS spectra of SPN-Eu in the presence of different concentrations of Cu^{2+} (A to J: 0, 0.001, 0.1, 1, 10, 100, 1000, 10000, 100000 nM). Incubation at 25 °C for 60 min in HEPES buffer(20 mM, pH 7.0). Dilution to 1.0×10^4 particles/mL and injecting into spICP-MS(^{153}Eu , dwell time: 10 ms)	75
41. Relationship between aggregation Level and Cu^{2+} in concentration from 0.1 nM to 10000 nM.....	76
42. Selectivity of the SPN-Eu probe for Cu^{2+} detection by spICP-MS. Cu^{2+} and some other ions' concentration: 1 μM	77

LIST OF TABLES

Table	Page
1. Comparison of the proposed sensor with other fluorescent methods	34
2. Comparison of this work with other methods of GQDs.	50
3. Comparison of the spike recovery of ICP-MS methods with designed GQDs sensor	56
4. Operation parameters used for spICP-MS measurements.	61
5. Spike recovery level of spICP-MS and fluorometric methods for Cu ²⁺ detection in river water	78

LIST OF SCHEMES

Scheme	Page
1. Schematic illustration of the DOX-loaded rGO@msilica nanocarrier as a multifunctional drug delivery system for synergetic chemo-photothermal therapy of cancer.	10
2. Schematic illustration of the Exo III detection based on the GO and FAM-labelled HP	28
3. Schematic illustration of the formation of GQDs and its application for Cu ²⁺ detection.....	45
4. Schematic illustration of Cu ²⁺ detection by Eu coordinated MEH-PPV semiconducting polymer nanoparticles.....	64

ACKNOWLEDGEMENTS

It has been five years since the first time I came to Dr. Zhao's group to begin my Ph.D program. After I finished my first year in UND, I have vividly conceived the difficulties and conflicts I might face in the following years. Luckily, I have been offered a lot of help from our group. I would say I might never have been able to finish my Ph.D study and dissertation without the guidance of my committee members, the help from friends, and the support from my family.

I would always remember every moment involved with Dr. Zhao, my most adorable and loving advisor, my deepest gratitude generates and accumulates from every guidance she offered me. The irradiation from her caring, patience and spirit has been shining in my whole study life at the University of North Dakota. When I first came here, she encouraged me to face my fear and treat my life seriously. I was awakened by her and started to target my goal to become an instructor, a chemist and an independent thinker. For everything she imparted to me, I will never ever forget it. I would also like to thank all of my committee members: Dr. David T. Pierce, Dr. Alena Kubátová, Dr. Kathryn A. Thomasson, and Dr. Nuri Oncel. I thank Dr. Pierce for letting me realize my distance and weakness on the research, for his guidance and support during my project. I was raised up with a meticulous mind on presentation, which provided me a more competitive ability for future interview and job searching. I thank Dr. Alena Kubátová for providing me opportunities to participate in all the outreach activities, through which I learned how to be a good educator and scientist. Dr. Kathryn A. Thomasson, I learned a lot of courage from you, your positive attitude and strong determination will always a beacon for me to face my future uncertainties and

difficulties. I would also like to thank Dr. Nuri Oncel for helping me and pointing out my wrong decisions on project, it is a great honor that we worked together in Fargo for the summer academy; working with you is very enjoyable and relaxed. In particular, I would like to thank Dr. Xu Wu for helping me in every little details of my project, learning from him would clear the blurry and improve the accuracy in the experiment, which made me understand the value of absolute professionalism. I am really grateful for the extra time and patience he provided.

I would like to thank all of my friends who have been very kind enough to extend their help at various phases of my research and Ph.D study. Yuqian Xing, Shaina Strating, Juan Han, Wen Sun, Yingfen Wu, Sarah Reagent, thanks for their support in a very special way. I learned a lot from them through their personalities and the scholarly interactions with them helped me a lot. Their suggestions at various points of my research clear my mind and help me to think in a different way. They are more like my family members who always support me go through all the difficulties.

I am truly grateful for the financial support I received from the UND Graduate School, ND EPSCoR, and UND Chemistry Department. Without their financial support, I could never make it so far. Meanwhile, I appreciate the technical support from the Basic Science Imaging Center for training me on the microscopes and allowing me to use these instruments independently.

Finally, and most importantly, I would like to thank my parents for their support, encouragement, patience and unwavering love in the past five years. I thank them for their faith in me.

ABSTRACT

Graphene-based nanomaterials are novel emerging materials with their superior physical, chemical and mechanical features that have applications in a broad diversity of fields. Their excellent properties include: 1) Superior biocompatibility compared to the traditional QDs because they are free from toxic heavy metals. 2) Large surface area and easy covalent/chemical modification which makes them convenient as drug delivery carriers, in comparison with liposomes. 3) High light absorption in the near infrared (NIR) region. Compared to metal nanoparticles, which gives them better photothermal properties. 4) Strong quenching efficiency; graphene-based nanomaterials were able to quench various fluorophores through fluorescence resonance energy transfer (FRET). 5) Biofunctionalization; graphene-based materials display excellent capabilities for direct binding with biomolecules. Considering these significant properties, this dissertation work focuses on the development of graphene-based nanomaterials and applications of these nanomaterials in different fields. A total of four projects are presented.

In the first project, a multi-modal therapeutic drug delivery system was developed for cancer therapy. A reduced graphene oxide coated with mesoporous silica (rGO@msilica) nanocarrier was designed for chemo-photothermal therapeutic capacity. The inner layer of the rGO served as a photothermal agent while the outer layer of the mesoporous silica acted as a pH-triggered drug carrier. Doxorubicin (DOX) was loaded into the mesoporous silica vehicle as a chemotherapy agent. In the acidic environment, DOX was gradually released from the nanocarrier to fulfill the chemotherapeutic function. Meanwhile, rGO@msilica showed a strong photothermal (PTT) effect under

a NIR irradiation, generating synergistic therapeutic efficiency for destroying cancer cells.

In the second project, a “turn-on” fluorescence method was developed for monitoring exonuclease III enzymatic activity based on the interaction between graphene oxide (GO) and a DNA hairpin probe (HP). In the absence of Exo III, the strong π - π interaction between the fluorophore-tagged DNA and GO caused efficient fluorescence quenching via FRET. In the presence of Exo III, the fluorophore tagged 3'-hydroxyl termini of DNA probe was digested to set the fluorophore free from adsorption by GO, causing less fluorescence quenching. This simple GO-based probe showed highly sensitive and selective linear response in the low detection range from 0.01 U/mL to 0.5 U/mL and with a limit of detection (LOD) of 0.001 U/mL. Compared with other fluorescent probes, this assay exhibited superior sensitivity and selectivity in both buffer and fetal bovine serum samples. The assay was also low cost and easy to set up.

In the third project, humic acid, a new carbon source was used to fabricate graphene quantum dots (GQDs) by an easy one pot hydrothermal reaction. The morphology of the blue emission graphene quantum dots was characterized by high resolution transmission electron microscopy (HRTEM) and dynamic light scattering (DLS). The results showed crystalline lattice spacing of 0.286 nm and a hydrodynamic diameter of 6.6 nm. X-ray photoelectron spectroscopy (XPS) and FT-IR have demonstrated diverse functional groups on the GQDs, which yielded strong chelating interactions with Cu^{2+} . The optical properties of GQDs were characterized by photoluminescence (PL) spectra and ultraviolet-visible (UV-Vis) spectroscopy. Both showed that the GQDs had an excitation-dependent fluorescence behavior and a large stoke shift with maximum excitation/emission wavelength at 340/470 nm. These

properties will provide a useful signal for fluorometric methods of analysis. Furthermore, the GQDs showed a good photostability and a relative high quantum yield of 20%, which is adequate to serve as a bioimaging probe. Metal ion selectivity studies indicated that the GQDs could be applied as Cu^{2+} sensing nanoprobe for drinking water in the linear range from 1 μM to 40 μM and a low LOD of 0.44 μM . Overall, this work provided a simple method to produce GQDs as well as a Cu^{2+} sensing nanoprobe with low cost raw materials humic acid, which would be a great improvement in biomedical fields.

In the fourth project, Eu^{3+} coordinated polymer nanoparticles based on poly[2-methoxy-5-(2-ethylhexyloxy)-1,4-phenylenevinylene] (MEH PPV-Eu) were developed and used for Cu^{2+} detection. The designed MEH PPV-Eu probe has both fluorescence signal from the conjugated polymer and the Eu signal detected by spICP-MS. Cu^{2+} were proven to have efficient chelating interactions with carboxylic groups, which resulted in a significant fluorescence quenching due to aggregation. The aggregation increased the Eu intensity per particle and was also quantified by single-particle inductively coupled plasma mass spectrometry (spICP-MS). For the fluorometric method, it obtained a linear range from 2 μM to 50 μM and a LOD of 0.29 μM . For the spICP-MS method, it achieved a lower LOD of 0.42 pM and a wider linear range from 1.0×10^{-3} nM to 1.0×10^4 nM. This combination assay will provide a rapid and fast approach with an extremely low detection limit, indicating its superior potential in environmental analysis.

CHAPTER I

REDUCED GRAPHENE OXIDE/MESOPOROUS SILICA NANOPARTICLES FOR pH-TRIGGERED DRUG RELEASE AND PHOTOTHERMAL THERAPY

1. Introduction

Cancer is a terrifying health threat to human beings worldwide.¹ Up to now, multiple therapeutic strategies have been developed. Chemotherapy, which uses drugs to attack tumor cells, has been widely applied. However, non-specific drug delivery causes considerable side effects to patients, which limits their applications.² Therefore, it is urgent to develop a controllable drug release system that effectively targets malignant tissue regions.³ Traditional drug carriers have relied on blood circulation to proceed the medication process, which is a passive and lacks specificity.⁴ Nowadays, active drug delivery systems are being developed to respond to certain environmental stimuli, such as light, pH, and thermalization.⁵⁻⁹ Compared with passive drug carriers, active carriers have controllable loading and releasing systems which response to internal or external stimulations. As a result, the drug targeting efficiency has been enhanced significantly and healthy cells have been protected.³

Among the stimuli used for active drug release, the pH-responsive drug delivery system shows promising functions in the field of chemotherapy.¹⁰ In general, cancer cells have a feature of unlimited proliferation; thus, they contribute to over-oxygen consumption and an acidic microenvironment compared to healthy tissues.¹¹⁻¹² The lower pH value can be utilized as a stimulus to design active drug delivery carriers for chemotherapy.¹⁰ In this regard, nanomaterials could be applied as active drug carriers since their surface can be easily modified to be pH-responsive.¹³ The functional groups on the nanomaterials can be protonated or deprotonated according to pH of the environment and used to control the drug release.¹⁴ For example, the carboxylic acid groups controlled the deformation of polymeric nanocapsules.¹⁵ In a basic medium, the

carboxyl groups were deprotonated, and the electrostatic attraction between the drug and the carrier limited the drug release. However, in an acidic medium, the carboxyl groups were protonated so that charged molecules had less resistance to transport through the nanocapsules, resulting in the drug release. The charge variation weakened the interactions to the drugs, which directly regulated the loading and releasing behavior of drugs, which implied one of the designations in pH-mediated drug delivery.¹⁶ Using electrostatic interactions to initiate drug release has been considered as a major pathway for developing pH-responsive active drug delivery system.¹⁷

In the development of nanomaterial-based pH-responsive drug delivery systems, several types of nanovehicles have been used, including polymer nanocarriers,¹⁸⁻¹⁹ dendrimers,²⁰ lipids,²¹⁻²² gold nanocarriers,²³ carbon nanotubes^{16, 19} and mesoporous silica nanocarriers.²⁴ Drugs were attached on those nanomaterials²⁵, loaded into their pores, or encapsulated into vacant domains of nanocarriers.²⁶ Among them, mesoporous silica nanocarriers attracted considerable attention due to their decent biocompatibility, easy surface modification, high drug loading efficiency, and good drug release pattern.^{8, 27-28} Accordingly, mesoporous silica is an excellent candidate for drug loading and releasing nanocarriers in cancer therapies.²⁹⁻³²

Furthermore, multi-modal therapeutic strategies have been promoted due to the development of nanomaterials.³³ By combining different therapeutic modalities, such as photodynamic therapy (PDT), photothermal therapy (PTT), radiotherapy, and immunotherapy, the synergistic effect was provided an impressive therapeutic outcome.³⁴⁻³⁹ Photothermal therapy is a non-invasive, convenient and promising physical treatment for tumor cells. Several synthesized and modified high-quality photothermal agents have been studied.⁴⁰⁻⁴¹ Graphene-based nanomaterials, especially reduced graphene oxide, have been used for photothermal therapy due to their high

photothermal conversion efficiency.⁴²⁻⁴⁶ For example, reduced graphene oxide that was coated with a temperature-responsive polymer layer has been successfully applied in a controllable drug release system triggered by a near-infrared (NIR) irradiation.⁴⁷ Besides, Liu's group selected a polymer layer to wrap graphene oxide, forming a stable and biocompatible photothermal agent.⁴⁴ Inspired by these works, we designed a bifunctional nanocarrier using mesoporous silica matched with reduced graphene oxide (rGO@msilica) for cancer treatment.

In this work, the designed sandwich structure of rGO@msilica nanocarrier has both chemo and photothermal therapeutic capacities. The inner layer of the reduced graphene oxide served as a photothermal agent owing to its superior NIR absorption and photo thermal conversion efficiency.⁴³ In the outer layer, the mesoporous silica acted as a drug container. A chemotherapeutic agent, doxorubicin (DOX), was loaded into the mesoporous silica carrier and adsorbed onto the rGO *via* noncovalent interactions at neutral pH environment. In the acidic environment, DOX was gradually released from the nanocarrier to fulfill the chemotherapeutic function. Meanwhile, rGO@msilica showed a strong PTT effect under a NIR irradiation, which generated synergistic therapeutic efficiency for destroying cancer cells. The developed bifunctional nanocarriers might be an effective pH-responsive drug carrier for cancer therapy.

2. Experimental Section

2.1. Chemicals.

Graphene oxide aqueous solution (GO, 5.0 mg/mL) was purchased from ACS Materials. The following chemicals were purchased from Sigma-Aldrich Inc. and used

as received without further purification. They were doxorubicin hydrochloride (DOX, $C_{27}H_{29}NO_{11} \cdot HCl$, 98%), tetraethyl orthosilicate (TEOS, $C_8H_{20}O_4Si$, 98%), sodium hydroxide (NaOH, 98%), hexadecyltrimethylammonium bromide (CTAB, $CH_3(CH_2)_{15}N(Br)-(CH_3)_3$, 96%), dimethyl sulfoxide (DMSO, $(CH_3)_2SO$, 99.9%), hydrazine hydrate (N_2H_4 , 50%-60%) and hydrochloric acid (HCl, 36.5%-38%), ethanol (C_2H_5OH , 99.8%), 3-(4,5-Dimethylthiazol-2-yl)-2,5-diphenyltetrazolium bromide (MTT, $C_{18}H_{16}BrN_5S$, 98%). The deionized (DI) water (18.2 M Ω ·cm) was obtained from a Millipore water purification system. Dulbecco's modified eagle's medium (DMEM), Leibovitz's L-15 medium (L-15) and 4'-6-diamidino-2-phenylindole (DAPI, $C_6H_{15}N_5$) were purchased from ThermoFisher Scientific Inc. Colon cancer cell line (SW620) was provided by MD Anderson Cancer Center. Lung cancer cell line (A549) was purchased from the American Tissue Culture Collection (ATCC). Both cells were cultured in the School of Medicine and Health Sciences in the University of North Dakota at 37 °C with 5% CO₂.

2.2. Instruments.

An Eppendorf 5804 centrifuge (Eppendorf, Hamburg, BRD) and an ultrasonicator (Branson, Buffalo Grove, IL, USA) were used to separate and disperse nanocarriers. The hydrodynamic diameters and surface potential of the nanocarriers were characterized by the Zetasizer Nano ZS (Marlwen, Worcestershire, UK). A Hitachi SU8010 field emission Scanning Electron Microscope (Hitachi, Tokyo, Japan) was used to take the TEM image of rGO. A Hitachi 7500 Transmission Electron Microscope (Hitachi, Tokyo, Japan) and JEOL JEM-2100 high-resolution transmission electron Microscope (JEOL Ltd., Tokyo, Japan) were employed to image the structure of mesoporous silica layer. The pore size and surface area of the nanocarriers were measured by an autosorb-iQ gas sorption analyzer (Quantachrome Instruments,

Boynton Beach, FL, USA). The absorption and fluorescence spectra were obtained by a PerkinElmer Lambda 1050 UV/VIS/NIR spectrometer (PerkinElmer, Santa Clara, CA, USA) and a Jobin Yvon Horiba Fluorolog-3 Spectrofluorometer (Horiba Scientific, Edison, NJ, USA), respectively. A BWF1 series fiber-coupled diode laser system (808 nm, B&W TEK Inc., Newark, DE, USA) was utilized to irradiate the nanocarrier for executing photothermal therapy. The temperature was monitored with a SK-1250MC electronic thermometer (Sato Keiryoki, Tokyo, Japan). A Multiskan spectrum spectrophotometer (ThermoFisher Scientific, Waltham, UK) was employed to perform MTT test for measuring the optical density at 570 nm in dimethyl sulfoxide (DMSO) solution.

2.3. Synthesis of the Reduced Graphene Oxide / Mesoporous Silica Nanocarrier (rGO@msilica).

The rGO@msilica nanocarrier was prepared by the following steps. In the beginning, 50.0 mL of deionized water was mixed with 1.0 mL of 5.0 mg/mL GO aqueous solution, followed by 30 min of sonication. The solution was centrifuged at 7,000 rpm for 30 min to remove the precipitate. Afterwards, 500 mg of CTAB and 20 mg of sodium hydroxide were added into the previous solution, followed by sonication for 3 h to build a basic condition for hydrolysis of TEOS. Then, an aliquot of 250 μ L of TEOS was added into the above solution and stirred for 7 h in a 40 °C water bath. The obtained nanocarrier solution was refluxed in 50 mL HCl/EtOH solution (0.1%, v/v) for 3 h to remove the excess CTAB, followed by washing with ethanol and water. The precipitate was re-dispersed in 50 mL water. An aliquot of 80 μ L of hydrazine hydride was added and stirred at 100 °C overnight. The final rGO@msilica was washed with water and ethanol (each for three times) and dried in an oven (80°C) for future usage. The GO@msilica nanocarrier was prepared as a control group following the

same procedure mentioned without the reduction process by hydrazine hydride.

2.4. Measurement of Pore Size and Surface Area.

The obtained dry rGO@msilica nanocarrier was loaded into a 12-mm sample cell in the autosorb-iQ gas sorption analyzer. Before this loading, the weight of the empty sample cell with glass and glass rod was measured. Then, the loaded cell was put into a heating mantle for degassing at the temperature of 120 °C for 2 h. After degassing, the sample was re-weighed. Then the loaded cell was transferred into the analysis port. The isotherm curve (volume absorbed vs relative pressure) was plotted, and the pore size and the surface area were obtained.

2.5. Measurement of Drug Loading and Releasing Efficiency.

An aliquot of 2.0 mL of 1.5 mg/mL rGO@msilica nanocarrier aqueous solution was mixed with 24 µL of 5.0 mg/mL doxorubicin (DOX) and 2.0 mL of 20 mM PBS buffer (pH=7.4) at room temperature for 24 h. Drug loading efficiency was calculated by measuring the fluorescence intensity of the original solution and the supernatant after centrifugation (11,500 rpm, 15 min). Furthermore, the pH-dependent drug release behavior of the nanocarrier was investigated under pH 7.4 and pH 5.0. Briefly, two aliquots of 1.0 mL of 0.75 mg/mL of DOX-loaded rGO@msilica nanocarriers were adjusted to two different pH values, pH 5.0 and pH 7.4, in a PBS buffer. At different time interval, the solution was centrifuged at 11,500 rpm for 15 min. Then, the supernatant was collected for fluorescence measurement, which was used to calculate the amount of DOX with a prepared calibration curve. Similarly, the photoresponsive release of DOX under a NIR irradiation was evaluated in different pH solutions. The initial temperature was adjusted at 37 °C using a water bath. The cuvette was exposed to a NIR diode laser (0.3 W/cm²) for 15 min and cultivated for different period of intervals, including 1 h, 2 h, 3 h, 4 h, 5 h and 6 h.

2.6. Photothermal Effect of rGO@msilica.

To evaluate photothermal effect of the GO@msilica nanocarrier and rGO@msilica nanocarrier, the temperature of an aliquot of 2.0 mL of GO@msilica nanocarrier (0.1 mg/mL) and rGO@msilica nanocarrier (0.1 mg/mL) under an NIR laser (808 nm, 0.3 W/cm²) irradiation were recorded by an electronic thermometer.

2.7. Biocompatibility of rGO@msilica Nanocarrier.

A549 lung cancer cells (5.0×10^4 cells/well) were incubated in a DMEM cell culture medium in a humidified atmosphere with 5% of CO₂ at 37 °C for 24 h.⁵⁰ The cells were rinsed with a PBS buffer and then treated with different concentrations of unloaded rGO@msilica nanocarriers (0, 2.5, 2.5×10^{-2} , 2.5×10^{-3} , 2.5×10^{-4} , and 2.5×10^{-5} mg/mL) for 24 h in a DMEM medium. The cells were washed to remove the physically adsorbed nanocarriers, then an MTT solution (5.0 mg/mL, 10 μL) was subsequently added into each well for incubation of 4.0 h. After the medium was removed, DMSO was added to dissolve the formed formazan violet crystals. The absorbance of formazan in DMSO solution was detected by a microplate reader at 570 nm. A different cell line (colorectal cancer cells SW620)⁵¹ has been used to validate the biocompatibility as well.

2.8. Chemotherapeutic Effect of the DOX-loaded rGO@msilica Nanocarrier.

A549 lung cancer cells (5.0×10^4 cells/well) were incubated in DMEM cell culture medium in a humidified atmosphere with 5% of CO₂ at 37 °C for 24 h. Then, the cells were treated with different concentrations (0, 2.5×10^{-5} , 2.5×10^{-4} , 2.5×10^{-3} , 2.5×10^{-2} , 2.5×10^{-1} , and 2.5 mg/mL) of DOX-loaded rGO@msilica nanocarriers for 12 h in a DMEM medium. An MTT assay was performed to measure the cell viability after the treatment. Furthermore, the impact of incubation time on the cell viability was investigated by MTT assay. Briefly, A549 cells were cultured with DOX loaded rGO@msilica nanocarriers (25 μg/mL) for various time periods (0 h, 3 h, 12 h, 24 h,

30 h, 36 h, and 42 h), followed by the MTT assay to assess the cell viabilities.

2.9. Confocal Fluorescence Imaging of Drug Release in Cancer Cells.

A549 cells (2.0×10^5 cells/well) were incubated in the cell culture medium in a humidified atmosphere with 5% of CO₂ at 37 °C for 24 h in a 24-well cell culture plate. Afterwards, an aliquot of 500 μL of DOX-loaded rGO@msilica nanocarrier dispersed in the culture medium (25 μg/mL) was added into the above cell culture plates. The cells were incubated at 37 °C for 10 min, 6 h and 24 h, respectively. Cell nuclei were stained by 300 nM DAPI solution. After washing the cells with PBS buffer to remove the excess DAPI and DOX-loaded rGO@msilica nanocarrier, the fluorescence imaging was taken with a confocal fluorescence microscope.

2.10. Synergistic Therapeutic Efficiency.

The synergistic therapeutic efficiency of DOX-loaded rGO@msilica nanocarrier was evaluated using A549 cells and SW620 cells. First, the A549 cells (5.0×10^4 cells/well) were seeded on a 96-well plate and cultured for 24 h. Five different treatment groups, including the control group, pure rGO@msilica (25 μg/mL), DOX-loaded rGO@msilica (25 μg/mL), rGO@msilica (25 μg/mL) with irradiation, and DOX-loaded rGO@msilica (25 μg/mL) with and irradiation, were used to assess the synergistic therapeutic efficiency. For the irradiation, an 808 nm laser with a power density of 0.3 W/cm² was used for 15 min. After the treatments, the cells were incubated for another 6 h or 24 h, followed by the measurement of cell viability using MTT assay. The therapeutic effect was also validated in SW620 cells using the same protocol.

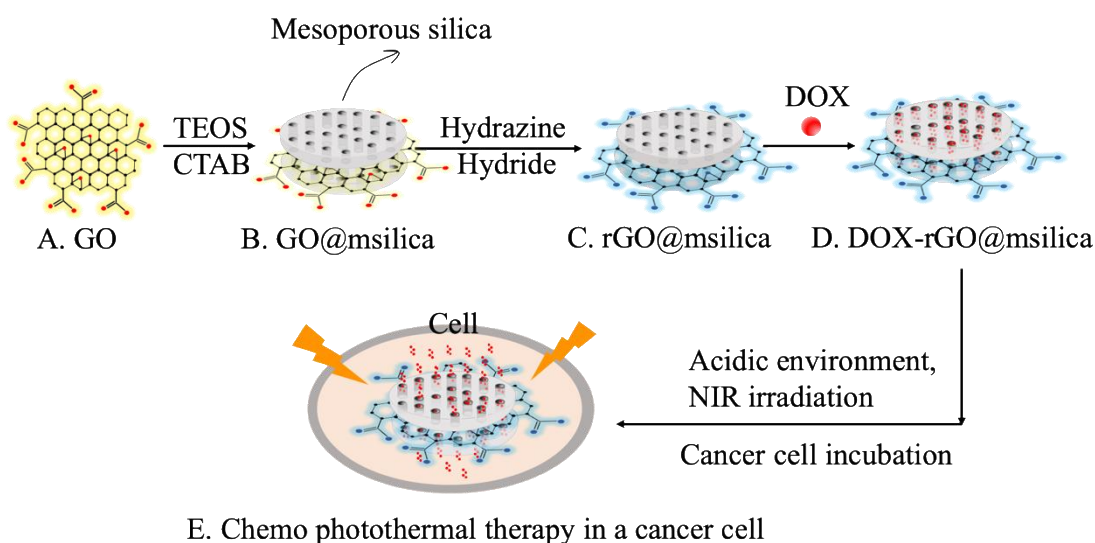
3. Results and Discussion

3.1. Design and Synthesis of the DOX-Loaded rGO@msilica Nanocarrier.

The design of the bifunctional DOX-Loaded rGO@msilica nanocarrier was illustrated in Scheme 1. Although multifunctional drug delivery systems have been

developed by many research groups, the DOX-loaded rGO@msilica nanocarrier developed in this work have the following three main features. First of all, the usage of rGO not only provides a powerful photothermal agent to ablate cancer cells with the irradiation of NIR laser, but also works as the controllable drug carrier for DOX.⁴⁴ The large sp^2 carbon clusters in rGO efficiently load hydrophobic drugs, like DOX, through π - π stacking under the normal environment.⁴⁸⁻⁴⁹ However, when the environment becomes acidic, the amine groups and carboxyl groups on rGO are protonated, resulting the strong repulsive force between the positive charged DOX and rGO.⁵⁰⁻⁵¹ This enhanced repulsive force will trigger the drug release from the nanocarrier. Moreover, under the NIR laser irradiation, the acidic triggered drug releasing efficiency was accelerated by the elevated temperature. Second, the mesoporous silica layers have three important functions in this design. With the protection of the mesoporous silica layers, rGO become more stable than the pure rGO without any modification. Also, the excellent biocompatibility of silica ensures the low cytotoxicity of the nanocarrier for drug delivery. More importantly, the mesopores in the silica layer provide an ideal container for drugs, which could be easily triggered to release in the acidic environment.⁵²⁻⁵⁴ Third, the synergistic effect by the two cancer killing mechanisms, including photothermal ablation and acidic triggered chemotherapy greatly enhanced

the therapeutic efficiency for cancer treatment.



Scheme 1. Schematic illustration of the DOX-loaded rGO@msilica nanocarrier as a multifunctional drug delivery system for synergetic chemo-photothermal therapy of cancer.

To prepare the nanocarrier, mesoporous silica was firstly coated on the surface of a single layer GO (Scheme 1 A) by the hydrolysis of TEOS with assistance of CTAB in an alkaline environment, forming a sandwich structure (Scheme 1B). Then, the inner GO was reduced by hydrazine hydrate to form the reduced graphene oxide (rGO, Scheme 1 C). Thereafter, a chemotherapeutic drug, doxorubicin hydrochloride (DOX),⁵⁵⁻⁵⁸ was loaded into the pores of mesoporous silica layer and the surface of rGO (Scheme 1 D) through electrostatic interaction and π - π stacking. Triggered by the acidic tumor microenvironment, DOX would be released for chemotherapy, which would also be enhanced by the photothermal effect under a NIR laser irradiation (Scheme 1 D).

3.2. Characterization of the DOX-Loaded rGO@msilica Nanocarrier.

The morphology and size of rGO@msilica nanocarrier was characterized with a regular transmission electron microscope (TEM) and a high-resolution transmission electron microscope (HRTEM). Without mesoporous silica coating, the pure rGO surface was smooth and no pores structure was observed (Figure 1A). After the formation of the rGO@msilica sandwich structure, the TEM image (Figure 1B) clearly

demonstrated the existence of mesopores silica with the lateral size around 300-500 nm. The HRTEM image (Figure 1C) showed the average pore size of mesoporous silica was about 3 nm.

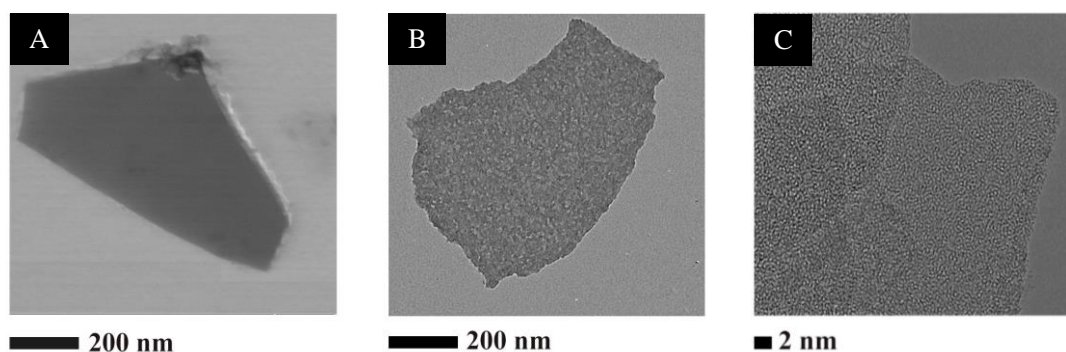


Figure 1. TEM images of rGO@msilica nanocarrier. (A) A pure rGO sheet. (B) low magnification TEM image of rGO@msilica nanocarrier (300 - 500 nm). (C) HRTEM image of rGO@msilica nanocarrier.

Furthermore, the composition of the synthesized rGO@msilica nanocarriers was investigated using energy-dispersive X-ray spectroscopy (EDS) equipped on a SEM. The elemental mapping from EDS showed the overlapping images of elements of C, Si, and O as designed (Figure 2). However, due to the low content of N in the rGO@msilica, no element N map was obtained.

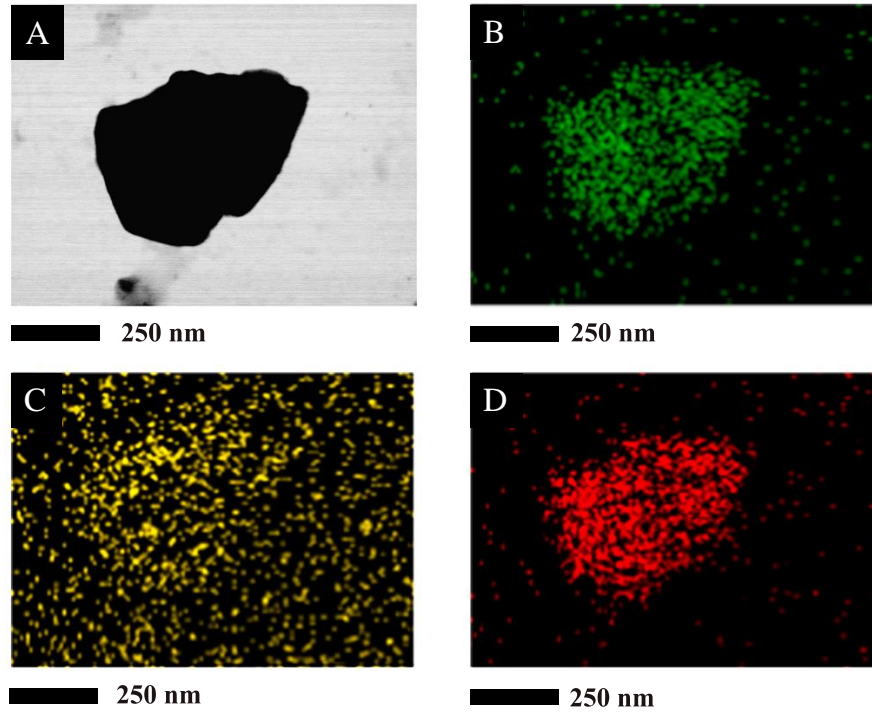


Figure 2. Elemental analysis of the of rGO@msilica nanocarriers. STEM image of the rGO@msilica nanocarrier (A) and its corresponding elemental maps of Si (B, green color), carbon (C, yellow color), and oxygen (D, red color) (scale bar = 250 nm).

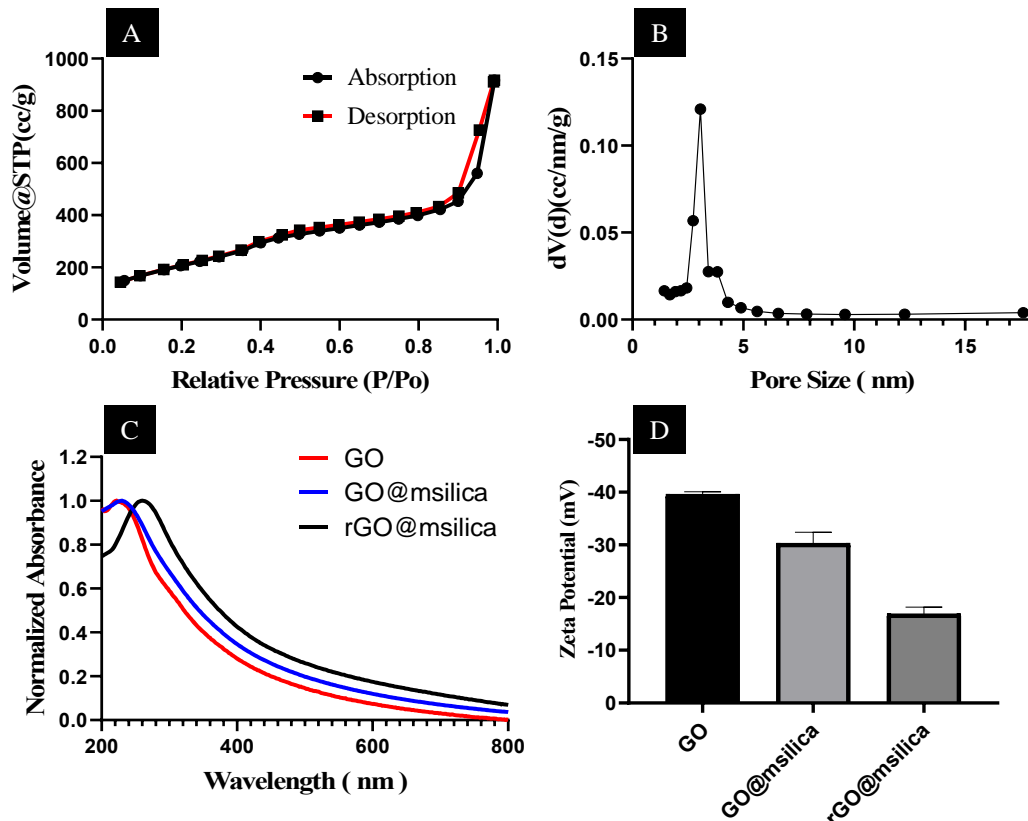


Figure 3. Nitrogen adsorption-desorption isotherm curve (A) and the pore size distribution (B) of rGO@msilica nanocarriers based on BJH method. The outgas was conducted at 120 °C for 1.2 h. (C) Absorption spectra of GO, GO@msilica and rGO@msilica nanocarrier. (D) Zeta potential of GO, GO@msilica and rGO@msilica

nanocarrier in pH 5.0, 10 mM PBS buffer at room temperature.

The surface area and pore sizes of the rGO@msilica were further measured using a surface area analyzer. The results of N₂ adsorption-desorption isotherm (Figure 3A) and the pore size distribution curve (Figure 3B) indicated that the rGO@msilica nanocarrier possessed a large BET surface area (770 m²/g). A computational mechanical modeling method, BJH method (Barrett, Joyner, and Halenda), was employed for calculating the pore size distribution from the experimental isotherms using the Kelvin model of pore filling. The pore volume was 1.21 cm³/g and the average pore size was estimated as 3.1 nm, which was consistent with the result from the HRTEM images.

To further confirm the formation of the rGO@msilica nanocarrier, we also monitored the absorption spectra (Figure 3C) during the synthetic process. The absorption peaks of GO and GO@msilica nanocarrier were both at 230 nm, which was the characteristic peak of GO. After reduction, the peak was shifted to 260 nm, indicating the formation of rGO. Meanwhile, the absorbance in the NIR range was significantly enhanced when GO was reduced to rGO, which was useful for PTT using NIR laser. Moreover, zeta potentials of GO, GO@msilica and rGO@msilica nanocarrier were measured, which were -39.6 ± 0.5 mV, -30.3 ± 2.1 mV, and -16.8 ± 1.3 mV, respectively (Figure 3D). By coating GO with mesoporous silica, the zeta potential decreased, but kept relatively large negative charge due to the formation of the -OH groups on silica surface. With the formation of rGO, the surface oxygen-containing groups of GO were partially removed, resulting in the further decrease of the zeta potential. Overall, the negative charge surface of rGO@msilica nanocarrier ensured the good stability of the nanocarrier in buffer and medium for bioapplications.

3.3 Drug Loading.

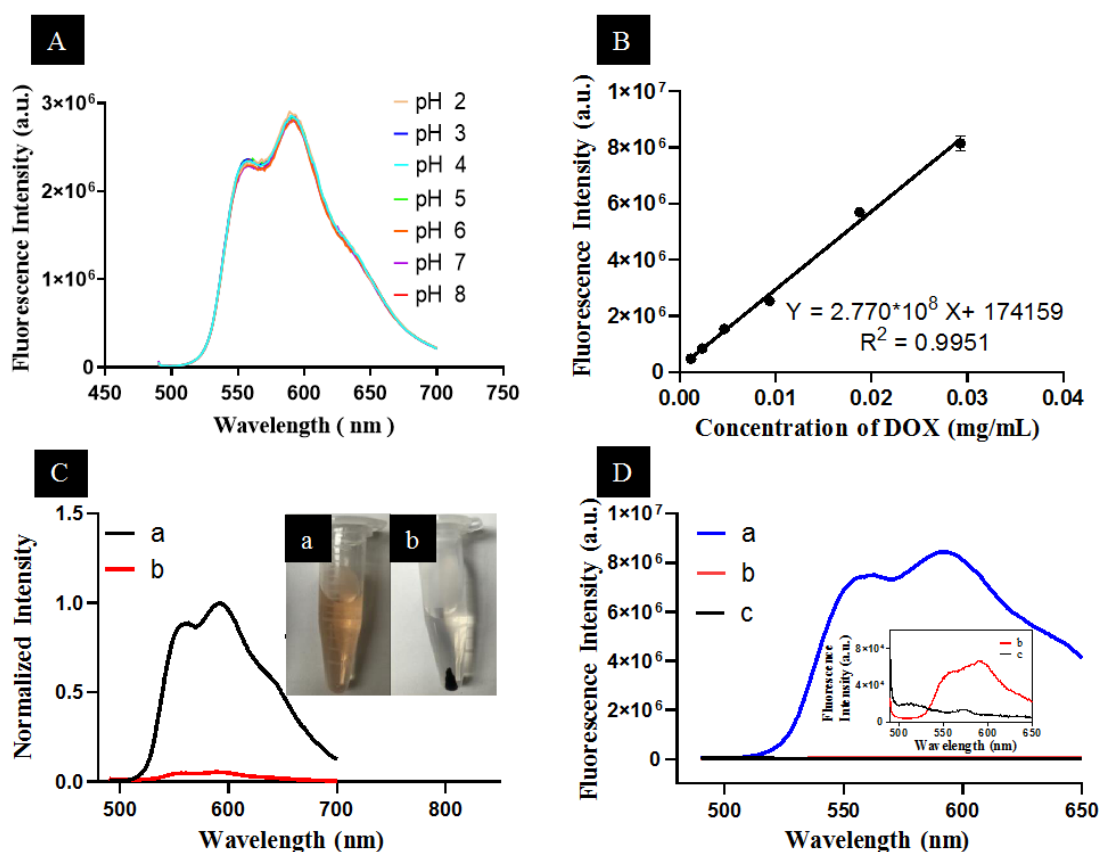


Figure 4. DOX loading into rGO@msilica nanocarrier. (A) The fluorescence spectra of DOX (0.01 mg/mL) at different pH values. (B) Calibration curve of DOX in 10 mM pH 7.4 PBS buffer (DOX concentration: 3.0×10^{-2} , 2.0×10^{-2} , 1.0×10^{-2} , 5.0×10^{-3} , 2.5×10^{-3} , 1.3×10^{-3} mg/mL). (C) Fluorescence spectra of initial pure DOX solution to be used for loading (curve a) and the supernatant after centrifuging DOX-loaded rGO@msilica nanocarrier (curve b). Inset shows the initial pure DOX solution (a) and the DOX-loaded rGO@msilica nanocarrier solution after centrifugation (b). (D) The fluorescence spectra of (a) pure DOX (3.0×10^{-2} mg/mL), (b) 7.5×10^{-1} mg/mL DOX-loaded rGO@msilica nanocarriers (with equivalent DOX concentration of 2.7×10^{-2} g/mL) in 10 mM pH 7.4 PBS buffer (c) and pure 10 mM pH 7.4 PBS buffer solution as control. Excitation wavelength: 480 nm, Emission wavelength: 591 nm.

One of the most important criteria for a successful stimuli-responsive drug delivery platform is that the loaded drug should be released only under the desired conditions with minimal nonspecific leakage. Due to the strong fluorescence of DOX, we used the fluorescence intensity of DOX to measure the loading efficiency and monitor the drug releasing behavior. To avoid false signals caused by the fluorescence variation of DOX, we first studied the pH effect on the fluorescence intensity of the pure DOX molecules. The results showed that DOX was insensitive to pH in the range

of 2 to 9 (Figure 4A).

The pH insensitive feature of DOX ensured the accuracy of the measurement of DOX by fluorescence intensity in this work. Therefore, a calibration curve based on the concentration of DOX and fluorescence intensity was established to quantify DOX in different environment (Figure 4B). To calculate the drug loading efficiency, a certain amount of DOX was loaded to the rGO@msilica nanocarrier as described in the experimental section. The drug loading efficiency was measured by the detection of the fluorescence intensities of the initial pure DOX solution (Figure 4C, curve a) and the supernatant after centrifuging the DOX-loaded rGO@msilica nanocarrier (Figure 4C, curve b). The loading efficiency was calculated to be 90% and the loading amount was 36.0 mg DOX/g nanocarrier. Interestingly, after loading DOX into rGO@msilica nanocarrier, the fluorescence of DOX was strongly quenched by rGO due to its universal fluorescence quenching ability, indicating the successful drug loading. As shown in Figure 4D, the fluorescence intensity of DOX-loaded rGO@msilica was only 1% of the original pure DOX solution.

3.4. pH-Responsive Drug Release.

Upon the successful loading of DOX into the rGO@msilica nanocarrier, the feature of the pH-triggered drug release behavior was investigated. Two pH values, including pH 7.4 and pH 5.0, were selected for the investigation. By monitoring the fluorescence intensity changes of the supernatant of the DOX-loaded rGO@msilica nanocarriers after centrifugation, the amount of released DOX was measured. As shown in Figure 5A, only 4.8% of the loaded DOX was released in the PBS buffer with pH 7.4 without NIR laser irradiation in the first 6 hours. In contrast, a significantly large amount of DOX (38.0 %) was released from the DOX-loaded rGO@msilica nanocarrier when the pH was changed to 5.0, indicating the accelerated drug releasing

profile triggered by the acidic environment.

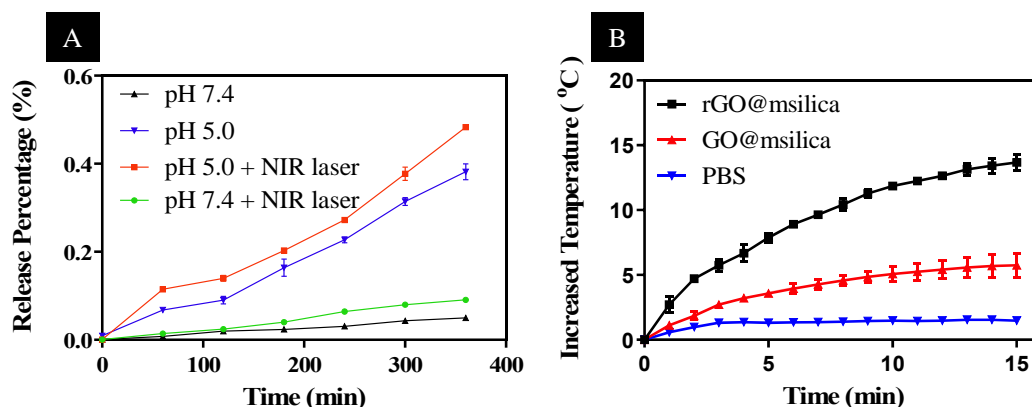


Figure 5. (A) Cumulative release of DOX from DOX-loaded rGO@msilica (1.0 mg/mL) within different pH buffers with or without irradiation. An NIR laser (808 nm, 0.3 W/cm²) was used for irradiation. (B) Temperature increasing curves of PBS, GO@msilica nanocarrier (0.5 mg/mL) and rGO@msilica nanocarrier (0.5 mg/mL) solutions exposed to an NIR laser (808 nm, 0.3 W/cm²) for 15 min. The solution volume was 2.0 mL.

Due to the enhanced NIR absorbance of rGO@msilica nanocarrier and the reported PTT effect of rGO, we also investigated the temperature change of the rGO@msilica nanocarrier under the 808 nm laser irradiation. The temperature of the rGO@msilica nanocarrier solution was monitored under the irradiation of an 808 nm laser (0.3 W/cm²) for 15 min (Figure 5B). Without the nanocarrier, the temperature of the PBS increased less than 0.5°C under the same irradiation (Figure 5B). In contrast, the temperature changes of GO@msilica nanocarrier solution (0.5 mg/mL) only elevated 4 °C (Figure 5B). Significantly, the temperature changes of the rGO@msilica nanocarrier solution (0.5 mg/mL) exceeded 14 °C (Figure 5B) with the irradiation. Therefore, the inner layer rGO of the nanocarrier contributed to the higher photothermal effect, which was also consistent with the enhanced absorption in the NIR range of rGO (Figure 3C). Considering that the normal human body temperature is about 37°C, the final temperature caused by rGO@msilica with irradiation could be over 51°C, which would be high enough to kill most of the malignant cells.

More importantly, we proposed that the acid-triggered drug releasing rate

would be increased attributing to the enhanced diffusion speed at a higher temperature. Therefore, the drug-releasing profile of DOX-loaded rGO@msilica nanocarrier was also investigated under the laser irradiation in different pH solutions. We first tested irradiation-triggered DOX releasing profile of DOX-loaded rGO@msilica nanocarrier in pH 7.4 solution. As shown in Figure 5A, 9.1 % of the loaded DOX was released in the first 6 hours with NIR irradiation. Compared to the one without NIR irradiation, an additional of 4.2% drug release was obtained. When the acidic pH of 5.0 was utilized with the NIR irradiation to trigger the drug release, 48.3 % of DOX was released from the nanocarrier in 6 hours (Figure 5A), which was significantly higher than the single trigger of acidic pH or NIR laser irradiation. Therefore, with the highly efficient photothermal effect, rGO@msilica nanocarrier was expected not only to work as a photothermal agent to directly kill cancer cells, but also to possess higher drug release rate with the elevated temperature under the NIR irradiation.

3.5 Biocompatibility of the rGO@msilica Nanocarriers.

The biocompatibility of the nanocarrier was investigated before the application of the nanocarrier for drug delivery. Two cancer cell lines, including human lung cancer cell line (A549) and human colorectal carcinoma cell line (SW620), were selected for this study because of their widespread prevalence and high mortality. As described in the experimental section, the cells were incubated with different concentrations of rGO@msilica nanocarrier without loading DOX. After 24 hours of incubation, an MTT assay was performed to evaluate the cell viability of these two cell lines. As shown in Figure 6, the cell showed high viability of 84.7% even at the concentration of 2.5 mg/mL. There was no significant difference between different treatment groups (* $p < 0.05$), indicating the excellent biocompatibility of the rGO@msilica nanocarrier.

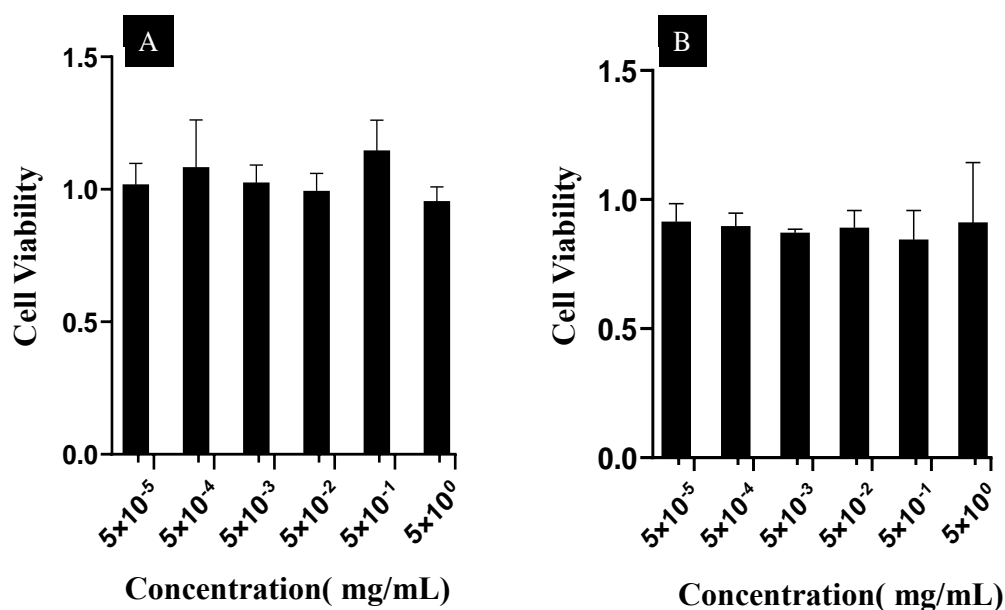


Figure 6. Cell viability of A549 cells (A) and SW620 cells (B) after the treatments with various concentrations of rGO@msilica nanocarriers for 24 h.

3.6. Chemotherapy Evaluation of the DOX-Loaded rGO@msilica Nanocarrier.

Due to the excellent biocompatibility of the rGO@msilica nanocarrier, the chemotherapy of the DOX-loaded rGO@msilica nanocarrier was investigated in vitro. A549 lung cancer cells were incubated with different concentrations of DOX-Loaded rGO@msilica (2.5×10^{-5} to 2.5 mg/mL) for 12 hours, followed by the MTT assay to evaluate the cell viability. As shown in Figure 7A, when the concentration of the DOX-Loaded rGO@msilica increased, the cell viability decreased significantly. 80.4% of the cancer cells were killed when the concentration of DOX-loaded rGO@msilica nanocarrier reached 2.5 mg/mL. The results demonstrated a dose-dependent therapeutic effect of the DOX-loaded rGO@msilica nanocarrier to the A549 cancer cells. The IC50 concentration was calculated to be 2.5×10^{-2} mg/mL at the period of 12-hour incubation. The effect of the incubation period on the A549 cell viability was also investigated at the concentration of 2.5×10^{-2} mg/mL. As shown in Figure 7B, the A549 cell viability decreased as the time collapsed and reached the plateau at 30 hours. At this moment, 82.9% of cancer cells were killed and remained the same value as the time increased to

40 hours. The result indicated that the drug release from the rGO@msilica nanocarrier was a slow and effective process.

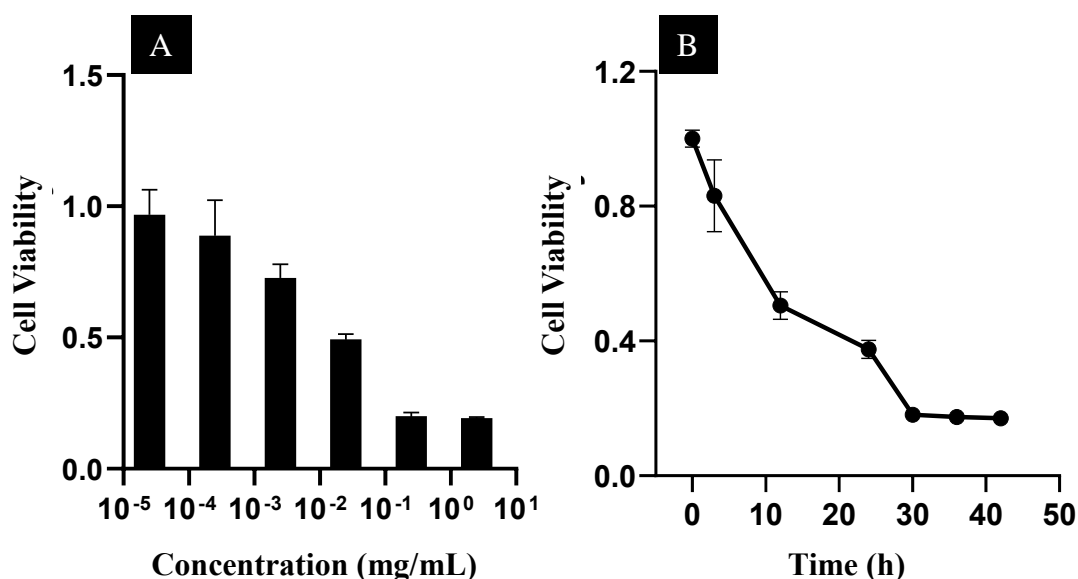


Figure 7. (A) The cell viability of the A549 cells with different concentrations of DOX-loaded rGO@msilica nanocarrier. The concentration of DOX loaded rGO@msilica was from 2.5×10^{-5} mg/mL to 2.5 mg/mL. The incubation time was 12 hours. (B) The time effect of the DOX-loaded rGO@msilica nanocarrier on the cell viability of the A549 cells. The concentration of the DOX-loaded rGO@msilica nanocarrier was 2.5×10^{-2} mg/mL.

3.7. Cellular Uptake and Drug Release in Cells.

To further confirm the drug release behavior of the nanocarrier in cancer cells, confocal fluorescence images of A549 cells were taken under different incubation time periods with the DOX-loaded rGO@msilica nanocarrier (Figure 8A). The cells were also stained with DAPI²³ as it could bind with DNA to show strong blue fluorescence. When the DOX-loaded rGO@msilica nanocarrier (2.5×10^{-2} mg/mL) was incubated with cells for only 10 min, the fluorescence signal from DOX was mainly localized around the nucleus (Figure 8A), which was because the un-released DOX from the nanocarrier couldn't enter the nucleus with the relative large size of the nanocarrier. However, when the incubation time increased to 6 hours, most of the DOX fluorescence was co-localized with DAPI in the nucleus (Figure 8A), indicating the effective drug release from the nanocarrier. When the incubation time increased to 24 hours, the red

fluorescence spread in both nucleus and cytoplasm due to the drug release from the nanocarrier. The intensities of these fluorescence signals were quantitatively measured (Figure 8B). The red fluorescence from DOX was gradually enhanced in cells with time, indicating the gradually drug release in cells.

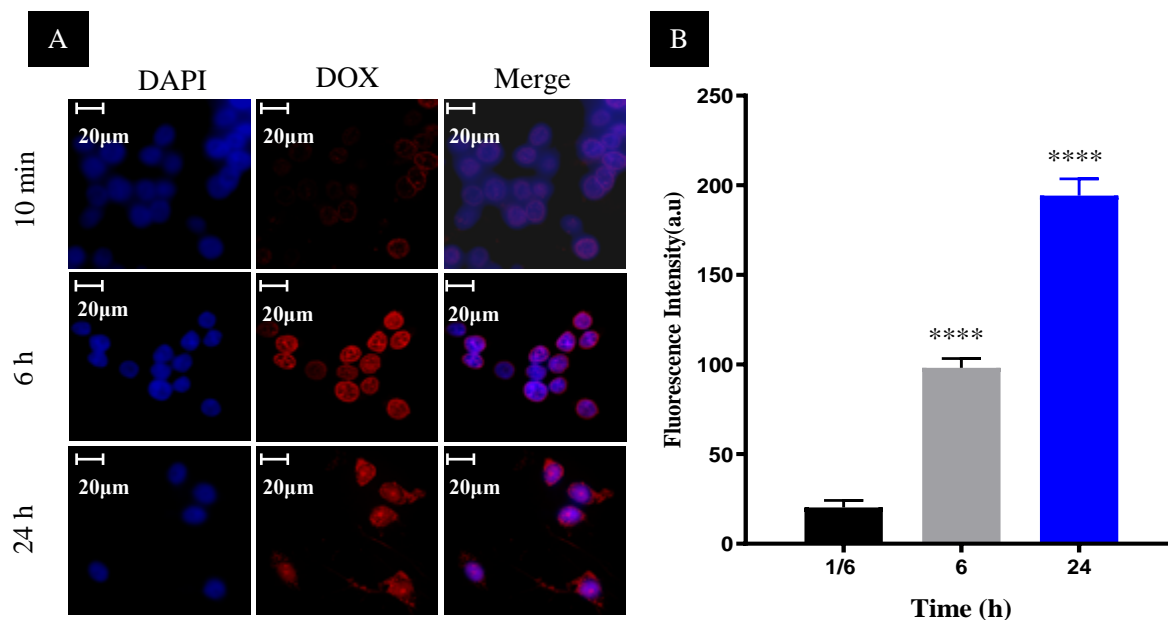


Figure 8. (A) Confocal fluorescence images of A549 cells incubated with DOX-loaded rGQ@msilica nanocarrier at different time periods, including 10 min, 6 h, and 24 h. The nucleus was counterstained with DAPI (blue). The red fluorescence was from DOX. (B) The fluorescence intensity of DOX in cells was quantified by Image J software. (**** $p < 0.0001$)

3.8. Synergistic Chemo-Photothermal Therapy of Cancer Cells.

As previously discussed, rGO was well recognized as an efficient photothermal agent for cancer treatment.³⁶ Combined with the chemotherapy of the loaded DOX, the synergistic chemo-photothermal therapeutic effect of the DOX-loaded rGO@msilica nanocarrier was investigated under an NIR irradiation (808 nm, 0.3 W/cm²). As shown in Figure 10, SW620 cells (Figure 9A) and A549 cells (Figure 9B) were incubated with 2.5×10^{-2} mg/mL DOX-loaded rGO@msilica nanocarrier for 6 hours and 24 hours, followed by the NIR laser irradiation (808 nm, 0.3 W/cm²) for 15 min. Then, the cells were cultured in medium for additional 12 h, followed by the MTT assay to assess the cell viabilities. The results showed that pure rGO@msilica

nanocarrier has no significant cytotoxic activity to both cell lines compared with the control group, indicating the great biocompatibility of the rGO@msilica nanocarrier. Taking SW620 cells as an example, the photothermal therapy effect caused by the combination of the rGO@msilica nanocarrier and NIR laser irradiation showed a moderate therapeutic effect, resulting in the reduction of cell viability to 60% and 66 % at 6 hours and 24 hours, respectively. Moreover, the cell viability of SW620 cells treated with DOX-loaded rGO@msilica nanocarrier without NIR irradiation caused severe cell death, resulting in the cell viabilities of 51% and 19% at 6 hours and 24 hours, respectively. More importantly, the combination of the chemo-photothermal therapy by treating cells with DOX-loaded rGO@msilica nanocarrier and NIR irradiation killed more cells. At 6 hours and 24 hours, the cell viabilities decreased to 31% and 9%, respectively. Similarly, the synergistic therapeutic efficiency was demonstrated in the treatment of A549 cells (Figure 9B). Thus, DOX-loaded rGO@msilica nanocarrier composed of chemo-photothermal therapeutic capacities demonstrates better

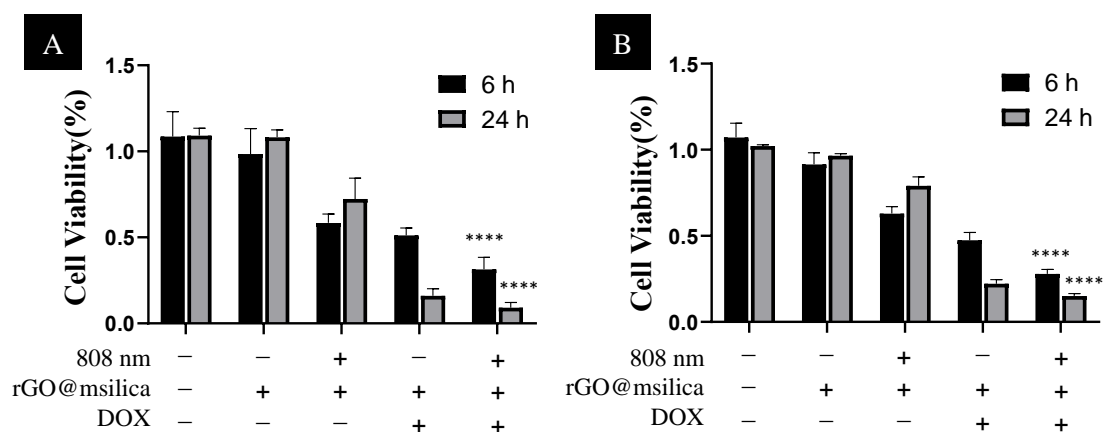


Figure 9. The cell viabilities of SW620 (A) and A549 (B) cells after different treatments. “-” stands for no treatment. “+” stands for the treatment. The cells were incubated with nanocarriers for 6 h and 24 h, respectively, followed by the 808 nm laser irradiation of 15 min. (**** p < 0.0001)

4. Conclusions

In summary, we have designed and constructed a bifunctional DOX-loaded rGO@msilica nanocarrier with photothermal effect and pH-responsive drug release properties. The large surface area and pore size of the rGO@msilica nanocarrier possessed effectively drug loading efficiency and pH-responsive drug releasing behavior. Moreover, in the acidic environment with NIR irradiation, the drug releasing efficiency was significantly enhanced, causing significant cancer cell death. The synergetic effect of chemotherapy and photothermal therapy under NIR irradiation demonstrated the enhanced cancer cell killing efficacy in vitro. The developed rGO@msilica nanocarriers might have great potential for fighting cancer by the combined therapeutic strategies.

CHAPTER II

GRAPHENE OXIDE-BASED FLUORESCENCE ASSAY FOR SENSITIVE DETECTION OF DNA EXONUCLEASE ENZYMATIC ACTIVITY

1. Introduction

In enzymatic studies, exonuclease families have been involved in numerous aspects of cellular metabolism and maintenance in physiological processes, such as assisting DNA proofreading and maintaining genome stability.⁵⁹ 3'-5' exonuclease III (Exo III), isolated from *E. coli* in 1964, was a key bifunctional enzyme and essential to genome stability. The function of Exo III was to remove mononucleotides from 3'-hydroxyl termini of double-stranded DNA.⁶⁰ In the process of DNA replication, 3'-5' exonuclease possesses indispensable functions, such as repairing DNA breaks,⁶¹ assuring the accuracy of replication process and stabilizing the mutation rates in cells.⁶²⁻⁶⁵ The defects of 3'-5' exonuclease enzymes render cells processing wrong transcription, translation and eventually lacking protection from cancer development, in particular under long periods of stress.^{59, 66} Therefore, it is highly desired to develop well-performed analytical methods for the precise measurement of the 3'-5' exonuclease activity.⁶⁷⁻⁶⁸

Traditional methods for the detection of 3'-5' exonuclease enzymatic activity are based on gel electrophoresis, which requires radioactive-labelled DNA probes. However, the liabilities of these methods include time-consuming measurements, tedious steps and safety concerns because of radiographic exposure process.⁶⁹⁻⁷¹ In order to overcome these limitations, a number of fluorescent biosensing systems have been developed due to their simple and cost-effective properties.⁷²⁻⁷⁴ For example, Yang *et al.* designed a label-free, "turn-on" fluorescence assay for the rapid detection of exonuclease III activity based on the Tb³⁺-promoted G-quadruplex.⁷⁵ Zhang's group developed a triple-color fluorescent probe by lab-on-a-DNA-molecule for simultaneous

detection of multiple exonucleases.⁷⁶ Recently, we constructed a dual molecular hairpin system to distinguish various exonucleases rapidly.⁷⁷ Comparing these approaches with traditional methods, both the cost and complexity have been significantly reduced. However, the relatively high background signals and limit of detection constrain the detection of exonuclease activity at low concentration in complex matrix.

Graphene oxide (GO), as a universal fluorescence quencher, is a two-dimensional oxidized version of graphite.⁷⁸⁻⁷⁹ It comprises of carbon-carbon sp^2 domains together with multiple functional groups, such as carboxylic group, hydroxyl and epoxide groups.⁸⁰ One of the most interesting roles of GO in sensing systems was to serve as a universal fluorescence quencher through fluorescence resonance energy transfer (FRET).⁸¹ For example, fluorophore-labeled single strand DNA (ssDNA) molecules can be easily attached onto the surface of GO by the strong π - π stacking interactions between GO and exposed nucleobases, inducing significant fluorescence quenching.⁸²⁻⁸⁷ In contrast, the binding force would become much weaker once the double-stranded DNA (dsDNA) was formed, which releases the fluorophore from the GO and restores the fluorescence. The difference of the binding forces between GO to ssDNA and dsDNA has been widely used to construct assays for detecting DNA, proteins, enzymes, metal ions, etc.⁸⁸ For instance, Min *et al.*⁷² used this strategy to construct a fluorescent sensor for detecting the activity of Exo III, in which the fluorescence was significantly decreased in the presence of Exo III. However, the signal “turn-off” strategy might have high background noise to affect the sensitivity, which hampered its wide applications.

In this work, we have developed a “turn-on” fluorescence assay for monitoring of 3' -5' exonuclease enzymatic activity based on the interaction between GO and a DNA hairpin probe (HP). The developed assay showed an ultra-low limit of detection

of 0.001 U/mL in buffer in 0.004 U/mL in 25-times diluted serum sample. This highly sensitive and selective assay provided a promising new technology for monitoring of 3'-5' exonuclease enzymatic activity in clinical diagnosis.

2. Experimental Section

2.1. Chemicals and Instruments.

Graphene oxide aqueous solution (5 mg/mL) was purchased from ACS Material (Pasadena, CA). The sequence of the hairpin probe (HP) was

5'-TTTTTTTTTTGGATCCCGCTTCTTTTTTTTTTTGAAGCGGGATCC-

FAM-3', which was synthesized by Integrated DNA Technologies (IDT). Exonuclease III (Exo III), T4 polynucleotide kinase (T4 PNK), alkaline phosphatase, calf Intestinal (CIP), uracil-DNA glycosylase (UDG), exonuclease I (Exo I), RecJf, lambda exonuclease (Lambda Exo) and 10x NEBuffer 2 were obtained from New England Biolabs (NEB). PBS tablets, ethylenediaminetetraacetic acid and fetal bovine serum were purchased from Sigma Aldrich Inc. The deionized (DI) water (18.2 MΩ • cm) was produced from a Millipore water purification system. Fluorescence measurements were performed on a RF-6000 fluorophotometer (SHIMADZU, Kyoto, Japan). The excitation wavelength was set to be 480 nm and the emission was recorded from 500 nm to 650 nm. The fluorescence intensity at 517 nm was selected to evaluate the performance of Exo III detection. Both the widths of excitation and emission slits were 10.0 nm. All the experiments were carried out at 37 °C. The morphology and element analysis of GO were carried out on a Hitachi SU8010 field emission Scanning Electron Microscope (SEM) equipped with an Energy-dispersive X-ray spectrometer.

2.2. Feasibility of the sensor for Exo III detection

A 100 μL aliquot of 1X NEBuffer 2 containing 100 nM hairpin probe (HP) was mixed with 1 μL of 50.0 U/mL Exo III and then incubated at 37 °C for 10 min.

Then, 1 μL of 2.0 mg/mL GO solution was added and incubated at 37 °C for another 10 min. The fluorescence spectra of the solution were recorded with the excitation wavelength of 480 nm.

2.3. Detection of Exo III activity

Briefly, a 100 μL aliquot of 1X NEBuffer 2 containing 100 nM hairpin probe (HP) was mixed with 1 μL of various concentrations of Exo III and then incubated at 37 °C for 10 min. Then, 1 μL of 2.0 mg/ mL GO was added to the above solution and incubated at 37 °C for another 10 min. The fluorescence intensity of the final solution was detected with the excitation wavelength of 480 nm.

2.4. Evaluation of the selectivity

The selectivity of the assays was evaluated by testing the fluorescence signal of the sensing system to other DNA digesting enzymes. Typically, a whole volume of 100 μL solution including HP (100 nM) and 10.0 U/mL of one of the following enzymes, including Exo III, Exo I, Lambda Exo, RecJf, T4 PNK, CIP and UDG, were incubated in a 37 °C water bath for 10 min. Then, 1 μL of 2.0 mg/ mL GO was mixed with the above solution and incubated at 37 °C for additional 10 min. The fluorescence intensity was measured with the excitation wavelength of 480 nm.

2.5. Exonuclease inhibition assay

To perform the inhibition assay on the activity of Exo III, a 100 μL aliquot of solution containing 10.0 U/mL Exo III, 100 nM HP and various concentrations of EDTA were incubated at 37 °C for 10 min, followed by addition of 1 μL of 2.0 mg/ mL GO and incubated for another 10 min in a 37 °C water bath. The fluorescence intensity of the final solution was recorded with the excitation wavelength of 480 nm.

2.6. Performance in 25-times diluted serum

A 0.4 mL volume of fetal bovine serum sample was added into 0.6 mL of

acetonitrile. The mixture was stirred at a vigorous vortex for 5.0 min, and then centrifuged at 10,000 rpm for 10 min. The collected supernatant was diluted by 5 times with 1X NEBuffer 2. To test the Exo III activity, a 100 μ L aliquot of above 5-times diluted FBS sample was first mixed with 100 μ L of 200 nM HP, followed by adding different concentrations of Exo III (0, 0.01, 0.05, 0.10, 0.15, 0.5, 1.0, 5.0 U/mL). The above solution was then incubated in a 37 °C water bath for 10 min. Finally, a 2 μ L of 2.0 mg/mL GO was added into the previous solution and incubated for another 10 min in a 37 °C water bath. The fluorescence spectra were recorded with the excitation wavelength of 480 nm.

2.7. Kinetic Analysis

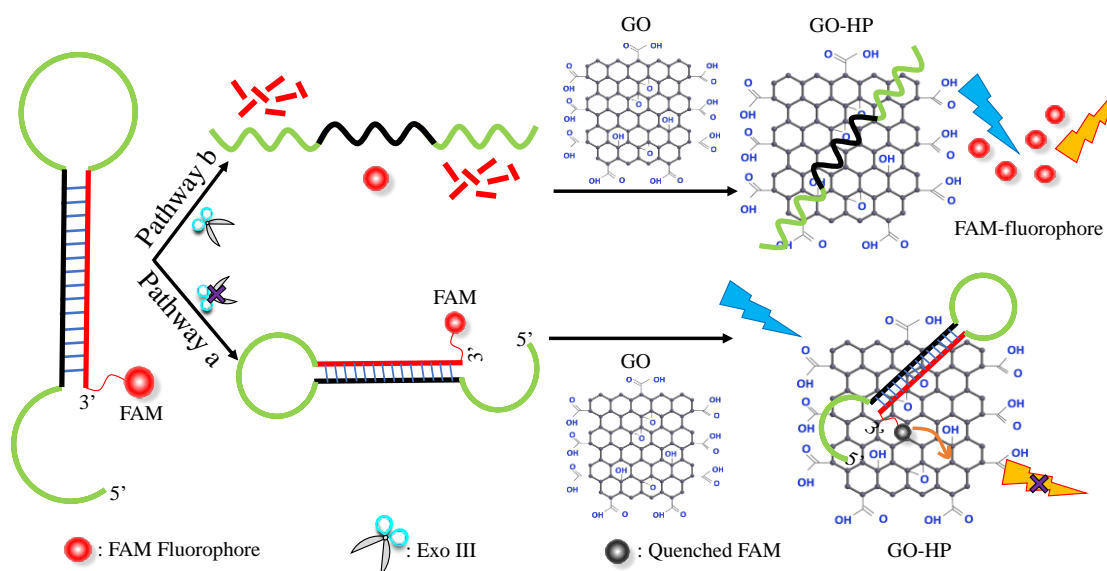
In general, a 100 μ L aliquot of 1X NEBuffer 2 containing 100 nM hairpin probe (HP) was mixed with 1 μ L of 2.0 mg/ mL GO. The fluorescence at 517 nm with excitation at 480 nm was recorded with time. After the fluorescence was stabilized, 1 μ L of various concentrations of Exo III was added and incubated at 37 °C. The fluorescence intensity was monitored *vs* time for another 5 min.

3. Results and Discussion

3.1. Design of the Exo III assay

As shown in Scheme 2, a hairpin probe (HP) modified with a fluorophore (FAM) at the blunt 3'-termini was used for this sensor. The intact FAM-tipped HP without treatment of Exo III would be strongly absorbed onto GO due to the strong π - π stacking interaction between them, leading to absolute fluorescence quench through the efficient FRET (Pathway a). However, the presence of Exo III digested phosphor-ester bonds and removed mononucleotides starting from the blunt 3'-termini of HP to the whole double strand domain, generating a long unlabeled ssDNA and a FAM-labeled mononucleotide. With the addition of GO, the ssDNA was absorbed onto GO

spontaneously but the affinity between the FAM-labeled mononucleotide and GO was much weaker than that with ssDNA.⁸⁹ Because of the dissociation between the GO and FAM-labeled mononucleotides (Pathway b), fluorescence was significantly restored compared with the sample without Exo III treatment.



Scheme 2 Schematic illustration of the Exo III detection based on the GO and FAM-labelled HP.

3.2. Characterization of GO.

To In this sensor, we utilized GO as a quencher for its excellent quenching efficiency to various fluorophores and its different affinities to ssDNA and mononucleotide.⁷⁸ To characterize the morphology of the GO and elemental analysis, a SEM image of GO and corresponding Energy-dispersive X-ray spectroscopy mapping were obtained (Figure 10). The average size of the GO sheets was around 800 nm, which provided large surface area for ssDNA (loop domain) to attach to (Figure 10A). The EDS analysis showed that GO mostly contained elements of carbon and oxygen (Figure 10B-C). Moreover, the absorption spectrum of GO showed the typical peak at 230 nm of GO and broad absorption from UV to visible range (Figure 10E), making GO an ideal fluorescent quencher for a variety of fluorophores.

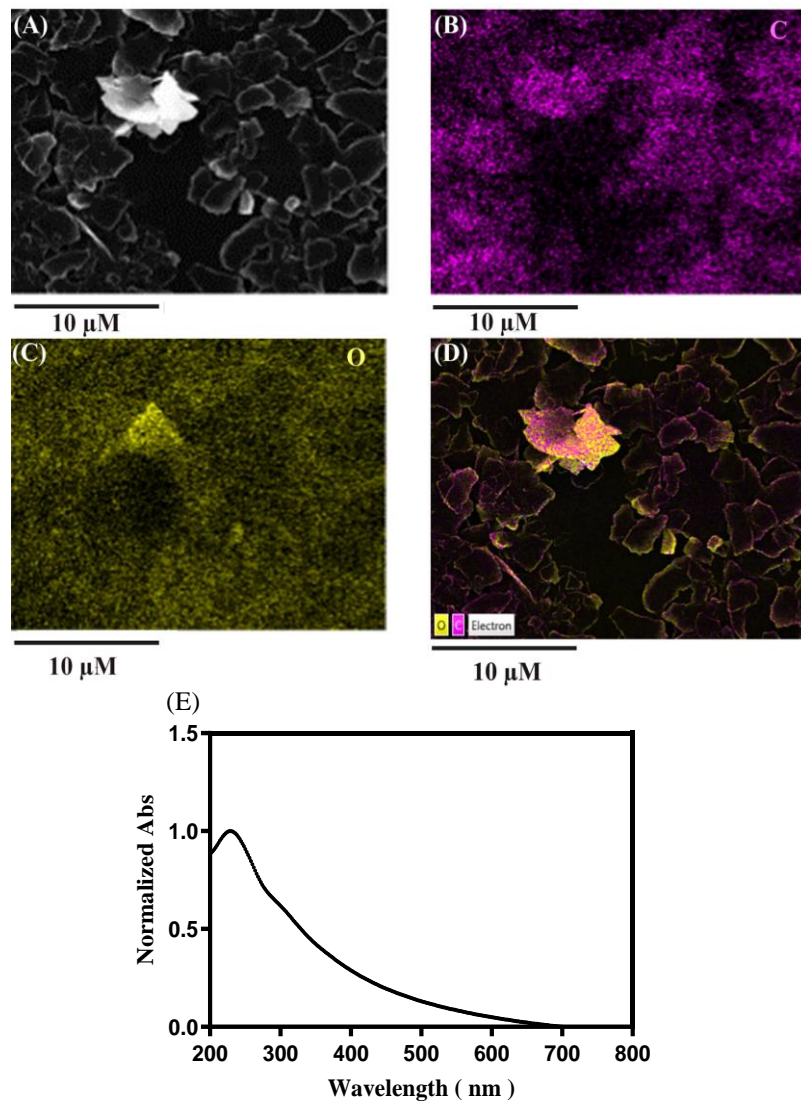


Figure 10. (A) The SEM image and corresponding elemental maps of GO in (B) carbon (pink), (C) oxygen (yellow). (D) overlayed mapping of GO (scale bar = 10 μm). (E) UV-vis absorption spectrum of GO with a typical absorption maximum at 230 nm.

3.3. Feasibility investigation.

To demonstrate the feasibility of the developed sensor, the fluorescence emission spectra of the HP under different conditions was recorded. As shown in Figure 11, pure HP (100 nM) emitted fluorescence at 517 nm with the excitation of 480 nm (curve a). When GO was added with the HP, the fluorescence intensity was decreased by over 95% (curve b) quickly, indicating the outstanding fluorescence quenching ability of GO. In contrast, when HP was treated with Exo III before the addition of GO, a relative high fluorescence intensity was collected (curve c), which was attributed to the removal of the FAM-labelled blunt 3'-terminal part of HP by Exo III, increasing the distance and weakening the FRET between GO and FAM. The variation of three spectra confirmed that this sensing system could be applied for the detection of Exo III activity.

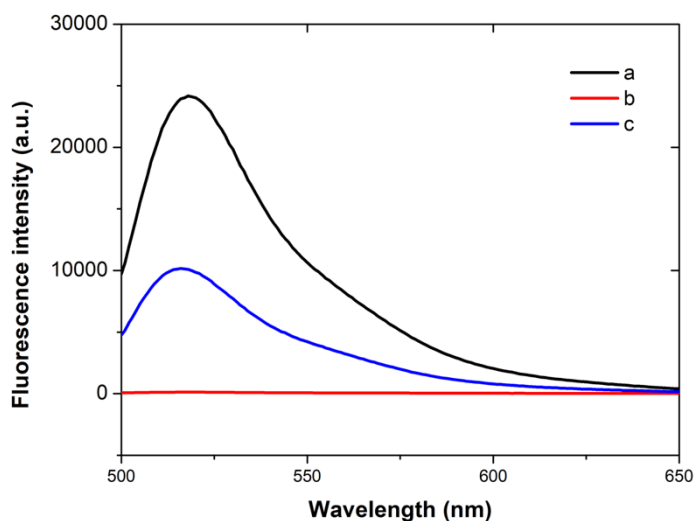


Figure 11. Fluorescence spectra of HP (100 nM) under different conditions. (a) 100 nM HP, (b) 100 nM HP + 20 $\mu\text{g/mL}$ GO, (c) 100 nM HP + 0.5 U/ mL Exo III + 20 $\mu\text{g/mL}$ GO. $\lambda_{\text{ex}} = 480$ nm, All the reagents were incubated in 1X NEBuffer 2. $\lambda_{\text{em}} = 500$ nm - 650 nm.

3.4. Optimization of experimental conditions.

To determine the optimal conditions for Exo III activity analysis, the impacts of the concentration of GO, the concentration of HP, and the reaction time on the sensing performance were investigated. As shown in Figure 12A, a time-based fluorescence collection was performed with a whole volume of 100 μL solution

(containing 20 $\mu\text{g}/\text{mL}$ GO and 50 nM HP in 1X NEBuffer2) at 37 $^{\circ}\text{C}$ for 1200 s. After the addition of GO, the fluorescence intensity decreased substantially in the first 100 s, and then reached the plateau after about 200 s. Therefore, the reaction time in the quenching process was set to 10 min.

Additionally, the concentration of GO needs to be considered to reach a low background. The fluorescence intensity of HP with and without different concentrations of GO were measured to assess the optimal concentration of GO. As shown in Figure 12B, F_0 refers to the fluorescence intensity of 100 nM HP without GO, and F refers to the fluorescence intensity of 100 nM HP after the addition of various concentrations of GO. The ratio of F/F_0 was decreased as the concentration of GO elevated, indicating the concentration-dependent quenching ability of GO. The ratio reached to a plateau after the concentration enhanced to 20 $\mu\text{g}/\text{mL}$. Therefore, in the following experiments, we used 20 $\mu\text{g}/\text{mL}$ as the optimal concentration of GO to perform the subsequent detection.

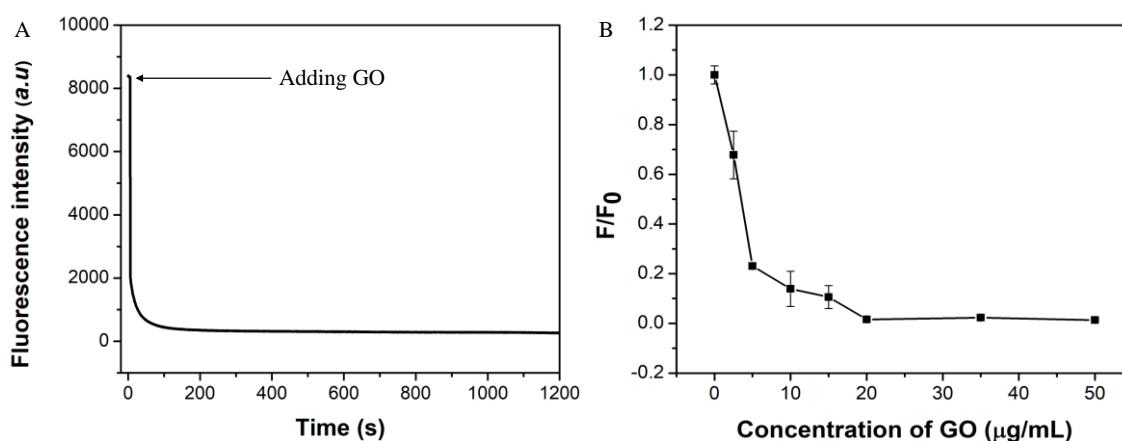


Figure 12. (A) A time-based fluorescence intensity curve was collected in 100 μL 1X NEBuffer2 solution containing 50 nM HP solution with addition of 20 $\mu\text{g}/\text{mL}$ GO at 37 $^{\circ}\text{C}$ for 1200 s. (B) Fluorescence intensity ratios of F/F_0 at different concentrations of GO. F_0 refers to the fluorescence intensity of 100 nM HP without GO, and F refers to the fluorescence intensity of 100 nM HP after the addition of various concentrations of GO. $\lambda_{\text{ex}} = 480 \text{ nm}$, $\lambda_{\text{em}} = 517 \text{ nm}$.

The concentration of HP was the third impact that needs to be optimized. A series of concentrations of HP were incubated with 50.0 U/mL Exo III, followed by mixing with 20 $\mu\text{g/mL}$ GO (Figure 13). Fluorescence intensity of the above solution was recorded and designated as F. In contrast, another series of same concentrations of HP were directly mixed with 20 $\mu\text{g/mL}$ GO only, whose fluorescence intensity was defined as F_0 . The corresponding ratios of F to F_0 reached maximum value at the concentration of 100 nM of HP, suggesting the highest sensitivity at this concentration. Consequently, we set the concentration HP to 100 nM for the following experiments.

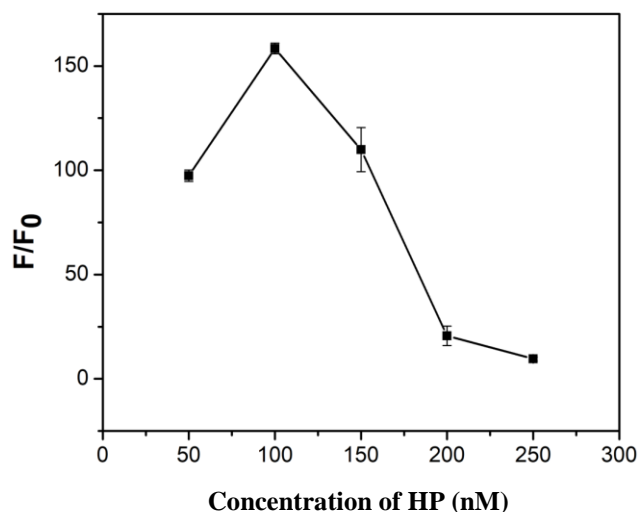


Figure 13. The effect of concentration of HP on the performance of the sensor. F referred to the fluorescence intensity of different concentrations of HP treated with 50.0 U/mL of Exo III followed by the addition of 20 $\mu\text{g/mL}$ GO. F_0 represented the fluorescence intensity of the same series of HP without treatment of Exo III in the presence of 20 $\mu\text{g/mL}$ GO. $\lambda_{\text{ex}} = 480 \text{ nm}$, $\lambda_{\text{em}} = 517 \text{ nm}$.

3.5. Exo III detection.

To investigate the sensitivity of the sensor towards Exo III, 100 nM HP solution was treated with different concentrations of Exo III for 10 min at 37 $^{\circ}\text{C}$, followed by the addition of 20 $\mu\text{g/mL}$ GO. As shown in Figure 5A, the fluorescence intensity of FAM increased when the concentration of Exo III increased from 0 U/mL to 20.0 U/mL. The results showed that the dynamic range was from 0 U/mL to 20.0 U/mL (Figure 14B), with a linear range between 0.01 U/mL to 0.5 U/mL (the inset of

Figure 14B). The calibration curve showed a regression equation of $Y=19380.6X + 71.6$ with a correlation coefficient of 0.9855. Y and X represented the fluorescence intensity and the concentration of Exo III in unit of U/mL, respectively. The limit of detection (LOD) for the detection of Exo III was calculated to be 0.001 U/mL based on the slope of the equation ($3\sigma/s$), where σ was the standard deviation of four blank fluorescence intensities and s was the slope of the calibration curve. This ultra-low LOD demonstrated that the GO-based sensor ensured an ultra-sensitive platform for the detection of Exo III activity compared with other fluorescent methods (Table 1). Moreover, the present work only needs one-terminal modification of the DNA probe compared with our previous work with a molecular beacon, and the superior quenching ability of GO significantly decreased the background, thus enhancing the sensitivity of the sensor.

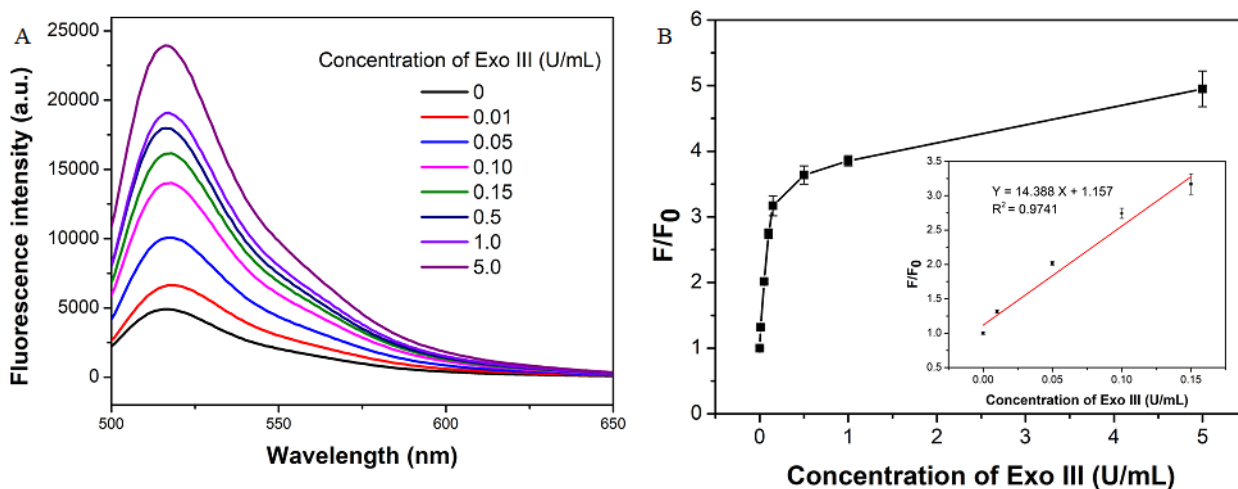


Figure 14. Fluorescence spectra of sensor incubated with different concentrations of Exo III from 0 U/mL to 20.0 U/mL. (B). The plot of the fluorescence intensity with different concentrations of Exo III. The inset graph shows the calibration curve of the sensor. Reaction conditions: 100 nM HP and 20 μ g/mL GO in 100 μ L 1X NEBuffer 2. $\lambda_{ex} = 480$ nm, $\lambda_{em} = 517$ nm.

Table 1. Comparison of the proposed sensor with other fluorescent methods.

Probes	LOD (U/mL)	Linear range	Response time	Reference
Molecular beacons	0.01	0.04 - 8 U/mL	200 s	77
Copper Nanoparticles	0.02	0.05 - 2 U/mL	91 min	91
SYBI green I	0.7	1 - 200 U/mL	110 min	92
G-quadruplex	0.8	5 - 100 U/mL	70 min	75
GO/HP	0.001	0.01-0.5 U/mL	20 min	This work

3.6. Selectivity investigation.

To validate the selectivity of this sensor, we studied the response of the sensor towards a series of DNA enzymes, including Exo I, T4 PNK, Lambda Exo, RecJf, CIP, UDG and Exo III, with a concentration of 10 U/mL. Exo I is the enzyme to cut down single strand DNA from 3' termini to 5' termini.⁹³ Lambda Exo removes 5' mononucleotides from duplex DNA.⁹⁴ RecJf digests single-stranded DNA specific from 5' termini to 3' termini.⁹⁵ T4 PNK is hunting for 5' phosphorylation of DNA/RNA for subsequent ligation.⁹⁶ CIP is catalyzing the dephosphorylation of 5' and 3' ends of DNA and RNA.⁹⁷ UDG is a recombinant enzyme that releases uracil from single strand or double strand DNA.⁹⁸ Those DNA enzymes are all very common and play essential roles in multiple biological processes.⁹⁹ Therefore, it is important to determine the selectivity of the sensor for Exo III enzymatic activity. As shown in Figure 15, with the same concentration treatment of these enzymes, only Exo III caused a significant fluorescence enhancement comparing with other enzymes. These results demonstrated

that this sensor has excellent selectivity for Exo III detection.

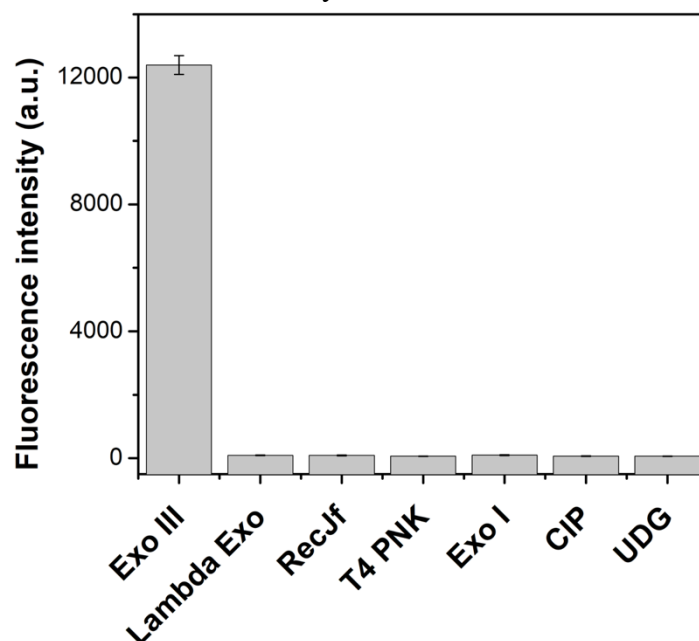


Figure 15. Selectivity of the sensor for Exo III over other enzymes. Reaction conditions: 100 nM HP and 20 $\mu\text{g}/\text{mL}$ GO in 100 μL 1X NEBuffer 2. The concentration of enzymes was 10.0 U/mL. $\lambda_{\text{ex}} = 480 \text{ nm}$, $\lambda_{\text{em}} = 517 \text{ nm}$.

3.7 Inhibition test.

We further evaluated the inhibition assay of Exo III as it is important for drug screening. EDTA, as a chelating agent, could effectively inhibit the activity of Exo III.41 As shown in Figure 16, the fluorescence intensity of the sensor decreased with the enhanced concentration of EDTA, indicating the inhibition effect of EDTA for Exo III activity. Half-maximal inhibitory concentration (IC_{50}) of EDTA was estimated to be 3.0 mM. The results demonstrated that this designed sensor could be utilized for the drug screening specifically for selecting the potential inhibitors of Exo III activity.

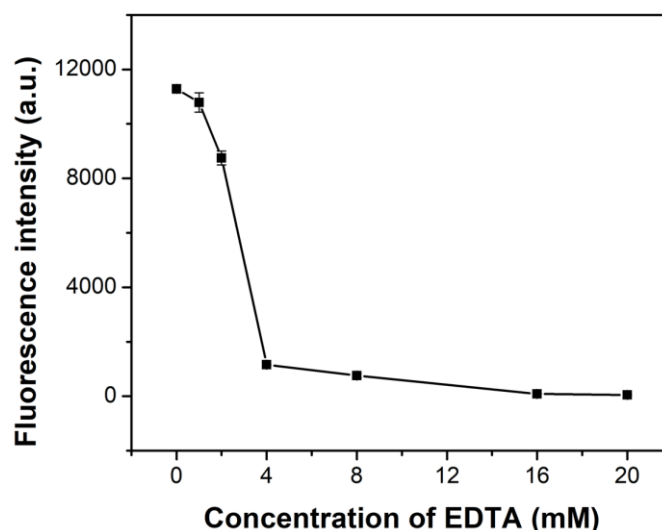


Figure 16. Effect of EDTA concentration on the Exo III activity. Reaction conditions: 100 nM HP and 20 $\mu\text{g/mL}$ GO in 100 μL 1X NEBuffer 2. The concentration of Exo III was 10.0 U/mL. $\lambda_{\text{ex}} = 480 \text{ nm}$, $\lambda_{\text{em}} = 517 \text{ nm}$.

3.8. Application in diluted serum sample.

To test the applicability of the sensor, we investigated the performance of the sensor in fetal bovine serum (FBS). The experiments were conducted at the same optimized conditions, except that the 1X NEBuffer 2 was replaced with 10-times diluted FBS with buffer. Similarly, the fluorescence intensity of FAM increased as the concentration of Exo III increased from 0 U/mL to 5.0 U/mL (Figure 17), with a linear range between 0.01 U/mL to 0.15 U/mL (the inset of Figure 17B). The calibration curve showed a regression equation of $Y = 14.388 X + 1.157$ with a correlation coefficient of 0.9741. Y and X represented the fluorescence intensity and the concentration of Exo III in the unit of U/mL, respectively. The limit of detection (LOD) for Exo III was calculated to be 0.004 U/mL in 25-times diluted FBS based on the slope of the equation ($3\sigma/s$). The results suggested that the sensor could be used in complicated samples for the detection of enzymatic activity of Exo III.

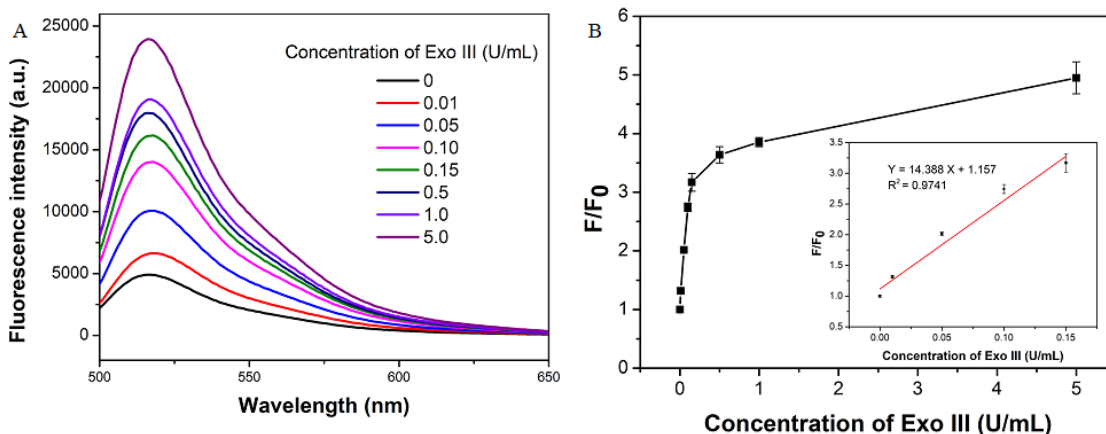


Figure 17. (A) Fluorescence spectra of the sensor upon incubation with different concentrations of Exo III in 25-times diluted FBS from 0 U/mL to 5.0 U/mL. (B) The plot of the fluorescence intensity with different concentrations of Exo III. The inset graph shows the calibration curve of the sensor. Reaction conditions: 100 nM HP and 20 μ g/mL GO in 200 μ L 25-times diluted FBS. $\lambda_{ex} = 480$ nm, $\lambda_{em} = 517$ nm.

3.9. Kinetic Analysis.

In order to obtain the kinetic analysis of the enzymatic activity, we performed the real-time fluorescence measurements using the sensor for different concentrations of Exo III. As shown in Figure 18, the fluorescence of HP was firstly totally quenched by the addition of GO, indicating the strong interaction between GO and HP, as well as the excellent quenching ability of GO towards the fluorophore. When the fluorescence intensity had stabilized, an aliquot of Exo III with different concentrations was introduced into the cuvette. The immediate fluorescence record shows a dramatically fluorescence enhancement after the addition of Exo III, indicating that the rapid enzymatic reaction in the sensor. The signal-to-background ratio reached about 10.0 when the concentration of Exo III was 1.0 U/mL. The fluorescence intensity reached a plateau after about 300 s.

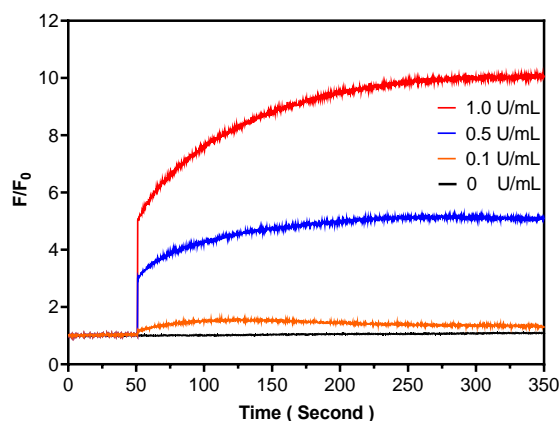


Figure 18. Real-time kinetic analysis of Exo III with different concentrations. From bottom to top: 0, 0.1, 0.5, 1.0 U/mL

4. Conclusions

In conclusion, we developed a simple and ultra-sensitive fluorescent sensor to detect the enzymatic activity of Exo III. The design was based on the different affinities of ssDNA and mononucleotide with GO and the superior quenching ability of GO to fluorophores. The sensor presented excellent selectivity to Exo III with a LOD of 0.001 U/mL in buffer, and 0.004 U/mL in 25-times diluted FBS. To the best of our knowledge, the LOD in this assay was superior in the fluorescent method for Exo III detection. The successful application in complex sample (diluted serum) of the sensor suggested that this method has the potential to be used for disease diagnosis and drug screening relating to the enzymatic activity.

CHAPTER III

ONE POT SYNTHESIS OF GRAPHENE QUANTUM DOTS USING HUMIC ACID AND ITS APPLICATION FOR COPPER(II) ION DETECTION

1. Introduction

Nanomaterials, due to their unique chemical, physical and optical properties, have proven to be pivotal tools in multiple biomedical applications.¹⁰⁰⁻¹⁰⁷ In particular, some fluorescent nanomaterials, such as quantum dots and polymer dots, have been widely used as bioimaging agents. When compared with fluorescent dyes, fluorescent nanomaterials have shown a major advantage in their photostability, which makes them an effective new probe for labeling and imaging of cells, tissues and organisms.¹⁰⁸⁻¹¹⁸ Among all the fluorescent nanomaterials, quantum dots, owing to their excellent properties, attract great attention.¹¹⁹ The bright and stable fluorescence of traditional semiconductor quantum dots (QDs), such as CdSe and CdTe, caused them to be used as alternatives to dyes in a number of applications.¹²⁰⁻¹²² They exhibit a broad absorption, along with a narrow and adjustable emission wavelength. However, the high cytotoxicity of their heavy metal components constrains their biological applications.

123-127

Graphene quantum dots (GQDs), a new emerging class of quantum dots, have attracted great attention as a promising fluorescent probe due to their unique characterizations including good water solubility, excellent photoluminescence, low toxicity, biocompatibility and high resistance to photodegradation and photobleaching.¹²⁸⁻¹³⁰ In general, GQDs are synthesized from carbon-based materials. Basically, there are two main strategies: top-down and bottom-up methods. The top-down methods include acidic exfoliation, electrochemical oxidation and hydrothermal synthesis, which break large-sized materials to small-sized GQDs. Some physical methods like sonication will accelerate the formation of GQDs. The top-down methods

bring oxygen-containing functional groups to the edges of GQDs, promoting the solubility and simplifying modification for specific purposes.¹²⁷ However, the purification procedure is time-consuming because of the highly concentrated salt in the solution. In contrast, bottom-up methods utilize small carbon-based precursors to form graphene quantum dots.¹²⁸ These approaches offer possibilities of doping multiple heteroatoms on graphene quantum dots to enrich their intrinsic properties for further applications. Unfortunately, the synthesis process always suffers from low utilization of starting materials, low yield of production and aggregation.

There are abundant raw materials to produce GQDs; the starting materials of top-down methods could be summarized as large graphene-based materials, such as graphite, graphene sheets, carbon nanotubes and fibers.¹²⁹ However, these materials are relatively expensive, which leads to a higher cost for scaled-up production. The bottom-up methods use low molecular weight carbon-based precursors.¹³⁰ Up to now, only a few low molecular weight compounds including citric acid, glucose and amino acids have been used for fabricating graphene quantum dots.¹³¹⁻¹³³ Recently, humic acid, a higher molecular weight organic compound, has been extracted from a broad range of raw materials, such as peat, soils, black coals, dystrophic lake, sea sediments and other natural materials.¹³⁴ In general, humic acid could be considered as a byproduct of biological or chemical decompositions of plant and animal residues. Thus, there is no absolute static structure for humic acid due to the diversity of humification pathways. It has been proposed that most humic acids have large conjugated double bonding area and aromatic ring structures as the main matrix, together with multiple chemically reactive functional groups such as carboxyl, aldehydes, ketones, phenols, alcoholic hydroxyls and quinones, which provide the possibilities of chelating interactions to some specific ions. Comparing with graphene-based starting materials, humic acid

contains similar highly conjugated sp^2 carbon hybridization domains, aromatic and benzene ring structures. Therefore, humic acid would be qualified to serve as a new carbon source to synthesize graphene quantum dots.¹³⁵ In the last few decades, the technology to extract humic acid from industrial waste and straw has provided sufficient supplies for the production of GQDs.¹³⁶

In this chapter, we have successfully fabricated highly fluorescent GQDs using humic acid. The preparation was conducted by hydrothermal treatment of humic acid in an autoclave at 200 °C for 12 h. The results of FTIR and XPS exhibited plentiful functional groups on the GQDs. Fluorescence and UV-Vis spectroscopy analysis showed a high yield of ca. 20% of GQDs. Compared with other methods to produce GQDs, using humic acid as a precursor would reduce the cost for scaled-up production to a great extent due to the existence of abundant humic acid in the environment. Furthermore, the application of the GQDs was demonstrated by its sensitive fluorescence response to Cu^{2+} , which was based on chelation-induced aggregation. The method showed a limit of detection of 0.44 μM Cu(II) in buffer and a linear range from 0 μM to 40 μM Cu(II).

2. Experimental Section

2.1. Chemical and materials.

Humic acid was obtained from Advanced Material Characterization Laboratory of Institute for Energy Studies. Ammonium hydroxide (NH_4OH , 28.0% – 30.0%), (4-(2-hydroxyethyl)-1-piperazineethanesulfonic acid) HEPES and sodium hydroxide were obtained from Sigma-Aldrich. Sterile syringe filters (0.45 μm cellulose acetate) were provided by ThermoFisher Scientific. High purity liquid argon and ultra-high purity helium gas obtained from Airgas were used in the ICP-MS measurements.

The 100 ppm Cu, Sc, and Rh stock solutions provided from Inorganic Ventures were used during the ICP-MS measurements. All chemicals were analytical reagent grade unless specified. All buffer solutions were prepared using ultrapure water (18 M Ω ·cm) from a Millipore Milli-Q water purification system. Copper(II) sulfate was purchased from Sigma-Aldrich.

2.2. Synthesis of the GQDs.

The GQDs was produced by a simple hydrothermal method. Briefly, 10.0 mg of humic acid was dispersed in 10.0 mL 0.01 M NaOH aqueous solution and then the pH was optimized to about 10. The black solution was sonicated and transferred into a 25.0 mL Teflon-lined stainless-steel autoclave. The reaction temperature was heated up to 200 °C for 12 h in an oven. After the autoclave was cooled down to room temperature, and the solution had turned brown. Finally, the solution was centrifuged at 10,000 rpm for 20 min to remove the large particles, and the supernatant was further dialyzed in a dialysis bag (molecular weight cutoff = 10,000) for 48 h to remove small molecules.

2.3. Characterization of the GQDs.

A JEOL JEM-2100 high-resolution transmission electron microscope (HRTEM) (JEOL Ltd., Tokyo, Japan) was used to take images of the GQDs with the voltage condition at 200 kV. The size distribution of the GQDs was recorded from Zetasizer Nano ZS (Marlwen, Worcestershire, UK). A PerkinElmer Lambda 1050 UV/VIS/NIR spectrometer (PerkinElmer, Santa Clara, CA, USA) was used to obtain the absorption spectra of the GQDs. Fluorescence measurements were performed on a RF-6000 fluorophotometer (SHIMADZU, Kyoto, Japan). The excitation wavelength was 360 nm and the emission was recorded from 380 nm to 700 nm. The fluorescence intensity at 470 nm was selected to evaluate the performance of Cu²⁺ detection. Both the widths of excitation and emission slits were 10.0 nm. All the experiments were

carried out at 25 °C. A FT-IR Spectrum ATR iD5 spectrometer (ThermoFisher Scientific, Waltham, UK) was used to collect the Fourier transform infrared (FTIR) spectra of GQDs. The X-ray photoelectron spectroscopy (XPS) measurements was performed on a PHI-5400 X-ray photoelectron spectrometer (ULVAC-PHI, Japan) with 10^{-10} Torr base pressure. The Al K α (1486.6 eV) X-ray radiation was used as the X-ray source, powered at 300 W for excitation. An X-ray diffraction spectrum was recorded on a Smartlab-3KW X-ray Diffractometer (Rigaku, Tokyo, Japan). Teflon Lined Hydrothermal Synthesis Autoclave Reactor (APT, RI, USA). PTFE Lined Vessel (25 mL) was used to synthesize GQDs. VWR Symphony Vacuum Oven (VWR, PA, USA). was utilized to increase the temperature to 200 °C. An iCAP Qc ICP-MS (Thermo Scientific, Bremen, Germany) combined with a 4-channel 12-roller peristaltic pump and a Teledyne CETAC ASX560 autosampler (Omaha, NE) was used to monitor the Cu concentrations in Red Revier water samples. The THERMO-4AREV (Thermo Scientific) standard was run daily to optimize the ICP-MS with maximum ^{59}Co , ^{238}U and minimum $^{140}\text{Ce}/^{140}\text{Ce}$ oxide signal in the kinetic energy discrimination. The ICP-MS measurements of Cu concentraions were collected using the QtegraTM software (version 2.8.2944.202). The isotopes ^{45}Sc and ^{103}Rh were used as internal standard in the ICP-MS measurements.

2.4. Effect of pH and photostability

1.0 mL of 1.0 mg/mL GQDs solution was incubated in different pH buffer, ranging from 1 to 12 for 1 hour. Then, the fluorescence intensity of the GQDs solution at different pH was recorded. In order to investigate the photostability of GQDs, a time-based fluorescence collection was performed with 1.0 mL 1.0 mg/mL GQDs solution for 1800 s. FITC was used as a control group.

2.5. Quantum yield measurement

Quinine sulfate in 0.1 M H₂SO₄ (QY = 0.54 at 360 nm) was chosen as a standard for quantum yield measurement. The quantum yield of the GQDs was calculated according to the following formula:

$$\Phi_x = \Phi_{st} \left(\frac{Grad_x}{Grad_{st}} \right) \left(\frac{\eta_x^2}{\eta_{st}^2} \right)$$

Φ_x is the quantum yield. Grad is the gradient from the plot of integrated fluorescence intensity vs absorbance and η is the refractive index of the solvent (1.33 for water). The subscript "st" stands for the reference standard of known quantum yield and "x" for the sample. In order to minimize reabsorption effects, absorbances in the 10 mm fluorescence cuvette were kept under 0.1 at the excitation wavelength (360 nm).

2.6. Copper(II) ion induced aggregation analysis

In order to demonstrate the strategy for this Cu²⁺ detection, as a stronger chelator, same molar amount (40 μ M) of EDTA as Cu²⁺ was together added into the 0.4 mg/mL GQDs solution. In two parallel experiments, one only contained 0.4 mg/mL GQDs, the other contained an aliquot of 40 μ M of Cu²⁺ mixed with 0.4 mg/mL GQDs. All of the fluorescence intensity was measured with an excitation wavelength of 360 nm. The fluorescence signal at emission wavelength of 470 nm was recorded.

2.7. Copper(II) ion detection procedure.

In order to investigate the quenching ability of Cu²⁺ on GQDs, we incubated the 1.0 mL of 0.4 mg/mL GQDs with different concentrations of Cu²⁺ for 12 h. Then, the fluorescence intensity at 470 nm with excitation of 360 nm was recorded for each concentration. The concentration of Cu²⁺ ranged from 0 to 300 μ M.

2.8. Selectivity investigation of GQDs.

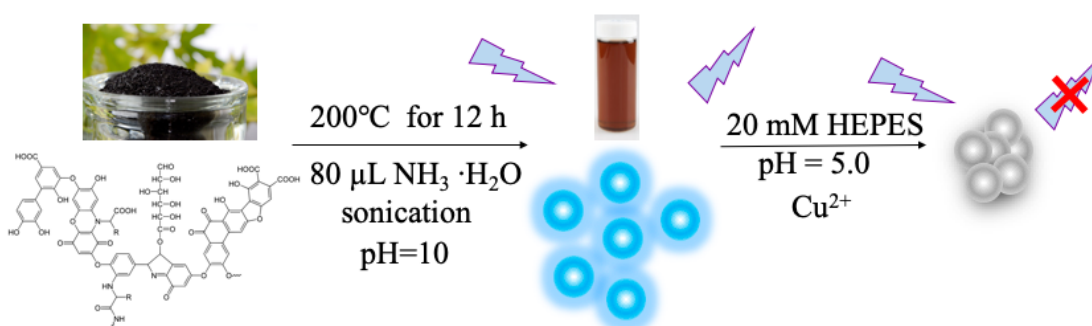
In order to investigate the selectivity of GQDs on different metal ions, 1.0 mL of 1.0 mg/mL GQDs solution was added with different metal ions, including, Ni²⁺, Ca²⁺,

Co^{2+} , Cd^{2+} , Mg^{2+} , Cu^{2+} , Zn^{2+} , Fe^{3+} , Mn^{2+} , Na^+ , K^+ , Ag^+ , and Pb^{2+} . The concentrations of the metal ions were fixed at 20 μM . All the fluorescence intensity was measured with the excitation wavelength of 360 nm. The fluorescence signal at emission wavelength of 470 nm was recorded.

3. Results and Discussion

3.1. Formation and design of the highly fluorescent GQDs

A simple bottom-up method was developed to fabricate GQDs from humic acid by a one pot hydrothermal reaction. The formation of GQDs is illustrated in Scheme 3. Firstly, in order to enhance the solubility of humic acid, the pH of distilled water was adjusted to 10 by ammonium hydroxide; during this process, humic acid was well dispersed and formed into a dark black solution. Afterwards, an aliquot of 10.0 mL of the above solution was transferred into autoclave and put into an oven whose temperature was set to be 200 °C for 12 h. After purification by dialysis, the highly fluorescent GQDs were obtained. Interestingly, the fluorescence intensity of this specific GQDs showed strong response to Cu^{2+} (Scheme 3). In the presence of Cu^{2+} , the carboxylic groups on the GQDs might chelate with Cu^{2+} and lead to a significant aggregation of GQDs, which cause a noticeable decrease of the fluorescence intensity. In order to prove this theory, same concentration of EDTA and Cu^{2+} was added together into graphene quantum dots, it was found that the fluorescence intensity would recover with the help of EDTA (Figure 19).



Scheme 3. Schematic illustration of the formation of GQDs and its application for Cu^{2+} detection.

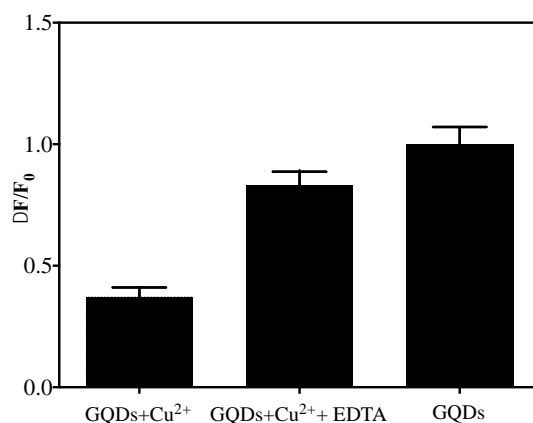


Figure 19. The Cu^{2+} induced aggregation could be reversed by introducing EDTA into solution. Reaction condition: pH 7.0, 20 mM HEPES, 0.4 mg/mL GQDs, 40 μM Cu^{2+} , 40 μM EDTA, $\lambda_{\text{ex}} = 360$ nm, $\lambda_{\text{em}} = 470$ nm.

3.2. Characterization of graphene quantum dots

To characterize the morphology of the GQDs, a high resolution TEM was performed, (Figure 20). The lattice spacing of GQDs from the Figure 20(c) is about 0.286 nm, indicating the characteristic structure of the graphitic carbon. The size distribution measured by the DLS is shown in Figure 20(d), indicating the uniform size distribution of hydrodynamic diameters (6.5 ± 2.3 nm). XRD was also performed to characterize the graphitic nature of the GQDs. As shown in Fig. 21, there was a broad peak centered at $2\theta = 25^\circ$, corresponding to an interlayer spacing of 0.286 nm, which may be caused by the graphite (002) planes. The result was consistent with other paper reported on GQDs.¹³¹

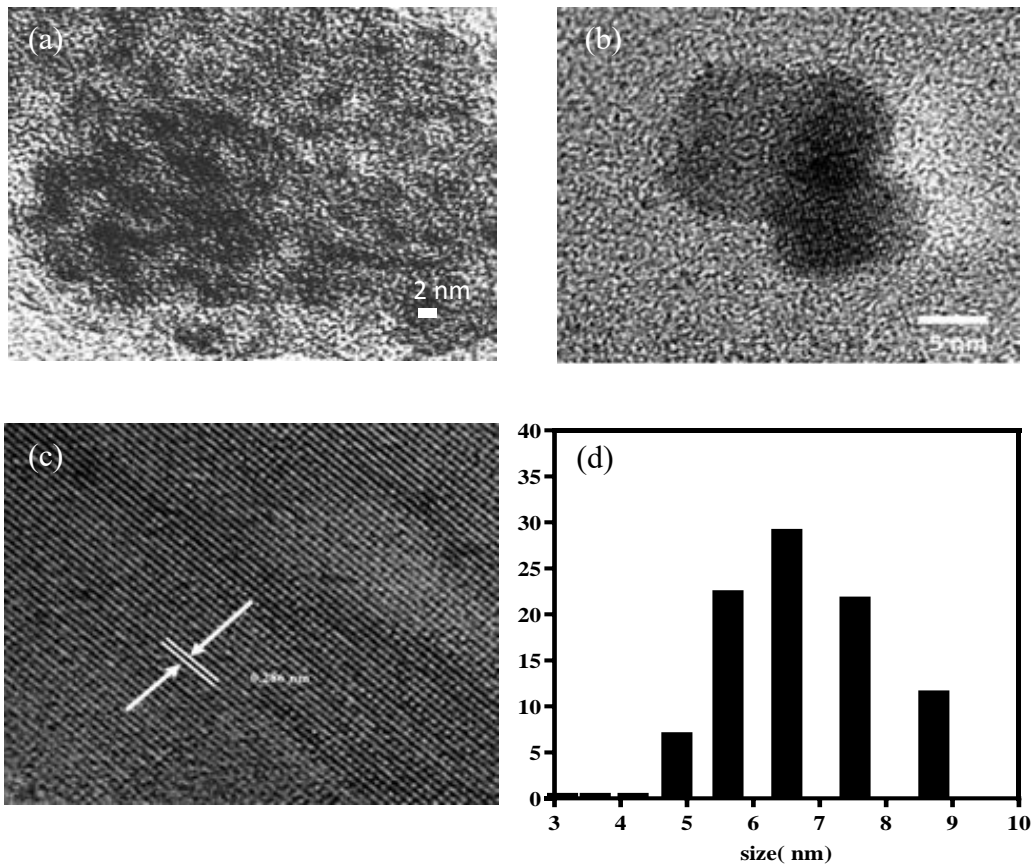


Figure 20. (a),(b) TEM images of the GQDs. (c) HRTEM image of the GQDs (0.286 nm). (d) The size distribution of the GQDs detected by DLS.

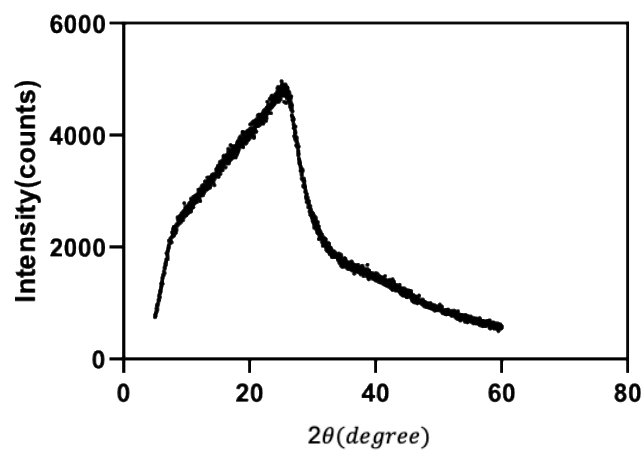


Figure 21. XRD patterns of the GQDs.

FT-IR spectroscopy and X-ray photoelectron spectroscopy (XPS) are commonly used to study the surface groups of the GQDs and analyze their components.

The composition of the obtained GQDs was characterized by XPS (Figure 22). The results showed two main peaks at 285.25 eV, and 432.5eV, which can be attributed to C 1s and O 1s, respectively. The atomic percentage of the carbon and oxygen were calculated be about 80 % and 20 %, respectively, which were the main elements in the GQDs. The C 1s spectrum of GQDs (Figure 22 b) showed five component peaks , including at 284.2 eV, 284.9 eV, 286.2 eV, 288. 2 eV and 288.9 eV indicated the presence of C=C, C-C/C-H, C-OH, C=O and -COOH, respectively. All these data from XPS analyses suggested that the C and O atoms existed in GQDs. These functional groups, including carboxyl groups, enabled the modification potential for future applications.

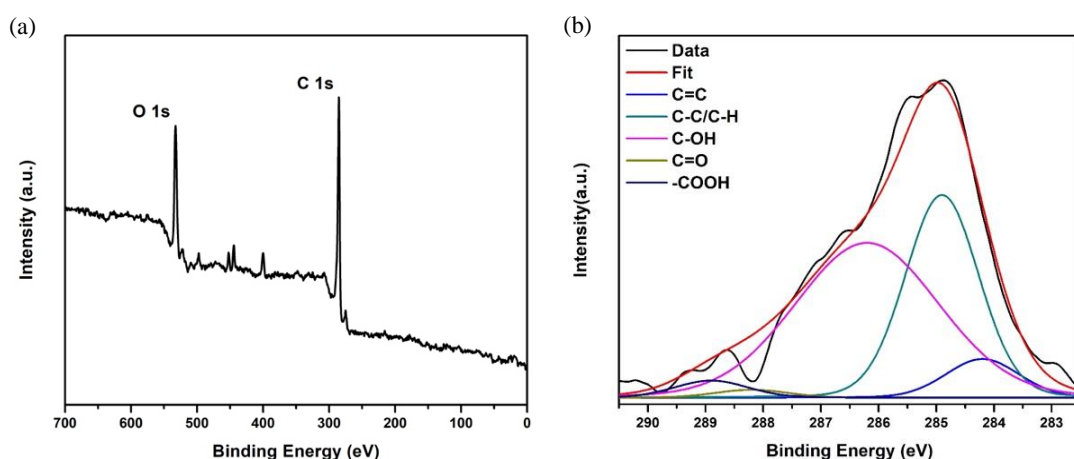


Figure 22. (a) Survey XPS spectra of the GQDs. (b) High resolution C 1s spectra of the GQDs.

FTIR was used to demonstrate the existence of various functional groups on GQDs. As shown in Figure 23, the peaks at 1070 cm^{-1} , 1250 cm^{-1} and 1400 cm^{-1} indicated the presence of the C-O-C, C-O and N-H stretching in graphite structure. The presence of carboxyl groups was proved by the broad peak area at 2970 cm^{-1} and the sharp peak at 1600 cm^{-1} . Besides the carbon related functional groups; the amine N-H functional group showed stretching vibrations of amine N-H at $3000 - 3500\text{ cm}^{-1}$.

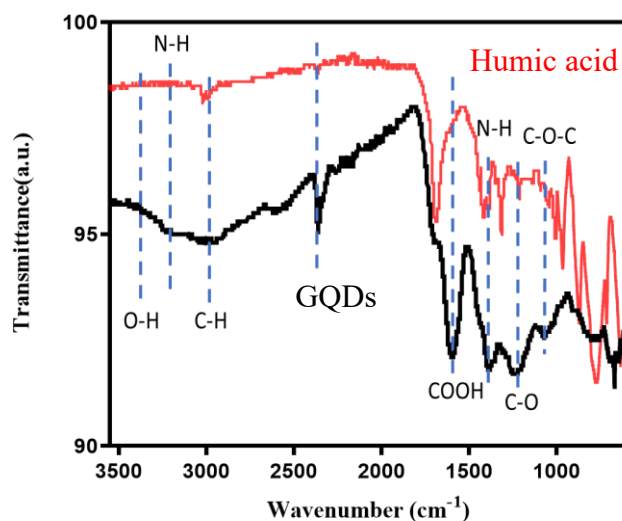


Figure 23. The FT-IR spectra of the GQDs and Humic acid.

3.3. Fluorescent properties.

Under the irradiation of 365 nm UV light, the GQDs showed strong white blue fluorescence (Figure 24A), indicating the formation of the fluorescent GQDs and a broad emission band. The excitation and emission spectra of GQDs were shown in Figure 24B. The strongest fluorescence emission was obtained when the excitation wavelength was set to 340 nm. Upon excitation at 340 nm, GQDs showed a strong fluorescence peak at 470 nm. In Figure 24C, the UV-Vis absorption spectrum of the GQDs aqueous solution showed a typically optical absorption in the ultraviolet (UV) region with a long tail expanding into the visible range. There is no obvious peak except the peak near 260 nm, which corresponding to a π to π^* transition of aromatic C=C bonds. In Figure 24D, the graphene quantum dots showed excitation-dependent emission. When the excitation wavelength increased from 260 nm to 560 nm, the emission wavelength increased from 440 nm to 590 nm. This excitation-dependent manner was consistent with most of the fluorescence properties of graphene quantum dots. In table 2, the morphology, color, quantum yield, stoke shift and preparation procedure of blue emission GQDs of some different methods were summarized and

compared. Both the quantum yield and stoke shift showed superior advantages than other GQDs, the preparation procedure was simpler, and the starting materials was lower cost.

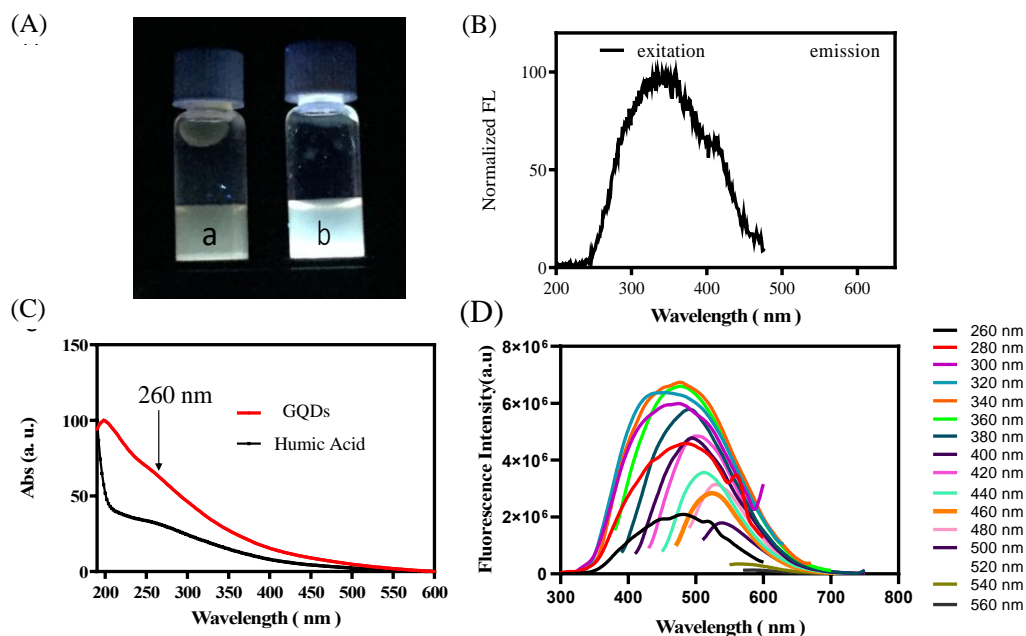


Figure 24. (A) photographs of humic acid (b) and GQDs (a) excited under 365 nm UV light). (B) Upon excitation at 340 nm, GQDs emit fluorescence peak at 470 nm. (c) UV-vis absorption spectrum of humic (a) and humic acid GQDs (b). (D) Fluorescence spectra the excitation wavelength increased from 260 nm to 560 nm, the fluorescence emission peak shifted from 440 nm to 590 nm.

Table 2. Comparison of this work with other methods of GQDs.

Methods	Starting Materials	Size (nm)	Color	Quantum yield (%)	Excitation, Emission Stoke Shift	Procedure, Reaction time	Reference
Acidic Oxidation	Carbon black	~18	Yellow	9.0	365 nm, 440 nm 75 nm	One pot, 24 h	137
Microwave	GO	2-7	Green, Blue	8.0	340 nm, 450 nm 80 nm	Multiple procedures	138
Hydrothermal	GO	5-13	Blue	5.0	320 nm, 430 nm 110 nm	Multiple procedures	139
K intercalation	Graphite flakes	~20	Blue	9.9	316 nm, 423 nm 107 nm	Multiple procedures	140
Precursor pyrolysis	Citric acid thiourea	~15	Blue	14.5	369 nm, 444 nm 75 nm	One pot, 2 h	141
This work	Humic acid	~6	White, Blue	20	340 nm, 470 nm 130 nm	One pot, 12 h	-

3.4. pH effect, photostability and stability on metal ions

In order to test the feasibility of the GQDs for bioimaging and biosensing, the photostability of GQDs were investigated. They exhibited superior photostability compared with the organic dyes, FITC. It was observed that no photobleaching appeared at a long irradiation period of 30 min (Figure 25A). In Figure 25B, the fluorescence intensity of GQDs showed significant difference at different pH. The emission intensity at 470 nm was used to compare from pH 1.00 to pH 12.00, the fluorescence intensity elevated when the pH of the GQDs solution increased from 1.00 to 9.00. Under strong basic condition from pH 10 to pH 12, the intensity was weakened. In particular, the emission exhibited stable fluorescence signal in the pH range of 5.00 to 9.00, indicating its applicability in physiological environments.

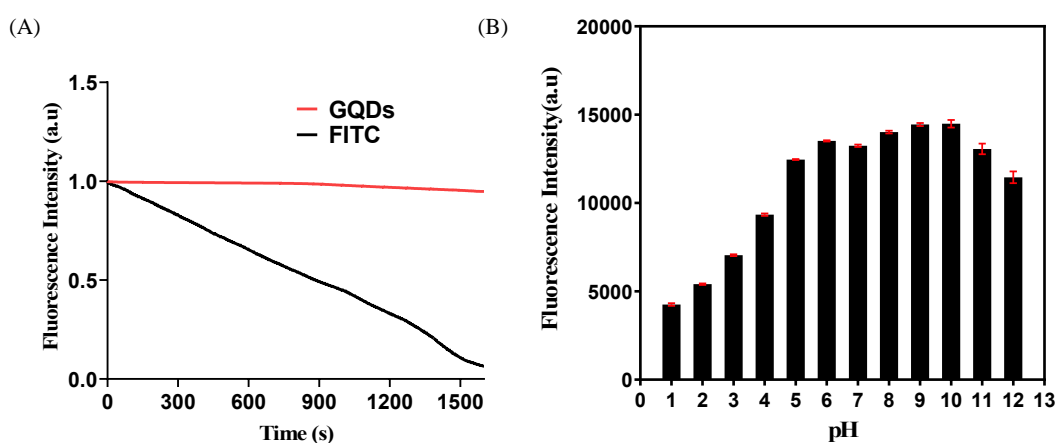


Figure 25. Photostability(A) and pH effect (B) of the GQDs

Moreover, we investigated the effect of different metal ions on the fluorescence intensity of GQDs. As shown in Figure 26B, a series of different metal ions were tested at the concentration of 20 μM . It showed that Cu^{2+} induced a significantly better fluorescence quenching than other metal ions.

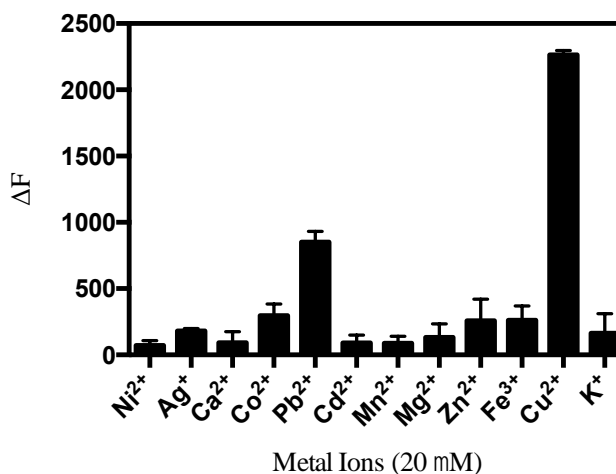


Figure 26. Effects of different ions (20 μM) on the fluorescence intensity of graphene quantum dots.

3.5. Experiment condition optimization.

In order to demonstrate the optimal conditions for reacting with Cu^{2+} , the effects of the concentration of GODs, the pH and the reaction time on the precipitation performance were studied.

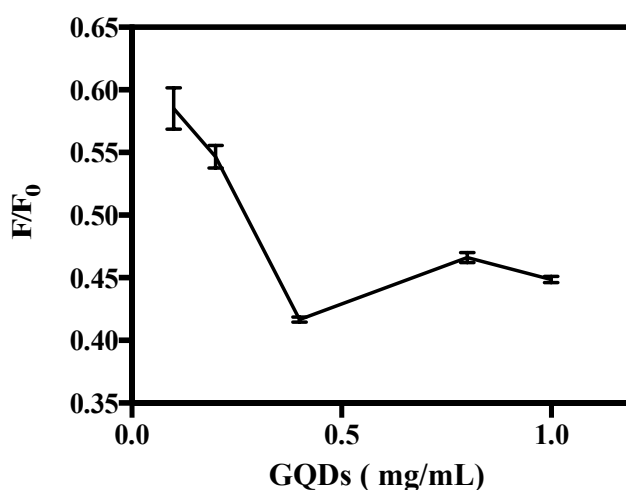


Figure 27. The effect of concentration of graphene quantum dots on the sensitivity of the assay. F referred to the fluorescence intensity of different concentrations of quantum dots treated with 50 μM Cu^{2+} in 20 mM HEPES (pH 5.0)

$\lambda_{\text{ex}} = 360 \text{ nm}$, $\lambda_{\text{em}} = 470 \text{ nm}$.

The concentration of GQDs was the first condition that required to be determined. A list of concentrations of GQDs were sonicated with 50 μM Cu^{2+} in 20 mM HEPES at pH 5.0 overnight. The fluorescence intensity of the above solution was recorded and designated as F . As a control, the same concentration of GQDs kept stirring overnight with adding the same amount of water only, the fluorescence intensity was defined as F_0 . The corresponding ratios of F to F_0 reached minimum value at the concentration of 0.40 mg/mL of GQDs, indicating the optimal sensitivity at this concentration. Therefore, we utilized the concentration GQDs at 0.40 mg/mL for the following experiments.

Additionally, the optimal pH and reaction time were required to be considered to reach the optimal result. The fluorescence intensities of GQDs at different pH were tested to evaluate the optimal pH. As shown in Figure 28, F_0 refers to the fluorescence intensity of 0.4 mg/mL GQDs without Cu^{2+} , and F refers to the fluorescence intensity of 0.4 mg/mL GQDs after the addition of 50 μM Cu^{2+} at various pH conditions. The ratio of F/F_0 was enhanced as the pH value elevated, indicating the pH-dependent quenching ability of GQDs. Obviously, at pH 5.0, the fluorescence quenching reached the lowest value, therefore the following experiments was performed at pH 5.0.

The time optimization was also tested in Figure 29, F_0 refers to the fluorescence intensity of 0.4 mg/mL GQDs at various time period as a control, and F refers to the fluorescence intensity of 0.4 mg/mL GQDs with the addition of 50 μM Cu^{2+} at various time period. It was observed that after 12 hours, the curve has reached plateau. Consequently, the reaction time was set to 12 hours.

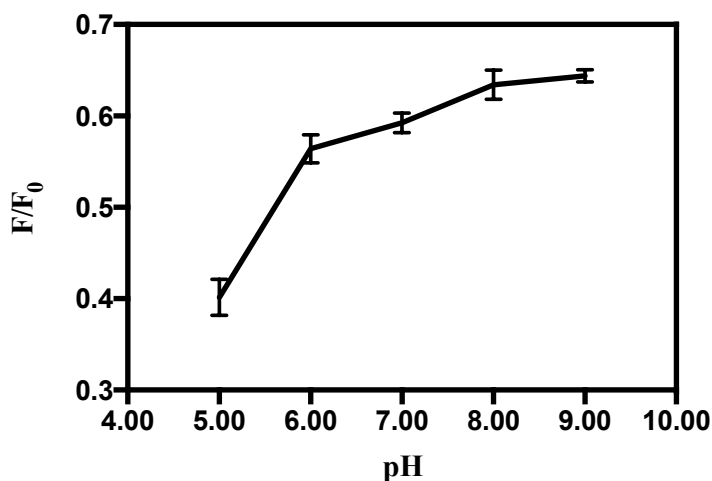


Figure 28. The effect of pH on the sensitivity of the sensor. F refers to the fluorescence intensity of different pH of the same concentration of quantum dots treated with 50 μM Cu^{2+} in 20 mM HEPEs (pH 5.0) $\lambda_{\text{ex}} = 360$ nm, $\lambda_{\text{em}} = 470$ nm.

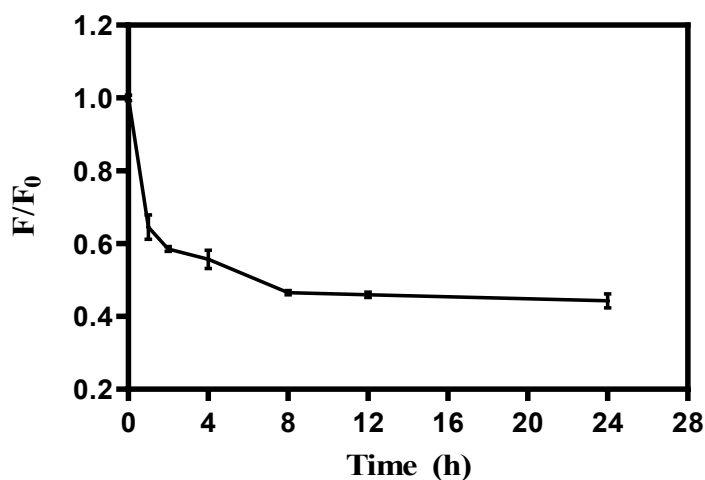


Figure 29. The effect of reaction time on the sensitivity of the assay. F refers to the fluorescence intensity of different pH of the same concentration of quantum dots treated with 50 μM Cu^{2+} in 20 mM HEPEs (pH 5.0) $\lambda_{\text{ex}} = 360$ nm, $\lambda_{\text{em}} = 470$ nm.

3.6. Cu^{2+} detection.

To analyze the sensitivity of the GQDs towards Cu^{2+} , 0.4 mg/mL of GQDs solution was mixed with various concentrations of Cu^{2+} for 12 h at room temperature

in 20 mM HEPES buffer at pH 5.0, the corresponding fluorescence intensity was recorded. As shown in Figure 30A, the fluorescence intensity of QDs decreased as the concentration of Cu^{2+} increased from 0 μM to 300 μM . The curve showed that the dynamic range was from 0 μM L to 300 μM (Figure 30), with a linear range between 0 μM to 40 μM (the inset of Figure 30B). The calibration curve showed a regression equation of $Y= 90.21X + 63.59$ with a correlation coefficient of 0.9984. Y and X represent the fluorescence intensity and the concentration of Cu^{2+} in unit of μM , respectively. The limit of detection (LOD) for the detection of Cu^{2+} was calculated to be 0.44 μM based on the slope of the equation ($3\sigma/s$), where σ was the standard deviation of three blank fluorescence intensities and s was the slope of the calibration curve. This LOD could ensure the Cu^{2+} detection in drinking water, because the Environmental Protection Agency (EPA) has required the highest concentration level of Cu^{2+} in drinking water to be 20 μM . Therefore, this assay is qualified for the drinking water monitoring.¹⁴²

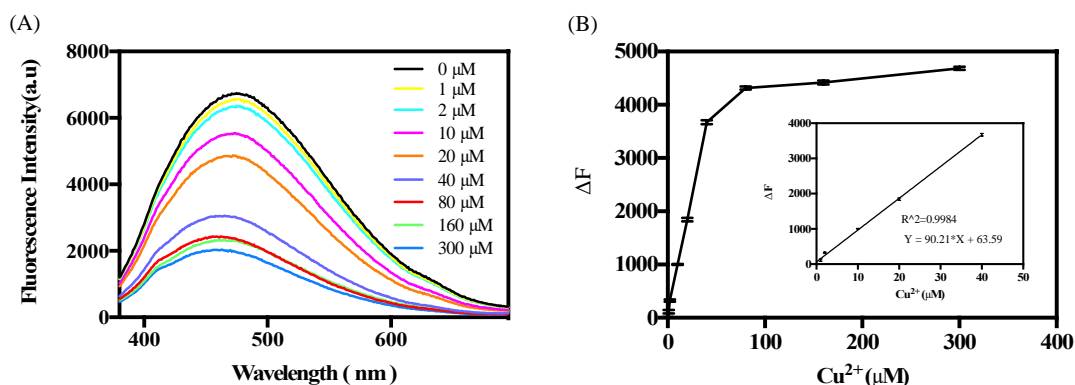


Figure 30. Fluorescence spectra of quantum dots incubation with different concentrations of Cu^{2+} in 20 mM HEPES (pH 5.0) from 0 μM to 300 μM . (B). The plot of the fluorescence intensity with different concentrations of Cu^{2+} . The inset graph shows the calibration curve of the sensor. $\lambda_{\text{ex}} = 360 \text{ nm}$, $\lambda_{\text{em}} = 470 \text{ nm}$. (LOD: 0.44 μM)

3.7. Analysis of spiked sample.

To validate GQDs as a Cu^{2+} sensing reagent, a series of different concentrations of Cu^{2+} was added into the Red River water as spiked samples (Table 3).

The final Cu^{2+} concentration was 10 μM and 20 μM . The ICP-MS method was performed as a standard method to compare with this Cu^{2+} GQDs sensing approach. The results showed a good correspondence for both samples.

Table 3. Comparison of the spike recovery of ICP-MS Methods with Designed GQDs essay.

Samples	Spikes (μM)	Detected (μM)	Recovery of this assay (%) (n=3)
River water (Red river)	10	11.30 ± 0.93	113 ± 9.3
	20	23.044 ± 0.20	115 ± 1.0
Samples	Spikes (μM)	Detected (μM)	Recovery of ICP-MS (%) (n=3)
River water (Red river)	10	10.28 ± 1.78	103 ± 17.8
	20	20.27 ± 1.49	102 ± 7.5

4. Conclusions

We have developed a facile procedure to produce the blue emissive graphene quantum dots using humic acid that were extracted from soil, peat, and coal. The fluorescence intensity of this new developed quantum dots was proportional to the concentration of Cu^{2+} based on its fluorescence quenching to GQDs. The optimized assay provided a linear range from 1 μM to 40 μM $\text{Cu}(\text{II})$, and a detection limit of 0.44 μM $\text{Cu}(\text{II})$. The method was used to test red river by spiking $\text{Cu}(\text{II})$. The accuracy was proved by inductively coupled plasma mass spectrometry (ICP-MS).

CHAPTER IV

TWO READOUTS SENSOR USING EU COORDINATED MEH PPV POLYMER DOTS FOR THE DETECTION OF COPPER (II) IONS

Introduction

Metal pollution has been considered as a serious safety issue due to its wide and long-term effect.¹⁴³ Therefore, metal ion monitoring in river, lake and other natural resources is significantly necessary for environmental protection and ion cycling in biological systems.¹⁴⁴ In order to accurately monitor the metal ion concentrations, it is essential to conceive the basic principles and benefits for different methods on metal analysis. There were plenty of analysis methods for elemental analysis, including atomic absorption/emission spectrometry (AAS/AMS), induced coupled plasma mass spectrometry (ICP-MS), fluorescence methods and nuclear techniques.¹⁴⁵⁻¹⁵⁰ Each of those methods utilized one signal to quantify the amount of element. Among all these methods, fluorometric methods have been regarded as a faster and simpler methodology, the diversity of fluorescence probes including all kinds of nanomaterials, such as organic dyes, quantum dots, nanoclusters and semiconducting polymer dots.¹⁵¹⁻¹⁵³ However, those fluorescent nanoprobe suffer from the same limitations, such as high background noise in some complex matrix, photobleaching problems of fluorescent probes and high limit of detection.¹⁵⁴ Besides, most of the detection limit of fluorescent nanoprobe is in the micromole range, which would prevent their further application in low detection range such as nanomolar detection. In order to improve the feasibility of the fluorescent nanoprobe in low detection range, a single pattern of fluorescence signal could not suffice, an ultrasensitive signal is required to play a role in this sensing system to construct a two readouts nanoprobe.

Recently, a new technology called single particle inductively coupled plasma-mass spectrometry (spICP-MS) has emerged as a promising analytical approach for

metal-containing nanoparticles in an aqueous matrix.¹⁵⁵ During the sample acquisition time period, each metal-containing nanoparticle was ionized by a plasma torch, producing an ion cloud containing the target isotope. Within one dwell time period, a single particle was controlled to be collected and shown as one single peak. Consequently, one peak represented the detected metal signal from one single particle. The intensity of the isotope peak is directly proportional to the amount of metal element doped in a single nanoparticle. Most importantly, spICP-MS is a “particle by particle” detection process which requires all the particle solutions to be detected at an extremely low concentration. Each single spike exhibits the isotopic signal collected from the detected metal doped nanoparticle and high intensity of the spike represents the more Eu element in one single nanoparticle. Theoretically, if two nanoparticles aggregated together, a higher intensity will be recorded, the more nanoparticles are agglomerated, the higher intensity will be detected, while the spike number will be reduced, which makes spICP-MS an effective tool for ultrasensitive assay. Therefore, spICP-MS signal would be a good output to improve the fluorescent nanoprobe.

A two readouts nanoprobe was developed to achieve excellent sensitivity, a broad linear range and absolute nanoparticle concentration quantification. Eu^{3+} , as a lanthanide element, is one of the rarest rare metal elements on the earth and shows little toxicity when compared with other heavy metals. Therefore Eu^{3+} is a suitable metal isotope to be applied in spICP-MS analysis because of the lower background signal. When considering a suitable matrix to combine both a spICP-MS signal and a fluorescence signal, semiconducting polymer nanoparticles (SPNs) would be a great choice to fulfill the purpose. There are three main advantages for using SPNs. First, SPNs could be designed to contain a large amount of metal ions that will enhance the spICP-MS signal versus background noise. Second, semiconducting polymer

nanoparticles exhibit superior fluorescence properties, such as high quantum yield, large Stokes shift, and high photostability. Third, the synthesis process of lanthanide doped SPNs is simple, without a tedious purification protocol.¹⁵⁶ Considering this, a novel two-readouts nanoprobe fabricated from Eu^{3+} -coordinated MEH-PPV polymer nanoparticles was designed.

Copper, as a pivotal metal in human life, is involved in various physiological functions in biological activities, especially in cell generation and enzymatic processes.¹⁵⁷⁻¹⁵⁸ However, copper exhibits high toxicity if over-ingested. For example, through the food chain, copper has been proved to be a direct reason to increase the outbreak rate of multiple serious neurodegenerative diseases, such as Wilson and Parkinson's.¹⁵⁹⁻¹⁶⁰ In addition, Cu^{2+} disturb the normal functioning of organs, including gastrointestinal, kidney and liver.¹⁶¹ The identification and measurement of copper ions (Cu^{2+}) in environmental matrices and biological fluids are in great need. Thus, we chose copper as a model to test the applicability of this two readouts nanoprobe. Taking advantage of the paramagnetic properties of Cu^{2+} , many fluorescence probes have been designed to detect fluorescence signals influenced by Cu^{2+} ions. In addition, Irving–Williams Series proves that transition metal Cu^{2+} has tendency to form complex with carboxylic groups. The aggregation induced fluorescence quenching, the mechanisms include photoinduced electron transfer, fluorescence resonance energy transfer, charge transfer and some other interactions that occurred at the fluorescence nanoprobe surface.¹⁶²⁻¹⁶⁷

In this chapter, a novel two-readouts sensor fabricated from Eu^{3+} -coordinated MEH-PPV polymer nanoparticles was designed for the detection of copper ion (Cu^{2+}). One readout was based on the fluorescence signal emitted by the fluorescent matrix of MEH-PPV polymer nanoparticles. Cu^{2+} , compared to other element ions, have efficient

chelating interactions with carboxylic groups. They will be captured by carboxylic groups on the polymer nanoparticles and result in a significant fluorescence quenching. The other readout was based on the Eu mass signal from SPN-Eu; the aggregation of the SPN-Eu not only causes the fluorescence quenching but can also increase the size of the particle and decrease the spike numbers, which could be quantitated by single-particle inductively coupled plasma mass spectrometry (ICP-MS). Therefore, the concentration of Cu^{2+} would be proportional to both the fluorescence and ICP-MS signals. This assay provides a rapid and selective detection method for Cu^{2+} with an extremely low detection limit, indicating its superior potential applied in environmental monitoring.

2. Experimental Section

2.1. Materials and Instruments.

Poly[2-methoxy-5-(2-ethylhexyloxy)-1,4-phenylenevinylene] (MEH-PPV, average molecular weight is 40,000–70,000), europium(III) chloride, 4-(2-hydroxyethyl)piperazine-1-ethanesulfonic acid, (HEPES, 99.5%, ACS grade), copper(II) sulfate, potassium chloride, sodium chloride, magnesium(II) sulfate, zinc(II) sulfate, manganese(II) dichloride, lead(II) sulfate and tetrahydrofuran (THF, 99.9%, inhibitor-free, ACS grade) were purchased from Sigma Aldrich. Poly(styrene-co-maleic anhydride) (PSMA) was purchased from Polymer Source Inc. and used as received without further purification. Ultra-purified water (18.3 M Ω cm) used in all experiments was obtained using a Milli-Q Millipore water purification system.

A UV/VIS/NIR Spectrometer (Lambda 1050, PerkinElmer) was used to measure the absorption of samples. Fluorescence measurements were performed on a RF-6000 fluorophotometer (SHIMADZU). The excitation wavelength was set to be

480 nm and the emission was recorded from 500 nm to 700 nm. The fluorescence intensity at 560 nm was selected to evaluate the performance of SPN-Eu probe for Cu²⁺ detection. Both the widths of excitation and emission slits were 10.0 nm. All the experiments were carried out at room temperature. A Zetasizer particle analyzer (Nano – ZS, Malvern) was used to measure hydrodynamic diameters and surface charges of nanoparticles. A Hitachi 7500 transmission electron microscope (TEM) and a scanning electron microscope (SEM, SU8010, Hitachi) were used to obtain the morphology of the synthesized nanoparticles. An iCAP Qc ICP-MS (Thermo Scientific, Bremen, Germany) was used to all the spICP-MS measurements. Samples were introduced using a Teledyne CETAC ASX560 autosampler (Omaha, NE), a 4-channel 12-roller peristaltic pump, a microflow perfluoroalkoxy nebulizer and a Peltier-cooled quartz cyclonic spray chamber. The sample flow rate was set to ~ 0.20 mL min⁻¹. The ICP-MS was tuned daily for maximum ²³⁸U and minimum ¹⁴⁰Ce¹⁶O/¹⁴⁰Ce oxide level (< 0.03) with THERMO-4AREV (Thermo Scientific) standard solution in STDs mode. Detailed information about the ICP-MS operation parameters are provided in Table 4. The dwell time and data collection time for all the spICP-MS measurements were 10 ms and 180 s. Isotope ¹⁵³Eu intensity was recorded using Qtegra™ software (version 2.8.2944.202).

Table 4. Operation parameters used for spICP-MS measurements.

Parameters	Value
Radio Frequency Power (W)	1550.00
Cool Gas (L min ⁻¹)	14.00
Nebulizer Gas Flow (L min ⁻¹)	1.09
Spray Chamber Temperature (°C)	2.70
Sampling Depth	5.00
Peristaltic Pump Speed (rpm)	20.00

2.2. Synthesis of the Eu coordinated MEH-PPV semiconducting polymer nanoparticles (Eu-SPN).

First, an aliquot of 15 μL of EuCl_3 solution (10 mg/mL) was mixed with 4.4 mL of THF, followed by adding 500.0 μL of 1.0 mg/mL PSMA solution, and then stirred for one hour. Second, an aliquot of 50.0 μL of 0.50 mg/mL MEH-PPV polymer was added to reach the final volume of 5.0 mL. Then, each aliquot of 5.0 mL of the above solution was quickly injected into 10.0 mL of DI water under ultrasonication in the ice bath for about 1.0 min. Finally, THF solvent was evaporated on a hot plate.

2.3. Characterization of Eu-SPN.

The TEM was employed to image the structure of Eu-coordinated semiconducting polymer nanoparticles (Eu-SPN). The hydrodynamic diameter and surface potential of the Eu-SPN were characterized using the nano sizer. The elemental analysis was performed using EDS.

2.4. Cu^{2+} detection using the fluorometric method and spICP-MS

An aliquot of 100.0 μL of 5.0 ppm of Eu-SPN solution was incubated with different concentrations of Cu^{2+} for 1.0 h in a HEPES buffer solution (20 mM, pH 7.0) to reach a total volume of 1.0 mL at room temperature with regular shaking. Then, with the excitation of 480 nm, the fluorescence intensity of Eu-SPN at 560 nm was recorded at each Cu^{2+} concentration. The concentration of Cu^{2+} ranged from 0 to 80 μM . For spICP-MS detection, the above prepared Eu-SPNs were first diluted to 10^4 particles/mL with DI water and then introduced into spICP-MS.

2.5. Selectivity investigation of SPN-Eu in Fluorometric and spICP-MS Methods.

In order to investigate the sensitivity of SPN-Eu on different metal ions, 1.0 mL of 1.0 ppm of SPN-Eu solution was added with different metal ions, Pure water was used as

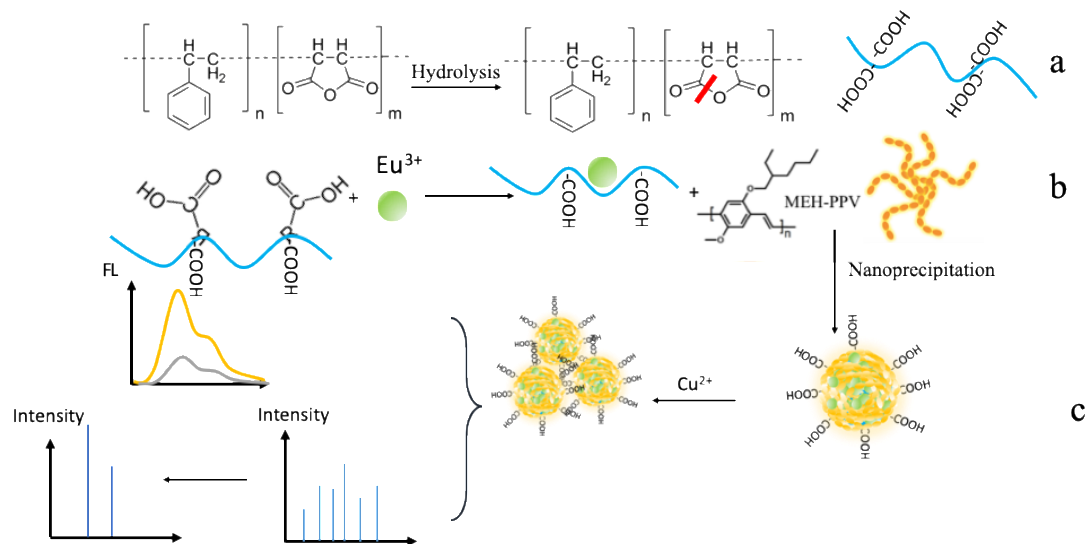
a control. The concentrations of the metal ions were fixed at 50 μM . For the selectivity in spICP-MS assay, the samples were performed at the sample reaction condition but with a series of metal ions at the concentration of 1.0 μM .

3.0. Results and Discussion

3.1. Design of the Eu-SPN sensing platform

In this work, we designed an Eu-SPN Cu^{2+} nanoprobe with high fluorescence and high spICP-MS signals. In the beginning, PSMA polymer was hydrolyzed to functionalize the carboxylic groups, and then followed by adding EuCl_3 THF/ethanol solution with vigorous stirring for 2 h (Scheme 4). During this period, PSMA served as a highly efficient absorbent to extract Eu^{3+} by the spontaneous chelation interactions.¹⁵⁹ After the immobilization, MEH-PPV polymer was blended in, and then the whole polymer mixture was injected into water with sonication in ice bath to form Eu-SPN. For this two-readout copper nanoprobe, one readout was fluorescence signal from the fluorescent MEH-PPV polymer, the other one was provided by the heavy loading of Eu^{3+} ions in Eu-SPN. Cu^{2+} , compared with other element ions, have efficient chelating interactions with carboxylic groups, which results in nanoparticle aggregation as well as a significant fluorescence quenching. Higher Cu^{2+} concentration resulted in higher aggregation. Meanwhile, in the presence of Cu^{2+} , the aggregation induced an increased spICP-MS intensity and a decreased number of the spikes. In the single particle analysis mode, the number of Eu-SPN entering the plasma could be quantified by counting the spikes. One spike refers to one particle, before adding Cu^{2+} . After adding Cu^{2+} , two or more nanoparticles agglomerated together went through the plasma. This caused the signal intensity to be enhanced but the number of pulses to decrease, which directly corresponded to the Cu^{2+} concentration. The spICP-MS can detect less than 100 Eu-SPN per mL, which is extremely lower than the LOD of the fluorescence signal detected

by a fluorophotometer. We believe that this assay will provide a rapid and selective detection of Cu^{2+} with an extremely low detection limit.



Scheme 4. Schematic illustration of Cu^{2+} detection by Eu coordinated MEH-PPV semiconducting polymer nanoparticles.

3.2. Synthesis and characterization of Eu-SPN

To prepare the designed SPN-Eu, PSMA was first hydrolyzed to produce two carboxylic groups at each unit on the polymer chain (Scheme 4 a). With the assistance of chelating interactions between two adjacent carboxylic groups, Eu^{3+} was doped on the PSMA chains during the stirring (Scheme 4 b). After adding MEH PPV fluorescent polymer, carboxylic functionalized Eu-SPN was formed during the process of nanoprecipitation. The morphology and size of SPN-Eu was characterized with a regular transmission electron microscope (TEM) and dynamic light scattering (DLS), as shown in Figure 31, SPN-Eu showed round-shaped well-dispersed nanoparticles, the zeta potential and hydrodynamic size of Eu-SPN and SPN were also tested. The hydrodynamic size was significantly increased after doping Eu^{3+} into the MEH-PPV polymer nanoparticles. The zeta potential of SPN-Eu and SPN were both lower than -20 mV, ensuring the doping process won't affect the relative stability of the SPN-Eu in the aqueous solution.

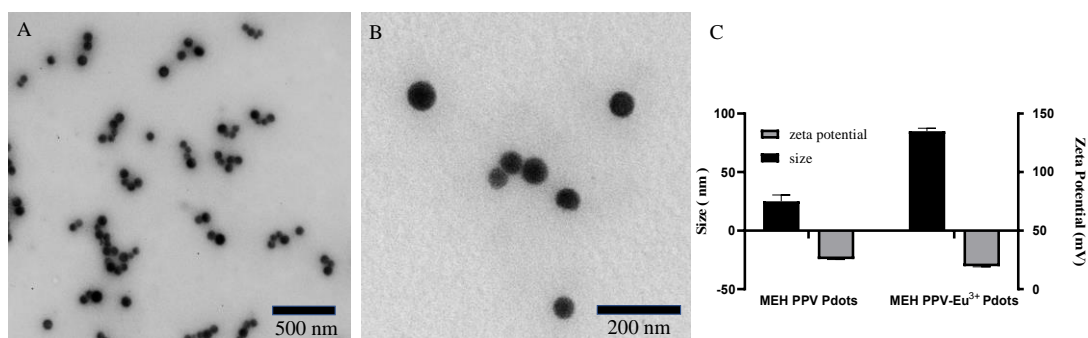


Figure 31. (A) TEM image of SPN-Eu (500 nm) (B) TEM image of SPN-Eu (200 nm) (C) Size distribution and zeta potential (pH 7.0 10 mM HEPES) of MEH PPV SPN and MEH PPV- Eu³⁺ SPN

3.3. Feasibility investigation of Cu²⁺ detection using fluorescence and spICP-MS.

To demonstrate the feasibility of Cu²⁺ detection using spICP-MS, the effective peak number from SPN-Eu without Cu²⁺ during the acquisition period was required. Furthermore, to guarantee single nanoparticle collected in each dwell time during spICP-MS measurements, particle number concentration of SPN-Eu was investigated. As shown in Figure 32a-f, the particle number concentration of SPN-Eu ranging from 5.0×10^3 , 1.0×10^4 , 2.0×10^4 , 3.0×10^4 to 5.0×10^4 Particles per mL was introduced into the spICP-MS. For SPN-Eu, with the increasing of particle number concentration, the collected peak number increased.

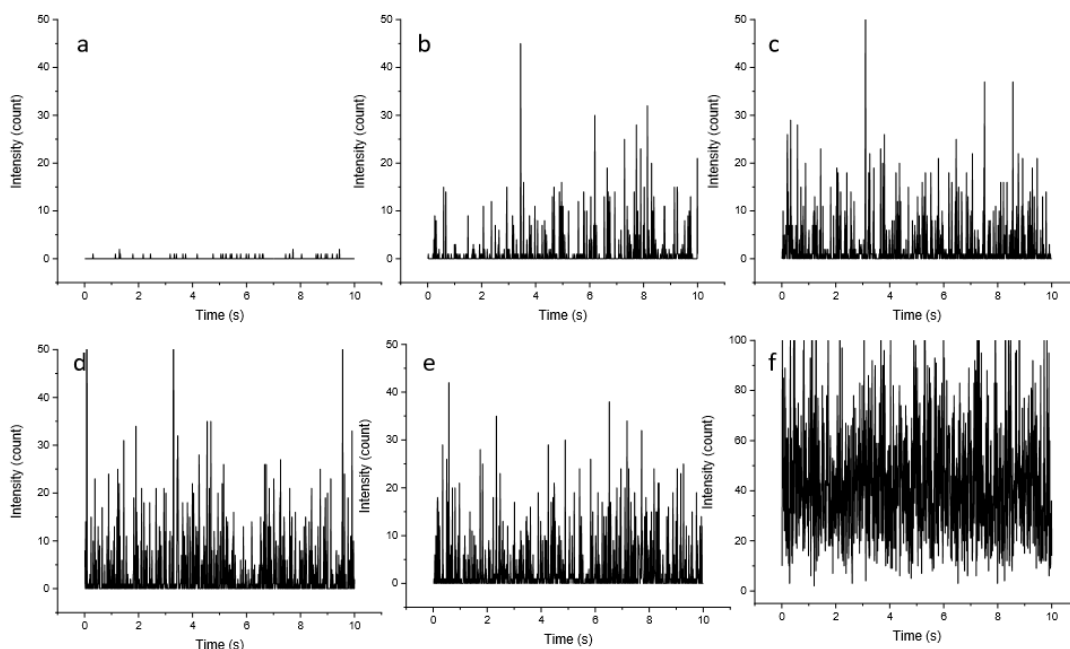


Figure 32. Increasing the particle number concentrations of Eu-SPN (a: 0 P/mL, b: 5.0×10^3 P/mL, c: 1.0×10^4 P/mL, d: 2.0×10^4 P/mL, e: 3.0×10^4 P/mL, f: 5.0×10^4 P/mL). (^{153}Eu , dwell time: 10 ms).

However, increasing the particle number concentration to 5.0×10^4 Particles/mL, the baseline from isotope Eu increased as well. The multiple nanoparticles would be monitored in each dwell time, which led to continuous spikes instead of individual spikes. The results showed that the concentration at 1.0×10^4 P/mL contained both high spike number and individual spikes. Consequently, before injecting into the spICP-MS, the particle number concentration was diluted to 1.0×10^4 P/mL in the following experiments.

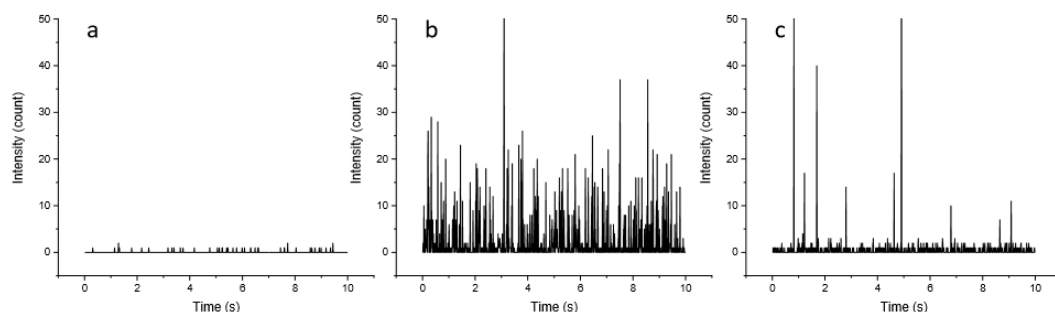


Figure 33. spICP-MS spectra of Eu-SPN in the presence of Cu^{2+} at $100 \mu\text{M}$ (a: 0 P/mL, b: 1.0×10^4 P/mL, c: 1.0×10^4 P/mL, Cu^{2+} concentrations in $100 \mu\text{M}$). (^{153}Eu , dwell time: 10 ms).

Figure 33 showed raw spICP-MS data for 10 s of the 180 s acquisition period. These data demonstrated that the spike number was substantially decreased with the existence of Cu^{2+} . The increased spike intensity and decreased spike number were also consistent with mechanism of the aggregation process. These clear different signals demonstrated the feasibility of spICP-MS detection. In the meanwhile, Figure 34 showed, SPN-Eu emitted fluorescence at 560 nm with the excitation of 480 nm (curve a). When Cu^{2+} was added with the SPN-Eu and sonicated for 60 min, the fluorescence intensity was decreased (curve b), indicating the outstanding fluorescence response to Cu^{2+} . In contrast, compared with control, a relative high fluorescence intensity was collected without mixing with Cu^{2+} (curve a).

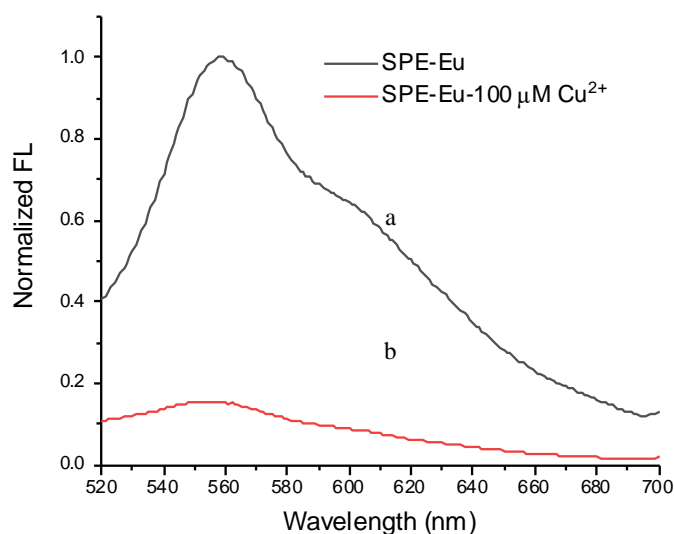


Figure 34. Fluorescence spectra of SPE-Eu under two conditions. (a) SPN-Eu (b) SPN-Eu + 100 μM Cu^{2+} , $\lambda_{\text{ex}} = 480$ nm, $\lambda_{\text{em}} = 560$ nm.

3.4. Optimization of the reaction conditions

The effect of the concentration of SPN-Eu on the fluorescence intensity was investigated in Figure 35. The fluorescence intensity of SPN-Eu was studied by measuring the fluorescence intensity of different concentrations of SPN-Eu in the solution of 100 μM of Cu^{2+} in 10 mM HEPES at pH 7.4. The concentrations of SPN

were 5.0 ppm, 2.0 ppm, 1.0 ppm, 0.5 ppm, 0.1 ppm and 0.05 ppm respectively. The fluorescence spectra were recorded in the range of 500 nm to 750 nm using an excitation wavelength of 480 nm. Fluorescence intensity of the SPN-Eu nanoparticle solution added with Cu^{2+} was recorded as F. The fluorescence of the same concentration of SPN-Eu was defined as F_0 . In the lower concentration of SPN-Eu, the ratio of F to F_0 was high because of the high background noise comparing to the low fluorescence signal. In the high concentration of SPN-Eu, the ratio of F to F_0 was also high, which is due to the decreased fluorescence was not significant comparing to the high fluorescence of SPN-Eu. Therefore, the shape of the curve decreased first and then increased as the concentration of SPN-Eu enhanced. The corresponding ratios of F to F_0 reached minimum value at the concentration of 1.0 ppm of SPN-Eu, referring to the highest sensitivity at this concentration. Consequently, we stipulated the concentration of SPN-Eu to 1.0 ppm for the following experiments.

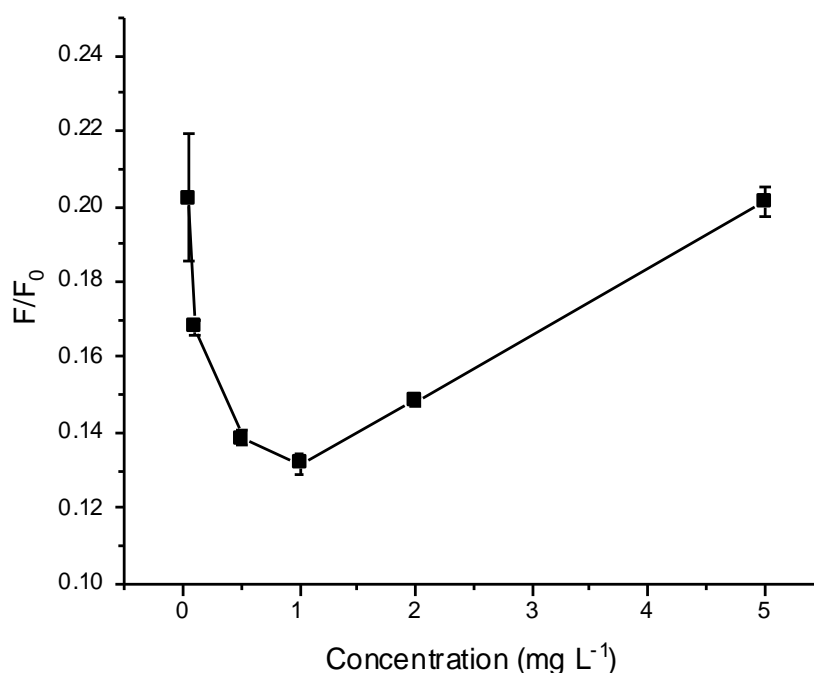


Figure 35. The effect of concentration of MEH-PPV-Eu SPN on the sensitivity of the

sensor. F referred to the fluorescence intensity of different concentrations of SPN treated with 50 μM Cu^{2+} in 20 mM HEPES (pH 7.0) $\lambda_{\text{ex}} = 480$ nm, $\lambda_{\text{em}} = 560$ nm, reaction time: 5.0 h.

Similarly, the impact of reaction time of Eu-SPN with Cu^{2+} ions was analyzed by measuring the fluorescence intensity of different reaction time period of Eu-SPN added into the solution of 50 μM of Cu^{2+} in 10 mM HEPES at pH 7.4. The reaction times were 0.5 h, 1 h, 3 h, and 5 h, respectively. The fluorescence spectra were recorded in the range of 480 nm to 700 nm using an excitation wavelength of 480 nm. The time optimization was shown in Figure 36, F_0 refers to the fluorescence intensity of 1.0 ppm of SPN-Eu at various time periods as a control, and F refers to the fluorescence intensity of 1.0 ppm of SPN-Eu with the addition of 50 μM Cu^{2+} at various time periods. It was observed that after 1.0 h the curve has reached a plateau. The following experiments were run for 1.0 h.

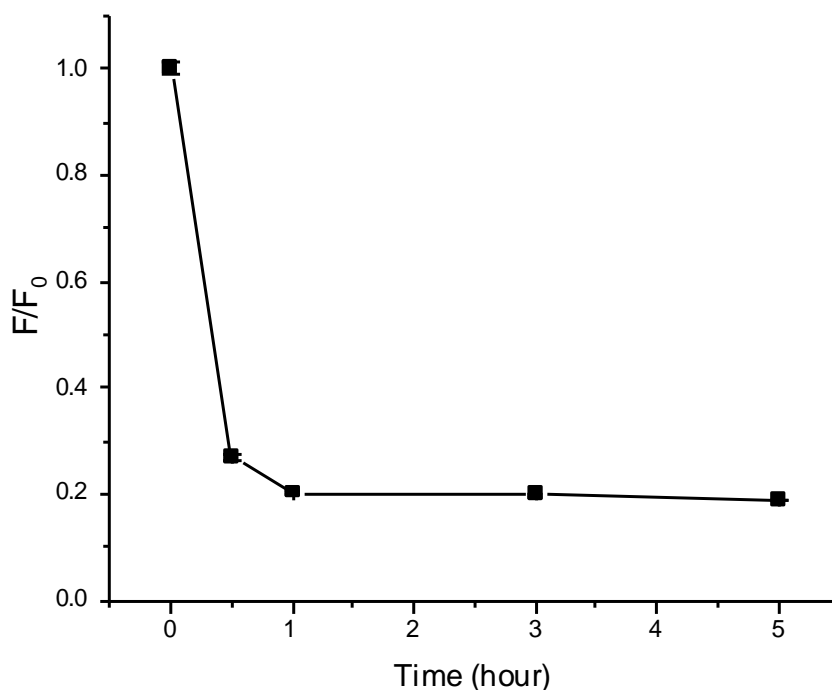


Figure 36. Time effect on the sensitivity of the MEH-PPV-Eu SPN. F referred to the fluorescence intensity of different time period of the 1.0 ppm of MEH PPV-Eu SPN treated with 50 μM Cu^{2+} in 20 mM HEPES (pH 7.0)

$\lambda_{\text{ex}} = 480 \text{ nm}$, $\lambda_{\text{em}} = 560 \text{ nm}$.

The pH was also an important factor in the aggregation reactions between the Cu^{2+} and nanoparticles. The fluorescence intensity of SPN-Eu mixed with Cu^{2+} at different pH conditions were recorded to assess the optimal pH condition. As shown in Figure 37, F_0 refers to the fluorescence intensity of 1.0 ppm of SPN-Eu without Cu^{2+} in various pH conditions, and F refers to the fluorescence intensity of 1.0 ppm of SPN-Eu with 100 μM Cu^{2+} at corresponding pH conditions. The ratio of F/F_0 was decreased as the pH value was increased from 1.0 to 7.0, indicating the pH-dependent quenching ability of GQDs. In low pH conditions, the protonation of the carboxylic groups shielded the SPN-Eu from chelating with Cu^{2+} , therefore the ratio of F to F_0 was higher. In high pH conditions, the ratio of F to F_0 was lower because of the stronger interactions between negative charged carboxylic groups and positive charged Cu^{2+} . Obviously, at pH 7.0, the fluorescence quenching reached the lowest value. Therefore, the following experiments were performed at pH 7.0.

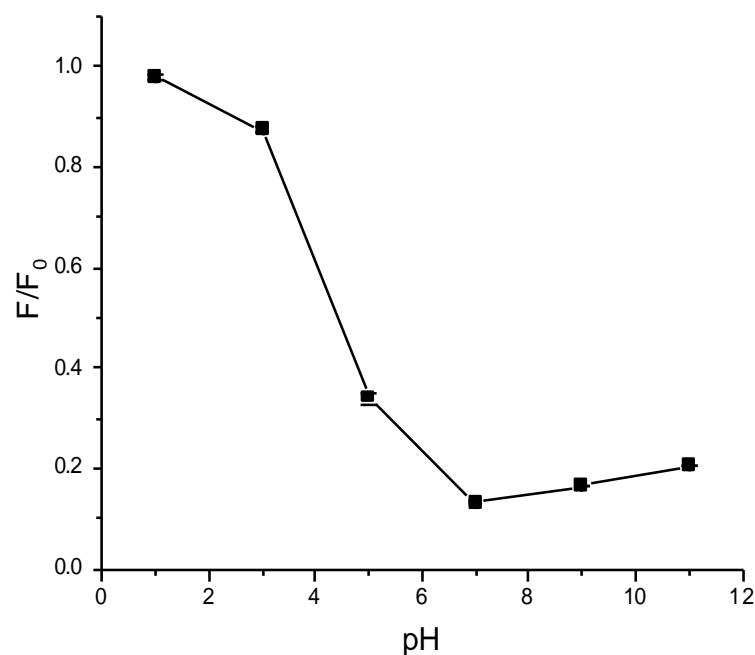


Figure 37. The effect of pH on the sensitivity of MEH-PPV-Eu SPN. F refers to the fluorescence intensity of the 0.1 ppm of MEH PPV-Eu SPN treated with 50 μM Cu^{2+} at different pH in 20 mM HEPES, $\lambda_{\text{ex}} = 480$ nm, $\lambda_{\text{em}} = 560$ nm, reaction time :1.0 h.

3.5. Sensitivity of SPN-Eu on Cu^{2+} by fluorescence

To evaluate the fluorescence quenching ability of Cu^{2+} to SPN-Eu under optimal conditions, 1.0 ppm of SPN-Eu solution was sonicated with various concentrations of Cu^{2+} (0 μM , 2 μM , 5 μM , 10 μM , 20 μM , 40 μM , 50 μM , 60 μM and 80 μM , respectively) for 1 h at room temperature in 20 mM HEPES buffer at pH 7.0. The corresponding fluorescence intensity was recorded. As the concentration of Cu^{2+} increased, the fluorescence intensity at 560 nm substantially reduced (Figure 38A).

The results showed that the dynamic range was from 0 μM L to 80 μM (Figure 38B), with a linear range from 2 μM to 50 μM (the inset of Figure 38B). The calibration curve showed a regression equation of $Y = -136.5X + 8538$ with a correlation coefficient of 0.9905. The limit of detection (LOD) for the detection of Cu^{2+} was calculated to be 0.29 μM based on the slope of the equation ($3\sigma/s$), where σ was the standard deviation of three blank fluorescence intensities and s was the slope of the calibration curve. This LOD could ensure the detection of Cu^{2+} in river or drinking water.

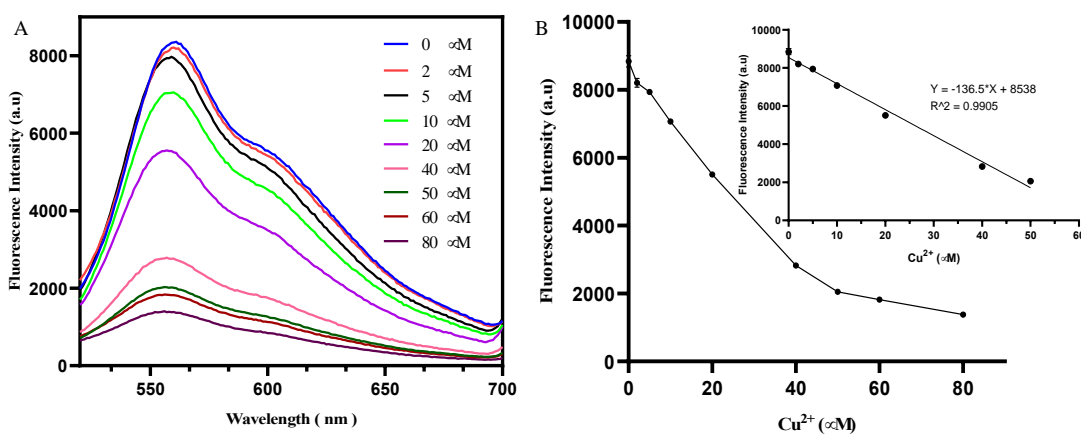


Figure 38. The effect of various Cu^{2+} concentrations on the fluorescence intensity of MEH-PPV-Eu SPN in pH 7.0 10 mM HEPES $\lambda_{\text{ex}} = 480$ nm, $\lambda_{\text{em}} = 560$ nm, reaction time 1.0 h.

3.6. Selectivity of SPN-Eu on various metal ions by fluorescence

A selectivity study for Cu^{2+} over different metal ions is shown in Figure 39. The same concentration of Cu^{2+} and other ions, Ni^{2+} , Co^{2+} , Fe^{2+} , Fe^{3+} , Pb^{2+} , Mg^{2+} , Cd^{2+} , Ag^+ , Zn^{2+} , Al^{3+} , Mn^{2+} (50 μM), were added into 1.0 ppm of the SPN-Eu solution in pH 7.0, 20 mM HEPES for 1.0 h. The fluorescence spectra were recorded in the range of 480 nm to 750 nm using an excitation wavelength of 480 nm. F_0 refers to the fluorescence intensity of 1.0 ppm of SPN-Eu at various metal ions as a control in the optimal condition, and F refers to the fluorescence intensity of 1.0 ppm of SPN-Eu with an addition of same concentration of various metal ions. The results showed a significantly lower

fluorescence intensity with Cu^{2+} than with other metal ions.

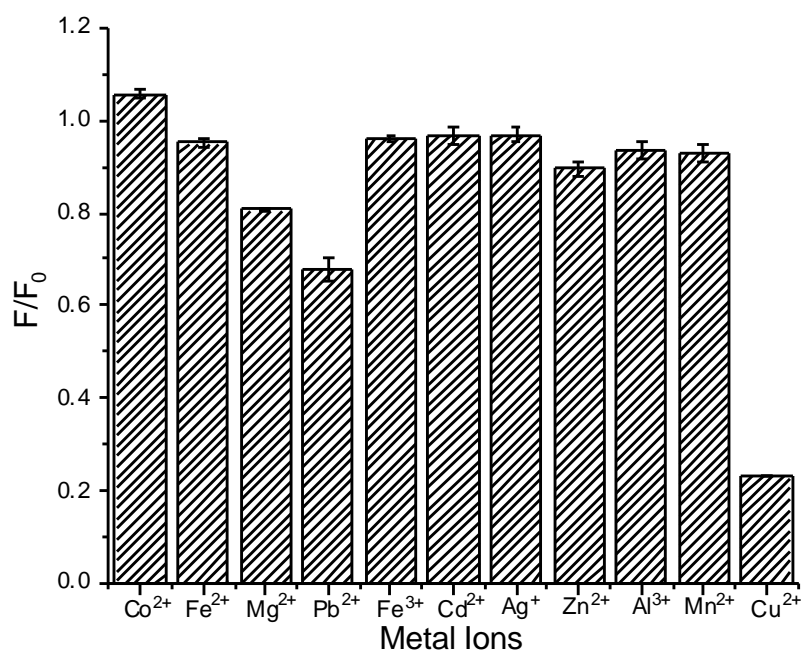


Figure 39. Effects of different ions (50 μM) on the fluorescence intensity difference of Eu-SPN in pH 7.0 for 1.0 h.

3.7. Cu^{2+} detection in spICP-MS

spICP-MS detection of SPN-Eu on Cu^{2+} was performed under the same optimized condition as the fluorescence approach. The feasibility experiments have demonstrated that the number of SPN-Eu detected during the spICP-MS data collection period (180s) was decreased as the amount of nanoparticle aggregation enhanced. Therefore, in order to build the relationship with Cu^{2+} concentration, the aggregation level was defined as φ in the following equation 1.

$$\varphi = 1 - \frac{\text{Number of SPN~Eu detected after mixed with } \text{Cu}^{2+}(E)}{\text{Number of SPN~Eu detected before mixed with } \text{Cu}^{2+}(E_0)}$$

Eq 1

In Figure 40, the raw spICP-MS data showed a decreased number of individual spikes in a wide Cu^{2+} detection dynamic range covering from 1.0×10^{-3} nM to 1.0×10^5 nM. In Figure 41, SPN-Eu (1.0 ppm) was reacted with different concentrations of Cu^{2+}

(0, 0.001, 0.01, 0.1, 1, 10, 100, 1,000, 10,000, 100,000 nM) at the optimized condition. The aggregation level showed an acceptable regression equation of $\varphi = 0.08327\text{Log}[\text{Cu}^{2+}] + 0.3289$ for Cu^{2+} with a correlation coefficient of 0.9944. (Figure 41) The limit of detection (LOD) for Cu^{2+} was calculated to be 0.42 pM based on the slope of the equation ($3\sigma/s$), where σ was the standard deviation of three blank φ values, and s was the slope of the calibration curve. In conclusion, this method showed a broad linear range and a low limit of detection value for Cu^{2+} .

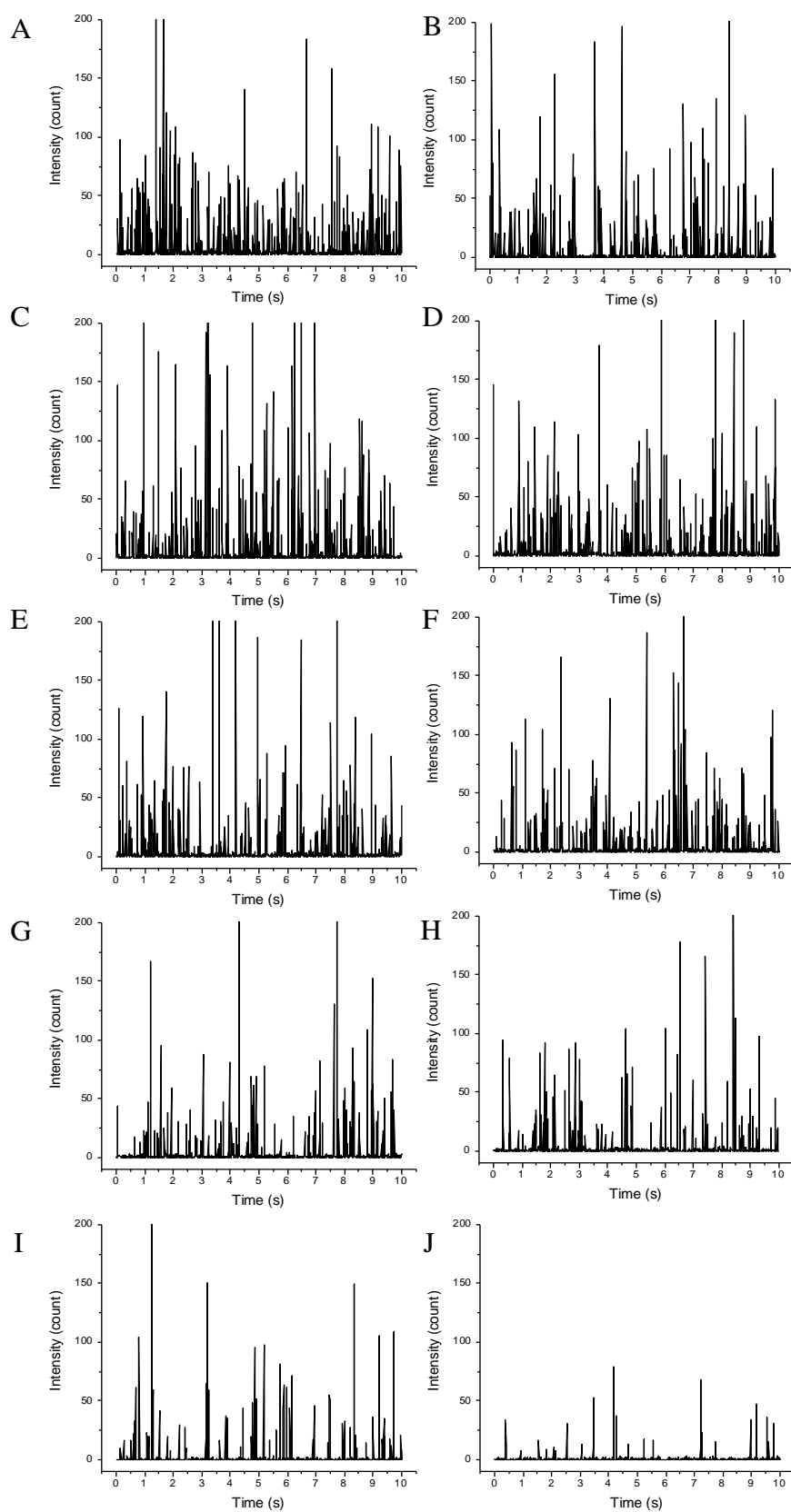


Figure 40. spICP-MS spectra of SPN-Eu in the presence of different concentrations of

Cu^{2+} (A to J: 0, 0.001, 0.1, 1, 10, 100, 1000, 10000, 100000 nM). Incubation at 25 °C for 60 min in HEPES buffer(20 mM, pH 7.0). Dilution to 1.0×10^4 particles/mL and injecting into spICP-MS(^{153}Eu , dwell time: 10 ms)

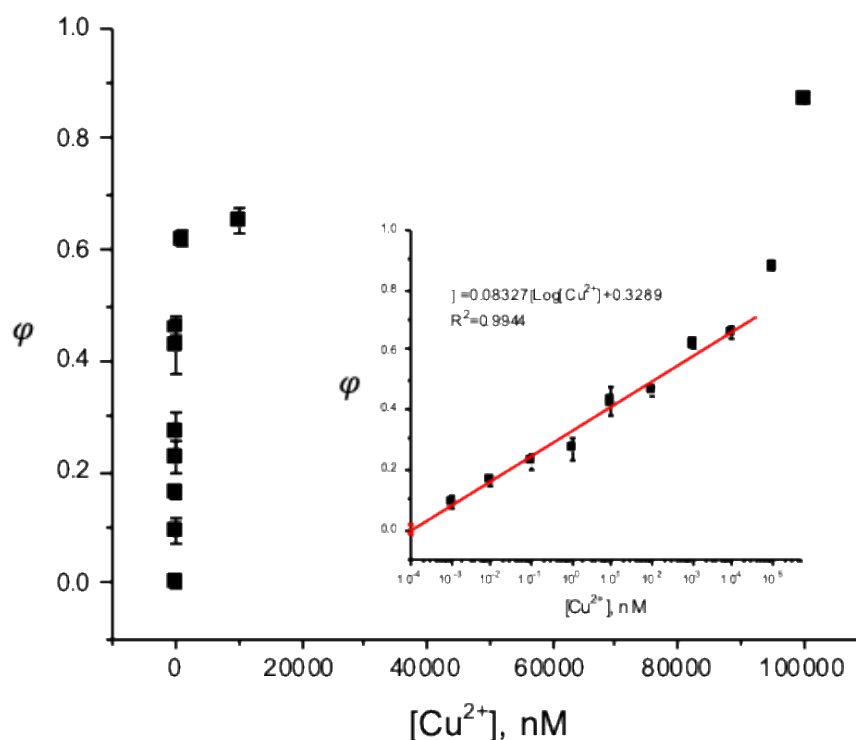


Figure 41. Selectivity of the SPN-Eu probe for Cu^{2+} detection by spICP-MS. Cu^{2+} and some other ions' concentrations: 1 μM .

3.8. Selectivity of SPN-Eu on Cu^{2+} by spICP-MS

The selectivity of the SPN-Eu probe for Cu^{2+} was studied using the spICP-MS assay. SPN-Eu solution was mixed with other relevant metal ions which might be existing in the natural environment. A series of metal ions was evaluated including Ni^{2+} , Co^{2+} , Fe^{2+} , Fe^{3+} , Pb^{2+} , Mg^{2+} , Cd^{2+} , Ag^+ , Zn^{2+} , Al^{3+} , Mn^{2+} , and Cu^{2+} at a concentration of 1 μM . The results are shown in Figure 40. The aggregation level ϕ on Cu^{2+} was higher than the other monovalent, bivalent and trivalent metal ions. Fe^{3+} , and Fe^{2+} showed slight aggregation. However, their value of E/E_0 was larger than 80%, which exhibited a significant difference compared with Cu^{2+} .

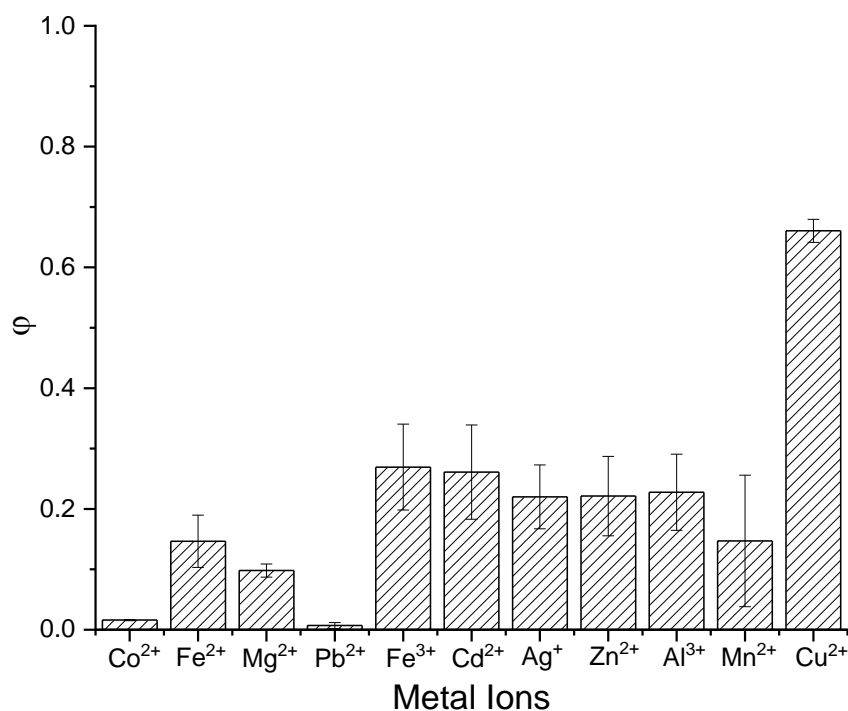


Figure 42. Selectivity of the SPN-Eu probe for Cu²⁺ detection by spICP-MS. Cu²⁺ and some other ions' concentrations: 1 μM.

3.9. Analysis of the spiked samples

To test the applicability of this Eu-SPN approach for Cu²⁺ detection, river water samples were spiked with two different levels of Cu²⁺ (10 μM and 100 nM), followed by detecting with both fluorescence signal and spICP-MS signal.

Both fluorescence and spICP-MS detection were performed. The spike recovery results are compared with the standard traditional ICP-MS method in Table 5. The higher concentration (10 μM) was in the linear range of the fluorometric method, the result detected by the fluorometric method showed a correspondent value with ICP-MS method. The lower concentration was in the linear range of spICP-MS method. Both of the results tested by the spICP-MS method and fluorometric method exhibited acceptable recoveries (100 ± 20%).

Table 5. Spike recovery level of spICP-MS and fluorometric methods for Cu²⁺ detection in river water (n=3).

Methods	Samples	Spiked (μM)	Detected (μM)	Recovery of this method (%)
ICP-MS	River water (Red river)	10	10.28 \pm 1.78	103 \pm 17.8
Eu-SPN FL Signal	River water (Red river)	10	8.34 \pm 0.07	83.4 \pm 0.72

Methods	Samples	Spiked (nM)	Detected (nM)	Recovery of this method (%)
ICP-MS	River water (Red river)	100	89 \pm 0.56	89 \pm 0.56
Eu-SPN spICP-MS Signal	River water (Red river)	100	114.75 \pm 23.35	114.75 \pm 23.35

4. Conclusions

In this chapter we developed a two-readout nanoprobe for Cu²⁺ detection by Eu³⁺ doped MEH-PPV semiconducting polymer nanoparticles. The strong chelating interactions between carboxylic groups and Cu²⁺ induced the aggregation, which could be analyzed by both fluorescence and spICP-MS signal. This method has substantially enhanced the sensitivity and reduced limit of detection for copper detection. The spICP-MS method showed a broad logarithmic range of 0.001 nM to 100,00 nM with a limit of detection of 0.42 pM. In contrast, the fluorescence method showed a linear range of 2 μM to 50 μM with a limit of detection of 0.29 μM . The developed probe was successfully used for Cu²⁺ detection in river water with acceptable recovery results.

REFERENCES

1. Poutahidis, T.; Varian, B. J.; Levkovich, T.; Lakritz, J. R.; Mirabal, S.; Kwok, C.; Ibrahim, Y. M.; Kearney, S. M.; Chatzigiagkos, A.; Alm, E. J.; Erdman, S. E., Dietary Microbes Modulate Transgenerational Cancer Risk. *Cancer Res.* **2015**, *75*, 1197-1204.
2. Lukianova-Hleb Ekaterina, Y.; Ren, X.; Zasadzinski Joseph, A.; Wu, X.; Lapotko Dmitri, O., Plasmonic Nanobubbles Enhance Efficacy and Selectivity of Chemotherapy Against Drug-Resistant Cancer Cells. *Adv. Mater.* **2012**, *24*, 3831–3837.
3. Danhier, F.; Feron, O.; Préat, V., To Exploit the Tumor Microenvironment: Passive and Active Tumor Targeting of Nanocarriers for Anti-cancer Drug Delivery. *J. Control. Release* **2010**, *148*, 135–146.
4. Bae, Y. H.; Park, K., Targeted Drug Delivery to Tumors: Myths, Reality and Possibility. *J. Control. Release* **2011**, *153*, 198–205.
5. Theato, P.; Sumerlin, B. S.; O'Reilly, R. K.; Epps, I. I. I. T. H., Stimuli Responsive Materials. *Chem. Soc. Rev.* **2013**, *42*, 7055–7056.
6. Wang, H.; Zhao, S.; Agarwal, P.; Dumbleton, J.; Yu, J.; Lu, X.; He, X., Multi-layered Polymeric Nanoparticles for pH-responsive and Sequenced Release of Theranostic Agents. *Chem. Comm.* **2015**, *51*, 7733–7736.
7. Dai, Y.; Ma, P. a.; Cheng, Z.; Kang, X.; Zhang, X.; Hou, Z.; Li, C.; Yang, D.; Zhai, X.; Lin, J., Up-Conversion Cell Imaging and pH-Induced Thermally Controlled Drug Release from NaYF₄:Yb³⁺/Er³⁺@Hydrogel Core–Shell Hybrid Microspheres. *ACS Nano* **2012**, *6*, 3327–3338.
8. Brannon-Peppas, L.; Blanchette, J. O., Nanoparticle and Targeted Systems for Cancer Therapy. *Adv. Drug Deliv. Rev.* **2004**, *56*, 1649–1659.
9. Mitragotri, S.; Lahann, J., Materials for Drug Delivery: Innovative Solutions to Address Complex Biological Hurdles. *Adv. Mater.* **2012**, *24*, 3717–3723.
10. Gao, W.; Chan, J. M.; Farokhzad, O. C., pH-Responsive Nanoparticles for Drug Delivery. *Mol. Pharm.* **2010**, *7*, 1913–1920.
11. Estrella, V.; Chen, T.; Lloyd, M.; Wojtkowiak, J.; Cornell, H. H.; Ibrahim-Hashim, A.; Bailey, K.; Balagurunathan, Y.; Rothberg, J. M.; Sloane, B. F.; Johnson, J.; Gatenby,

R. A.; Gillies, R. J., Acidity Generated by The Tumor Microenvironment Drives Local Invasion. *Cancer Res.* **2013**, *73*, 1524–1535.

12. Kato, Y.; Ozawa, S.; Miyamoto, C.; Maehata, Y.; Suzuki, A.; Maeda, T.; Baba, Y., Acidic Extracellular Microenvironment and Cancer. *Cancer Cell Int.* **2013**, *13*, 89–89.

13. Zheng, Y.; Wang, L.; Lu, L.; Wang, Q.; Benicewicz, B. C., pH and Thermal Dual-Responsive Nanoparticles for Controlled Drug Delivery with High Loading Content. *ACS Omega* **2017**, *2*, 3399–3405.

14. Esfand, R.; Tomalia, Poly(amidoamine) (PAMAM) Dendrimers: from Biomimicry to Drug Delivery and Biomedical Applications. D. A., *Drug Discov. Today* **2001**, *6*, 427–436.

15. Hu, H.; Zhang, X.; Sun, J.; An, L.; Du, J.; Yang, H.; Li, F.; Wu, H.; Yang, S., Preparation of pH-Responsive Hollow Poly(MAA-co-EGDMA) Nanocapsules for Drug Delivery and Ultrasound Imaging. *RSC Advances* **2016**, *6*, 103754–103762.

16. Dergunov, S. A.; Durbin, J.; Pattanaik, S.; Pinkhassik, E., pH-Mediated Catch and Release of Charged Molecules with Porous Hollow Nanocapsules. *J. Am. Chem. Soc.* **2014**, *136*, 2212–2215.

17. Pan, A. C.; Borhani, D. W.; Dror, R. O.; Shaw, D. E., Molecular Determinants of Drug–receptor Binding Kinetics. *Drug Discov. Today* **2013**, *18*, 667–673.

18. Pascu, S. I.; Arrowsmith, R. L.; Bayly, S. R.; Brayshaw, S.; Hu, Z., Towards Nanomedicines: Design Protocols to Assemble, Visualize and Test Carbon Nanotube Probes for Multi-modality Biomedical Imaging. *Philos. Trans. Royal Soc. A* **2010**, *368*, 3683–3712.

19. Hans, M. L.; Lowman, A. M., Biodegradable Nanoparticles for Drug Delivery and Targeting. *Curr. Opin. Solid State Mater. Sci.* **2002**, *6*, 319–327.

20. Pistolis, G.; Malliaris, A.; Tsiourvas, D.; Paleos, C. M., Poly(propyleneimine) Dendrimers as pH-Sensitive Controlled-Release Systems. *Chem.: Eur. J.* **1999**, *5*, 1440–1444.

21. Yatvin, M. B.; Kreutz, W.; Horwitz, B. A.; Shinitzky, M., pH-sensitive Liposomes: Possible Clinical Implications. *Science* **1980**, *210*, 1253–1255.

22. Gujrati, M.; Vaidya, A.; Lu, Z.-R., Multifunctional pH-Sensitive Amino Lipids for siRNA Delivery. *Bioconjugate Chem.* **2016**, *27*, 19–35.

23. Nam, J.; La, W.-G.; Hwang, S.; Ha, Y. S.; Park, N.; Won, N.; Jung, S.; Bhang, S. H.; Ma, Y.-J.; Cho, Y.-M.; Jin, M.; Han, J.; Shin, J.-Y.; Wang, E. K.; Kim, S. G.; Cho, S.-H.; Yoo, J.; Kim, B.-S.; Kim, S., pH-Responsive Assembly of Gold Nanoparticles and “Spatiotemporally Concerted” Drug Release for Synergistic Cancer Therapy. *ACS Nano* **2013**, *7*, 3388–3402.
24. He, Q.; Gao, Y.; Zhang, L.; Zhang, Z.; Gao, F.; Ji, X.; Li, Y.; Shi, J., A pH-responsive Mesoporous Silica Nanoparticles-based Multi-drug Delivery System for Overcoming Multi-drug Resistance. *Biomaterials* **2011**, *32*, 7711–7720.
25. Bharti, C.; Nagaich, U.; Pal, A. K.; Gulati, N., Mesoporous Silica Nanoparticles in Target Drug Delivery System: A review. *Int. J. Pharm. Investig.* **2015**, *5*, 124–133.
26. Karimi, M.; Ghasemi, A.; Sahandi Zangabad, P.; Rahighi, R.; Moosavi Basri, S. M.; Mirshekari, H.; Amiri, M.; Shafaei Pishabad, Z.; Aslani, A.; Bozorgomid, M.; Ghosh, D.; Beyzavi, A.; Vaseghi, A.; Aref, A. R.; Haghani, L.; Bahrami, S.; Hamblin, M. R., Smart Micro/Nanoparticles in Stimulus-Responsive Drug/Gene Delivery Systems. *Chem. Soc. Rev.* **2016**, *45*, 1457–1501.
27. Manzano, M.; Vallet-Regi, M., New Developments in Ordered Mesoporous Materials for Drug Delivery. *J. Mater. Chem.* **2010**, *20*, 5593–5604.
28. Yang, P.; Gai, S.; Lin, J., Functionalized Mesoporous Silica Materials for Controlled Drug Delivery. *Chem. Soc. Rev.* **2012**, *41*, 3679–3698.
29. Pan, L.; He, Q.; Liu, J.; Chen, Y.; Ma, M.; Zhang, L.; Shi, J., Nuclear-Targeted Drug Delivery of TAT Peptide-Conjugated Monodisperse Mesoporous Silica Nanoparticles. *J. Am. Chem. Soc.* **2012**, *134*, 5722–5725.
30. Kwon, S.; Singh, R. K.; Perez, R. A.; Abou Neel, E. A.; Kim, H.-W.; Chrzanowski, W., Silica-based Mesoporous Nanoparticles for Controlled Drug Delivery. *J. Tissue Eng.* **2013**, *4*, 2041731413503357.
31. Watermann, A.; Brieger, J., Mesoporous Silica Nanoparticles as Drug Delivery Vehicles in Cancer. *Nanomaterials* **2017**, *7*, 189.
32. Hao, X.; Hu, X.; Zhang, C.; Chen, S.; Li, Z.; Yang, X.; Liu, H.; Jia, G.; Liu, D.; Ge, K.; Liang, X.-J.; Zhang, J., Hybrid Mesoporous Silica-Based Drug Carrier Nanostructures with Improved Degradability by Hydroxyapatite. *ACS Nano* **2015**, *9*, 9614–9625.
33. Yuan, L.; Tang, Q.; Yang, D.; Zhang, J. Z.; Zhang, F.; Hu, J., Preparation of pH-Responsive Mesoporous Silica Nanoparticles and Their Application in Controlled Drug Delivery. *J. Phys. Chem. C* **2011**, *115*, 9926–9932.

34. Zhang, G.; Yang, M.; Cai, D.; Zheng, K.; Zhang, X.; Wu, L.; Wu, Z., Composite of Functional Mesoporous Silica and DNA: An Enzyme-Responsive Controlled Release Drug Carrier System. *ACS Appl. Mater. Interfaces* **2014**, *6*, 8042–8047.
35. Fan, W.; Yung, B.; Huang, P.; Chen, X., Nanotechnology for Multimodal Synergistic Cancer Therapy. *Chem. Rev.* **2017**, *117*, 13566-13638.
36. Zhao, Z. X.; Huang, Y. Z.; Shi, S. G.; Tang, S. H.; Li, D. H.; Chen, X. L., Cancer Therapy Improvement with Mesoporous Silica Nanoparticles Combining Photodynamic and Photothermal Therapy. *Nanotechnology* **2014**, *25*, 285701.
37. Yao, X.; Tian, Z.; Liu, J.; Zhu, Y.; Hanagata, N., Mesoporous Silica Nanoparticles Capped with Graphene Quantum Dots for Potential Chemo–Photothermal Synergistic Cancer Therapy. *Langmuir* **2017**, *33*, 591–599.
38. Hong, E. J.; Choi, D. G.; Shim, M. S., Targeted and Effective Photodynamic Therapy for Cancer Using Functionalized Nanomaterials. *Acta Pharm. Sin. B* **2016**, *6*, 297–307.
39. Huang, X.; El-Sayed, I. H.; Qian, W.; El-Sayed, M. A., Cancer Cell Imaging and Photothermal Therapy in the Near-Infrared Region by Using Gold Nanorods. *J. Am. Chem. Soc.* **2006**, *128*, 2115–2120.
40. Zhang, Z.; Wang, J.; Nie, X.; Wen, T.; Ji, Y.; Wu, X.; Zhao, Y.; Chen, C., Near Infrared Laser-Induced Targeted Cancer Therapy Using Thermoresponsive Polymer Encapsulated Gold Nanorods. *J. Am. Chem. Soc.* **2014**, *136*, 7317–7326.
41. Robinson, J. T.; Tabakman, S. M.; Liang, Y.; Wang, H.; Sanchez Casalongue, H.; Vinh, D.; Dai, H., Ultrasmall Reduced Graphene Oxide with High Near-Infrared Absorbance for Photothermal Therapy. *J. Am. Chem. Soc.* **2011**, *133*, 6825–6831.
42. Zhang, W.; Guo, Z.; Huang, D.; Liu, Z.; Guo, X.; Zhong, H., Synergistic Effect of Chemo-photothermal Therapy Using PEGylated Graphene Oxide. *Biomaterials* **2011**, *32*, 8555–8561.
43. Cheon, Y. A.; Bae, J. H.; Chung, B. G., Reduced Graphene Oxide Nanosheet for Chemo-photothermal Therapy. *Langmuir* **2016**, *32*, 2731–2736.
44. Kang, S.; Lee, J.; Ryu, S.; Kwon, Y.; Kim, K.-H.; Jeong, D. H.; Paik, S. R.; Kim, B.-S., Gold Nanoparticle/Graphene Oxide Hybrid Sheets Attached on Mesenchymal Stem Cells for Effective Photothermal Cancer Therapy. *Chem. Mater.* **2017**, *29*, 3461–3476.
45. Wang, D.; Duan, H.; Lu, J.; Lu, C., Fabrication of Thermo-responsive Polymer Functionalized Reduced Graphene Oxide@Fe₃O₄@Au Magnetic Nanocomposites for Enhanced Catalytic Applications. *J. Mater. Chem. A* **2017**, *5*, 5088–5097.
46. Wang, W.; Ye, Y.; Li, J.; Li, X.; Zhou, X.; Tan, D.; Jin, Y.; Wu, E.; Cui, Q.; Wu, M., Lyn Regulates Cytotoxicity in Respiratory Epithelial Cells Challenged by Cigarette Smoke Extracts. *Curr. Mol. Med.* **2014**, *14*, 663–672.

47. Yuan, K.; Xie, K.; Fox, J.; Zeng, H.; Gao, H.; Huang, C.; Wu, M., Decreased Levels of miR-224 and the Passenger Strand of miR-221 Increase MBD2, Suppressing Maspin and Promoting Colorectal Tumor Growth and Metastasis in Mice. *Gastroenterology* **2013**, *145*, 853–864.
48. Goenka, S.; Sant, V.; Sant, S., Cancer Therapy Graphene-based Nanomaterials for Drug Delivery and Tissue Engineering. *J. Control. Release* **2014**, *173*, 75–88.
49. Georgakilas, V.; Otyepka, M.; Bourlinos, A. B.; Chandra, V.; Kim, N.; Kemp, K. C.; Hobza, P.; Zboril, R.; Kim, K. S., Functionalization of Graphene: Covalent and Non-Covalent Approaches, Derivatives and Applications. *Chem. Rev.* **2012**, *112*, 6156–6214.
50. Na, Y. I.; Song, Y. I.; Kim, S. W.; Suh, S. J., Study on Properties of Eco-friendly Reduction Agents for the Reduced Graphene Oxide Method. *Carbon lett.* **2017**, *24*, 1–9.
51. Wang, R.; Wang, Y.; Xu, C.; Sun, J.; Gao, L., Facile One-step Hydrazine-assisted Solvothermal Synthesis of Nitrogen-doped Reduced Graphene Oxide: Reduction Effect and Mechanisms. *RSC Adv.* **2013**, *3*, 1194–1200.
52. Muhammad, F.; Guo, M.; Qi, W.; Sun, F.; Wang, A.; Guo, Y.; Zhu, G., pH-Triggered Controlled Drug Release from Mesoporous Silica Nanoparticles via Intracellular Dissolution of ZnO Nanolids. *J. Am. Chem. Soc.* **2011**, *133*, 8778–8781.
53. AlOthman, Z., A Review: Fundamental Aspects of Silicate Mesoporous Materials. *Materials* **2012**, *5*, 2874.
54. Cauda, V.; Schlossbauer, A.; Bein, T., Bio-Degradation Study of Colloidal Mesoporous Silica Nanoparticles: Effect of Surface Functionalization with Organo-Silanes and Poly(Ethylene Glycol). *Micropor. Mesopor. Mat.* **2010**, *132*, 60–71.
55. Smith, L.; Watson, M. B.; O’Kane, S. L.; Drew, P. J.; Lind, M. J.; Cawkwell, L., The Analysis of Doxorubicin Resistance in Human Breast Cancer Cells Using Antibody Microarrays. *Mol. Canc. Ther.* **2006**, *5*, 2115–2120.
56. Shen, Z.; Shen, T.; Wientjes, M. G.; O’Donnell, M. A.; Au, J. L. S., Intravesical Treatments of Bladder Cancer: Review. *Pharm. Res.* **2008**, *25*, 1500–1510.
57. Wang, S.-L.; Lee, J.-J.; Liao, A. T., Comparison of Efficacy and Toxicity of Doxorubicin and Mitoxantrone in Combination Chemotherapy for Canine Lymphoma. *Can. Vet. J.* **2016**, *57*, 271–276.
58. Thorn, C. F.; Oshiro, C.; Marsh, S.; Hernandez-Boussard, T.; McLeod, H.; Klein, T. E.; Altman, R. B., Doxorubicin Pathways: Pharmacodynamics and Adverse Effects. *Pharmacogenet. and Genomics* **2011**, *21*, 440–446.

59. Mason, P. A.; Cox, L. S., The Role of DNA Exonucleases in Protecting Genome Stability and Their Impact on Ageing. *Age(dordr)*. **2012**, *34*, 1317-1340.
60. Rogers, S. G.; Weiss, B., [26] Exonuclease III of Escherichia Coli K-12, an AP Endonuclease. In *Methods in Enzymology*, Academic Press: 1980; Vol. 65, pp 201-211.
61. Souza, L. L.; Eduardo, I. R.; Pádula, M.; Leitão, A. C., Endonuclease IV and Exonuclease III are Involved in the Repair and Mutagenesis of DNA Lesions Induced by UVB in Escherichia Coli. *Mutagenesis* **2006**, *21*, 125-130.
62. Fijalkowska, I. J.; Schaaper, R. M., Mutants in the Exo I Motif of Escherichia Coli dnaQ: Defective Proofreading and Inviability Due to Error Catastrophe. *Proc. Natl. Acad. Sci. U.S.A.* **1996**, *93*, 2856-2861.
63. Paull, T. T.; Gellert, M., The 3' to 5' Exonuclease Activity of Mre11 Facilitates Repair of DNA Double-Strand Breaks. *Mol. Cell* **1998**, *1*, 969-979.
64. Whitaker, A. M.; Flynn, T. S.; Freudenthal, B. D., Molecular Snapshots of APE1 Proofreading Mismatches and Removing DNA Damage. *Nat. Commun.* **2018**, *9*, 399.
65. Chen, Y.-C.; Li, C.-L.; Hsiao, Y.-Y.; Duh, Y.; Yuan, H. S., Structure and Function of TatD Exonuclease in DNA Repair. *Nucleic. Acids. Res.* **2014**, *42*, 10776-10785.
66. Shevelev, I. V.; Hübscher, U., The 3'-5' Exonucleases. *Nat. Rev. Mol. Cell Biol.* **2002**, *3*, 364-376.
67. Kavanagh, D.; Spitzer, D.; Kothari, P.; Shaikh, A.; Liszewski, M. K.; Richards, A.; Atkinson, J. P., New Roles for the Major Human 3'-5' Exonuclease TREX1 in Human Disease. *Cell Cycle* **2008**, *7*, 1718-1725.
68. Wang, C.-J.; Lam, W.; Bussom, S.; Chang, H.-M.; Cheng, Y.-C., TREX1 Acts in Degrading Damaged DNA from Drug-treated Tumor Cells. *DNA Repair* **2009**, *8*, 1179-1189.
69. Brucet, M.; Querol-Audí, J.; Bertlik, K.; Lloberas, J.; Fita, I.; Celada, A., Structural and Biochemical Studies of TREX1 Inhibition by Metals. Identification of a New Active Histidine Conserved in DEDDh Exonucleases. *Protein. Sci.* **2009**, *17*, 2059-2069.
70. Nimonkar, A. V.; Ozsoy, A. Z.; Genschel, J.; Modrich, P.; Kowalczykowski, S. C., Human Exonuclease 1 and BLM Helicase Interact to Resect DNA and Initiate DNA repair. *Proc. Natl. Acad. Sci. U.S.A.* **2008**, *105*, 16906-16911.
71. Lehtinen, D. A.; Harvey, S.; Mulcahy, M. J.; Hollis, T.; Perrino, F. W., The TREX1

Double-stranded DNA Degradation Activity Is Defective in Dominant Mutations Associated with Autoimmune Disease. *J. Biol. Chem.* **2008**, *283*, 31649-31656.

72. Lee, J.; Min, D.-H., A Simple Fluorometric Assay for DNA Exonuclease Activity based on Graphene Oxide. *Analyst* **2012**, *137*, 2024-2026.

73. Zou, P.; Liu, Y.; Wang, H.; Wu, J.; Zhu, F.; Wu, H., G-quadruplex DNAzyme-based Chemiluminescence Biosensing Platform based on Dual Signal Amplification for Label-free and Sensitive Detection of Protein. *Biosens. Bioelectron.* **2016**, *79*, 29-33.

74. Dai, N.; Kool, E. T., Fluorescent DNA-based Enzyme Sensors. *Chem. Soc. Rev.* **2011**, *40*, 5756-5770.

75. Yang, W.; Ruan, Y.; Wu, W.; Chen, P.; Xu, L.; Fu, F., A "Turn-on" and Label-free Fluorescent Assay for the Rapid Detection of Exonuclease III Activity based on Tb(III)-induced G-quadruplex Conjugates. *Anal. Bioanal. Chem.* **2014**, *406*, 4535-4540.

76. Xu, Q.; Zhang, Y.; Zhang, C.-y., A Triple-color Fluorescent Probe for Multiple Nuclease Assays. *Chem. Commun.* **2015**, *51*, 9121-9124.

77. Wu, X.; Chen, J.; Zhao, J. X., Ultrasensitive Detection of 3'-5' Exonuclease Enzymatic Activity Using Molecular Beacons. *Analyst* **2014**, *139*, 1081-1087.

78. Wang, Y.; Li, Z.; Wang, J.; Li, J.; Lin, Y., Graphene and Graphene Oxide: Biofunctionalization and Applications in Biotechnology. *Trends Biotechnol.* **2011**, *29*, 205-212.

79. Zhu, Y.; Murali, S.; Cai, W.; Li, X.; Suk, J. W.; Potts, J. R.; Ruoff, R. S., Graphene and Graphene Oxide: Synthesis, Properties, and Applications. *Adv. Mater.* **2010**, *22*, 3906-3924.

80. Singh, R. K.; Kumar, R.; Singh, D. P., Graphene Oxide: Strategies for Synthesis, Reduction and Frontier Applications. *RSC Adv.* **2016**, *6*, 64993-65011.

81. Liu, F.; Choi, J. Y.; Seo, T. S., Graphene Oxide Arrays for Detecting Specific DNA Hybridization by Fluorescence Resonance Energy Transfer. *Biosens. Bioelectron.* **2010**, *25*, 2361-2365.

82. Morales-Narváez, E.; Merkoçi, A., Graphene Oxide as an Optical Biosensing Platform. *Adv. Mater.* **2012**, *24*, 3298-3308.

83. Liu, Y.; Liu, C.-y.; Liu, Y., Investigation on Fluorescence Quenching of dyes by Graphite Oxide and Graphene. *Appl. Surf. Sci.* **2011**, *257*, 5513-5518.

84. Kasry, A.; Ardakani, A. A.; Tulevski, G. S.; Menges, B.; Copel, M.; Vyklicky, L., Highly Efficient Fluorescence Quenching with Graphene. *J. Phys. Chem. C* **2012**, *116*, 2858-2862.
85. Dong, H.; Gao, W.; Yan, F.; Ji, H.; Ju, H., Fluorescence Resonance Energy Transfer between Quantum Dots and Graphene Oxide for Sensing Biomolecules *Anal. Chem.* **2010**, *82*, 5511-5517.
86. Liu, C.; Wang, Z.; Jia, H.; Li, Z., Efficient Fluorescence Resonance Energy Transfer between Upconversion Nanophosphors and Graphene Oxide: A Highly Sensitive Biosensing Platform. *Chem. Commun.* **2011**, *47*, 4661-4663.
87. Shi, J.; Guo, J.; Bai, G.; Chan, C.; Liu, X.; Ye, W.; Hao, J.; Chen, S.; Yang, M., A Graphene Oxide based Fluorescence Resonance Energy Transfer (FRET) Biosensor for Ultrasensitive Detection of Botulinum Neurotoxin A (BoNT/A) Enzymatic Activity. *Biosens. Bioelectron.* **2015**, *65*, 238-244.
88. Li, S.; Aphale, A. N.; Macwan, I. G.; Patra, P. K.; Gonzalez, W. G.; Miksovska, J.; Leblanc, R. M., Graphene Oxide as a Quencher for Fluorescent Assay of Amino Acids, Peptides, and Proteins. *ACS Appl. Mater. Interfaces* **2012**, *4*, 7069-7075.
89. Li, F.; Feng, Y.; Zhao, C.; Li, P.; Tang, B., A Sensitive Graphene Oxide–DNA based Sensing Platform for Fluorescence “Turn-on” Detection of Bleomycin. *Chem. Commun.* **2012**, *48*, 127-129.
90. Wu, X.; Xing, Y.; Zeng, K.; Huber, K.; Zhao, J. X., Study of Fluorescence Quenching Ability of Graphene Oxide with a Layer of Rigid and Tunable Silica Spacer. *Langmuir* **2018**, *34*, 603-611.
91. Zhang, H.; Lin, Z.; Su, X., Label-free Detection of Exonuclease III by Using dsDNA-templated Copper Nanoparticles as Fluorescent Probe. *Talanta* **2015**, *131*, 59-63.
92. Xu, M.; Li, B., Label-free Fluorescence Strategy for Sensitive Detection of Exonuclease Activity Using SYBR Green I as Probe. *Spectrochim. Acta A Mol. Biomol. Spectrosc.* **2015**, *151*, 22-26.
93. Lehman, I. R.; Nussbaum, A. L., The Deoxyribonucleases of Escherichia coli : V. ON THE SPECIFICITY OF EXONUCLEASE I (PHOSPHODIESTERASE). *J. Biol. Chem.* **1964**, *239*, 2628-2636.
94. Mitsis, P. G.; Kwagh, J. G., Characterization of the Interaction of Lambda Exonuclease with the Ends of DNA. *Nucleic. Acids. Res.* **1999**, *27*, 3057-3063.

95. Lovett, S. T.; Kolodner, R. D., Identification and Purification of a Single-Stranded-DNA-Specific Exonuclease Encoded by the RecJ Gene of Escherichia Coli. *Proc. Natl. Acad. Sci. U.S.A.* **1989**, *86*, 2627-2631.
96. Richardson, C. C., 16 Bacteriophage T4 Polynucleotide Kinase. In *The Enzymes*; Boyer, P. D., Ed. Academic Press: 1981; Vol. 14, pp 299-314.
97. Green, Michael R; Sambrook, J., In *Molecular Cloning: A Laboratory Manual, 4th Ed.*; Cold Spring Harbor Laboratory Press: 1980; Vol. 2, p 1009.
98. Lindahl, T.; Ljungquist, S.; Siegert, W.; Nyberg, B.; Sperens, B., DNA N-Glycosidases: Properties of Uracil-DNA Glycosidase from Escherichia Coli. *J. Biol. Chem.* **1977**, *252*, 3286-3294.
99. Silva-Portela, R. C. B.; Carvalho, F. M.; Pereira, C. P. M.; de Souza-Pinto, N. C.; Modesti, M.; Fuchs, R. P.; Agnez-Lima, L. F., ExoMeg1: A New Exonuclease from Metagenomic Library. *Sci. Rep.* **2016**, *6*, 19712-19712.
100. Zhu, C.; Yang, G.; Li, H.; Du, D.; Lin, Y., Electrochemical Sensors and Biosensors Based on Nanomaterials and Nanostructures. *Anal. Chem.* **2015**, *87*, 230-49.
101. Hong, G.; Diao, S.; Antaris, A. L.; Dai, H., Carbon Nanomaterials for Biological Imaging and Nanomedicinal Therapy. *Chem. Rev.* **2015**, *115*, 10816-10906.
102. Liang, H.; Zhang, X.-B.; Lv, Y.; Gong, L.; Wang, R.; Zhu, X.; Yang, R.; Tan, W., Functional DNA-Containing Nanomaterials: Cellular Applications in Biosensing, Imaging, and Targeted Therapy. *Acc. Chem. Res.* **2014**, *47*, 1891-1901.
103. Chen, J.; Wu, X.; Hou, X.; Su, X.; Chu, Q.; Fahrudin, N.; Zhao, J. X., Shape-Tunable Hollow Silica Nanomaterials Based on a Soft-Templating Method and Their Application as a Drug Carrier. *ACS appl. mater. int.* **2014**, *6*, 21921-30.
104. Kimmel, D. W.; LeBlanc, G.; Meschievitz, M. E.; Cliffel, D. E., Electrochemical Sensors and Biosensors *Anal. Chem.* **2012**, *84*, 685-707.
105. Shi, J.; Votruba, A. R.; Farokhzad, O. C.; Langer, R., Nanotechnology in Drug Delivery and Tissue Engineering: From Discovery to Applications. *Nano lett.* **2010**, *10*, 3223-30.
106. Blum, A. P.; Kammeyer, J. K.; Rush, A. M.; Callmann, C. E.; Hahn, M. E.; Gianneschi, N. C., Stimuli-Responsive Nanomaterials for Biomedical Applications. *J. Am. Chem. Soc.* **2015**, *137*, 2140-2154.

107. Taylor-Pashow, K. M. L.; Della Rocca, J.; Huxford, R. C.; Lin, W., Hybrid Nanomaterials for Biomedical Applications. *Chem. Commun.* **2010**, *46*, 5832-5849.
108. Wang, J.; Ma, Q.; Wang, Y.; Shen, H.; Yuan, Q., Recent Progress in Biomedical Applications of Persistent Luminescence Nanoparticles. *Nanoscale* **2017**, *9*, 6204-6218.
109. Mader, H. S.; Kele, P.; Saleh, S. M.; Wolfbeis, O. S., Upconverting Luminescent Nanoparticles for Use in Bioconjugation and Bioimaging. *Curr. Opin. Chem. Biol.* **2010**, *14*, 582-596.
110. Zhou, C.; Yang, S.; Liu, J.; Yu, M.; Zheng, J., Luminescent Gold Nanoparticles: A New Class of Nanoprobes for Biomedical Imaging. *Exp. Biol. Med.* **2013**, *238*, 1199-1209.
111. Wang, F.; Tan, W. B.; Zhang, Y.; Fan, X.; Wang, M., Luminescent Nanomaterials for Biological Labelling. *Nanotechnol.* **2005**, *17*, R1-R13.
112. Wang, R.; Zhang, F., NIR Luminescent Nanomaterials for Biomedical Imaging. *J. Mater. Chem. B* **2014**, *2*, 2422-2443.
113. Feldmann, C., Luminescent Nanomaterials. *Nanoscale* **2011**, *3*, 1947-1948.
114. Yao, C.; Yao, C.; Tong, Y., Lanthanide Ion-based Luminescent Nanomaterials for Bioimaging. *Trends Anal. Chem.* **2012**, *39*, 60-71.
115. Lin, C.-A. J.; Yang, T.-Y.; Lee, C.-H.; Huang, S. H.; Sperling, R. A.; Zanella, M.; Li, J. K.; Shen, J.-L.; Wang, H.-H.; Yeh, H.-I.; Parak, W. J.; Chang, W. H., Synthesis, Characterization, and Bioconjugation of Fluorescent Gold Nanoclusters toward Biological Labeling Applications. *ACS Nano* **2009**, *3*, 395-401.
116. Zhang, M.; Bai, L.; Shang, W.; Xie, W.; Ma, H.; Fu, Y.; Fang, D.; Sun, H.; Fan, L.; Han, M.; Liu, C.; Yang, S., Facile Synthesis of Water-soluble, Highly Fluorescent Graphene Quantum Dots as A Robust Biological Label for Stem Cells. *J. Mater. Chem.* **2012**, *22*, 7461-7467.
117. Feng, J.; Shan, G.; Maquieira, A.; Koivunen, M. E.; Guo, B.; Hammock, B. D.; Kennedy, I. M., Functionalized Europium Oxide Nanoparticles Used as a Fluorescent Label in an Immunoassay for Atrazine. *Anal. Chem.* **2003**, *75*, 5282-5286.
118. Luo, S.; Zhang, E.; Su, Y.; Cheng, T.; Shi, C., A Review of NIR Dyes in Cancer Targeting and Imaging. *Biomaterials* **2011**, *32*, 7127-7138.
119. Genger, U. R.; Markus, G.; S. Jaricot, S.C.; Nitschke, R.; Nann, T., Quantum Dots Versus Organic Dyes as Fluorescent Labels. *Nat. Methods* **2008**, *5*, 763.

120. Kim, S.; Fisher, B.; Eisler, H.-J.; Bawendi, M., Type-II Quantum Dots: CdTe/CdSe(Core/Shell) and CdSe/ZnTe(Core/Shell) Heterostructures. *J. Am. Chem. Soc.* **2003**, *125*, 11466-11467.
121. Fortin, G. R. A.; Winnik, F. M.; Maysinger, D., Differences in Subcellular Distribution and Toxicity of Green and Red Emitting CdTe Quantum Dots. *J. Mol. Med.* **2005**, *83*, 377-385.
122. Wuister, S. F.; Swart, I.; van Driel, F.; Hickey, S. G.; de Mello Donegá, C., Highly Luminescent Water-Soluble CdTe Quantum Dots. *Nano Lett.* **2003**, *3*, 503-507.
123. Michalet, X.; Pinaud, F. F.; Bentolila, L. A.; Tsay, J. M.; Doose, S.; Li, J. J.; Sundaresan, G.; Wu, A. M.; Gambhir, S. S.; Weiss, S., Quantum Dots for Live Cells, *in vivo* Imaging, and Diagnostics. *Science* **2005**, *307*, 538-544.
124. Derfus, A. M.; Chan, W. C. W.; Bhatia, S. N., Probing the Cytotoxicity of Semiconductor Quantum Dots. *Nano Lett.* **2004**, *4*, 11-18.
125. Liang, J. G.; He, Z. K.; Zhang, S. S.; Huang, S.; Ai, X. P.; Yang, H. X.; Han, H. Y., Study on DNA Damage Induced by CdSe Quantum Dots Using Nucleic Acid Molecular “light Switches” as probe. *Talanta* **2007**, *71*, 1675-1678.
126. Liu, W.; Howarth, M.; Greytak, A. B.; Zheng, Y.; Nocera, D. G.; Ting, A. Y.; Bawendi, M. G., Compact Biocompatible Quantum Dots Functionalized for Cellular Imaging. *J. Am. Chem. Soc.* **2008**, *130* (4), 1274-1284.
127. Yao, J.; Larson, D. R.; Vishwasrao, H. D.; Zipfel, W. R.; Webb, W. W., Blinking and Nonradiant Dark Fraction of Water-Soluble Quantum Dots in Aqueous Solution. *Proc. Natl. Acad. Sci. U.S.A.* **2005**, *102*, 14284-14289.
128. Li, L.; Wu, G.; Yang, G.; Peng, J.; Zhao, J.; Zhu, J.-J., Focusing on Luminescent Graphene Quantum Dots: Current Status and Future Perspectives. *Nanoscale* **2013**, *5*, 4015-4039.
129. Zheng, X. T.; Ananthanarayanan, A.; Luo, K. Q.; Chen, P., Glowing Graphene Quantum Dots and Carbon Dots: Properties, Syntheses, and Biological Applications. *Small* **2015**, *11*, 1620-1636.
130. Tian, P.; Tang, L.; Teng, K. S.; Lau, S. P., Graphene Quantum Dots from Chemistry to Applications. *Mater. Today Chem.* **2018**, *10*, 221-258.
131. Bacon, M.; Bradley, S. J.; Nann, T., Graphene Quantum Dots. *Part. Part. Syst. Charact.* **2014**, *31*, 415-428.

132. Kalluri, A.; Debnath, D.; Dharmadhikari, B.; Patra, P., Chapter Twelve - Graphene Quantum Dots: Synthesis and Applications. In *Methods in Enzymology*, Kumar, C. V., Ed. Academic Press: 2018; Vol. 609, pp 335-354.
133. Ozhukil Valappil, M.; K. Pillai, V.; Alwarappan, S., Spotlighting Graphene Quantum Dots and Beyond: Synthesis, Properties and Sensing Applications. *Appl. Mater. Today* **2017**, *9*, 350-371.
134. Novák, J. r.; Kozler, J.; Janoš, P.; Čežíková, J.; Tokarová, V.; Madronová, L., Humic acids from coals of the North-Bohemian coal field: I. Preparation and characterisation Reactive and Functional Polymers. **2001**, *47*, 101-109.
135. Reddy, C. A.; Saravanan, R. S., Chapter Three - Polymicrobial Multi-functional Approach for Enhancement of Crop Productivity. In *Advances in Applied Microbiology*, Sariaslani, S.; Gadd, G. M., Eds. Academic Press: 2013; Vol. 82, pp 53-113.
136. Piccolo, A.; Spaccini, R.; Drosos, M.; Vinci, G.; Cozzolino, V., Chapter 4 - The Molecular Composition of Humus Carbon: Recalcitrance and Reactivity in Soils. In *The Future of Soil Carbon*, Garcia, C.; Nannipieri, P.; Hernandez, T., Eds. Academic Press: 2018; pp 87-124.
137. Dong, Y.; Chen, C.; Zheng, X.; Gao, L.; Cui, Z.; Yang, H.; Guo, C.; Chi, Y.; Li, C. M., One-step and high yield simultaneous preparation of single- and multi-layer graphene quantum dots from CX-72 carbon black *J. Mater. Chem.* **2012**, *22*, 8764-8766.
138. Li, L.-L.; Ji, J.; Fei, R.; Wang, C.-Z.; Lu, Q.; Zhang, J.-R.; Jiang, L.-P.; Zhu, J.-J., A Facile Microwave Avenue to Electrochemiluminescent Two-Color Graphene Quantum Dots. *Adv. Funct. Mater.* **2012**, *22*, 2971-2979.
139. Pan, D.; Zhang, J.; Li, Z.; Wu, M., Hydrothermal Route for Cutting Graphene Sheets into Blue-Luminescent Graphene Quantum Dots. *Adv. Mater.* **2010**, *22*, 734-738.
140. Lin, L.; Zhang, S., Creating high yield water soluble luminescent graphene quantum dots via exfoliating and disintegrating carbon nanotubes and graphite flakes *Chem. Commun.* **2012**, *48*, 10177-10179.
141. Lu, Y.-C.; Chen, J.; Wang, A.-J.; Bao, N.; Feng, J.-J.; Wang, W.; Shao, L., Facile synthesis of oxygen and sulfur co-doped graphitic carbon nitride fluorescent quantum dots and their application for mercury(ii) detection and bioimaging. *J. Mater. Chem. C* **2015**, *3*, 73-78.

142. Gao, J.; Yin, J.; Tao, Z.; Liu, Y.; Lin, X.; Deng, J.; Wang, S., An Ultrasensitive Fluorescence Sensor with Simple Operation for Cu²⁺ Specific Detection in Drinking Water. *ACS Omega* **2018**, *3*, 3045-3050.
143. Muralikrishna, I. V.; Manickam, V., Chapter One - Introduction. In *Environmental Management*, Muralikrishna, I. V.; Manickam, V., Eds. Butterworth-Heinemann: 2017; pp 1-4.
144. Tchounwou, P. B.; Yedjou, C. G.; Patlolla, A. K.; Sutton, D. J., Heavy Metal Toxicity and the Environment. In *Molecular, Clinical and Environmental Toxicology: Volume 3: Environmental Toxicology*, Luch, A., Ed. Springer Basel: Basel, 2012; pp 133-164.
145. Fernández, B.; Lobo, L.; Pereiro, R., Atomic Absorption Spectrometry | Fundamentals, Instrumentation and Capabilities. In *Encyclopedia of Analytical Science (Third Edition)*, Worsfold, P.; Poole, C.; Townshend, A.; Miró, M., Eds. Academic Press: Oxford, 2019; pp 137-143.
146. Lin, T.-W.; Huang, S.-D., Direct and Simultaneous Determination of Copper, Chromium, Aluminum, and Manganese in Urine with a Multielement Graphite Furnace Atomic Absorption Spectrometer. *Anal. Chem.* **2001**, *73*, 4319-4325.
147. Bonchin, S. L.; Zoorob, G. K.; Caruso, J. A., Atomic Emission, Methods and Instrumentation. In *Encyclopedia of Spectroscopy and Spectrometry*, Lindon, J. C., Ed. Elsevier: Oxford, 1999; pp 42-50.
148. Abou-Shakra, F. R., Chapter 12 - Biomedical applications of inductively coupled plasma mass spectrometry (ICP-MS) as an element specific detector for chromatographic separations. In *Handbook of Analytical Separations*, Wilson, I. D., Ed. Elsevier Science B.V.: 2003; Vol. 4, pp 351-371.
149. Mahapatra, A. K.; Hazra, G.; Das, N. K.; Goswami, S., A Highly Selective Triphenylamine-based Indolylmethane Derivatives as Colorimetric and Turn-off Fluorimetric Sensor toward Cu²⁺ Detection by Deprotonation of Secondary Amines would Copper Transport and its Alterations in Menkes and Wilson Diseases. *Sens. Actuators B Chem.* **2011**, *156*, 456-462.
150. Newgard, C. B.; Stevens, R. D.; Wenner, B. R.; Burgess, S. C.; Ilkayeva, O.; Muehlbauer, M. J.; Dean Sherry, A.; Bain, J. R., Chapter 9 - Comprehensive Metabolic Analysis for Understanding of Disease. In *Essentials of Genomic and Personalized*

Medicine, Ginsburg, G. S.; Willard, H. F., Eds. Academic Press: San Diego, 2010; pp 97-107.

151. Luo, S.; Zhang, E.; Su, Y.; Cheng, T.; Shi, C., A review of NIR dyes in cancer targeting and imaging. *Biomaterials* **2011**, *32*, 7127-7138.

152. Genger, U. R.; Markus, G.; S. Jaricot, S.C.; Nitschke, R.; Nann, T., Quantum dots versus organic dyes as fluorescent labels. *Nat. Methods* **2008**, *5*, 763.

153. Wu, C.; Chiu, D. T., Highly fluorescent semiconducting polymer dots for biology and medicine. *Angew. Chem. Int. Ed. Engl.* **2013**, *52*, 3086-3109.

154. Espósito, B. P.; Epsztejn, S.; Breuer, W.; Cabantchik, Z. I., A Review of Fluorescence Methods for Assessing Labile Iron in Cells and Biological Fluids. *Anal. Biochem.* **2002**, *304*, 1-18.

155. Bustos, A. R. M.; Winchester, M. R., Single-Particle-ICP-MS Advances. *Anal. Bioanal. Chem.* 2016, *408*, 5051-5052.

156. Wu, X.; DeGottardi, Q.; Wu, I. C.; Yu, J.; Wu, L.; Ye, F.; Kuo, C.-T.; Kwok, W. W.; Chiu, D. T., Lanthanide-Coordinated Semiconducting Polymer Dots Used for Flow Cytometry and Mass Cytometry. *Angew. Chem. Int. Ed.* **2017**, *56*, 14908-14912.

157. Tapiero, H.; Townsend, D. M.; Tew, K. D., Trace Elements in Human Physiology and Pathology. *Biomed. Pharmacother.* **2003**, *57*, 386-398.

158. Liu, J.; Simms, M.; Song, S.; King, R. S.; Cobb, G. P., Physiological Effects of Copper Oxide Nanoparticles and Arsenic on the Growth and Life Cycle of Rice. *Environ. Sci. Technol.* **2018**, *52*, 13728-13737.

159. Hiroko, K.; Chie, F.; Wattanaporn, B., Inherited Copper Transport Disorders: Biochemical Mechanisms, Diagnosis, and Treatment. *Curr. Drug Metab* **2012**, *13*, 237-250.

160. Bandmann, O.; Weiss, K. H.; Kaler, S. G., Wilson's Disease and Other Neurological Copper Disorders. *Lancet Neurol* **2015**, *14*, 103-113.

161. DiDonato, M.; Sarkar, B., Copper Transport and Its Alterations in Menkes and Wilson Diseases. *Biochi. Biophys. Acta (BBA) - Molecular Basis of Disease* **1997**, *1360* (1), 3-16.

162. Ge, C.; Chen, J.; Wu, W.; Fang, Z.; Chen, L.; Liu, Q.; Wang, L.; Xing, X.; Zeng, L., An Enzyme-free and Label-free Assay for Copper(ii) Ion Detection based on Self-assembled DNA Concatamers and Sybr Green I. *Analyst* **2013**, *138*, 4737-4740.
163. Min, M.; Wang, X.; Chen, Y.; Wang, L.; Huang, H.; Shi, J., Highly Sensitive and Selective Cu²⁺ Sensor Based on Electrospun Rhodamine Dye Doped Poly(ether sulfones) Nanofibers. *Sens. Actuators B Chem.* **2013**, *188*, 360-366.
164. Dong, Y.; Wang, R.; Li, G.; Chen, C.; Chi, Y.; Chen, G., Polyamine-Functionalized Carbon Quantum Dots as Fluorescent Probes for Selective and Sensitive Detection of Copper Ions. *Anal. Chem.* **2012**, *84*, 6220-6224.
165. Lan, G.-Y.; Huang, C.-C.; Chang, H.-T., Silver Nanoclusters as Fluorescent Probes for Selective and Sensitive Detection of Copper ions. *Chem. Commun.* **2010**, *46*, 1257-1259.
166. Su, P.-G.; Lin, L.-G.; Lin, P.-H., Detection of Cu(II) Ion by an Electrochemical Sensor Made of 5,17-bis(4'-nitrophenylazo)-25,26,27,28-tetrahydroxycalix[4]arene-Electromodified Electrode. *Sens. Actuators B Chem.* **2014**, *191*, 364-370.
167. Prado, C.; Wilkins, S. J.; Marken, F.; Compton, R. G., Simultaneous Electrochemical Detection and Determination of Lead and Copper at Boron-Doped Diamond Film Electrodes. *Electroanal.* **2002**, *14*, 262-272.